Digital Twin-Based Scour Monitoring of Masonry Bridges

Case Study of the Regent Bridge

Luyuan Long

Delft University of Technology

TU Delft

Digital Twin-Based Scour Monitoring of Masonry Bridges

Case Study of the Regent Bridge

by

Luyuan Long

to obtain the degree of Master of Science
at the Delft University of Technology,
to be defended publicly on July 21, 2025.

Student number:	5917026
Supervisor:	Maria Pregnolato
Supervisor:	Eliz-Mari Lourens
Committee member:	Kenneth Gavin

Cover: Mehmed Paša Sokolović Bridge; Image from Holamon.cat.

TU Delft

Preface

As I reach this final stroke of writing, it marks the closing chapter of my master's journey in Delft. As the saying goes, all banquets must come to an end, and every film has its curtain call. Whether in joy or sorrow, it is time to bid farewell to the past self. I feel deeply honored to conclude this chapter with a thesis on the structural health monitoring of masonry bridges. Applying a cutting-edge monitoring technique to one of the oldest architectural forms has been an endlessly fascinating endeavor.

Along this journey, my foremost gratitude goes to my daily supervisor, Maria Pregnolato. You were the one who helped me find and coordinate an array of resources to launch this compelling topic, and throughout, your unwavering support has been invaluable. I am equally grateful to my supervisory team, Eliz-Mari Lourens and Kenneth Gavin, for the professional and insightful guidance you offered in your respective areas of expertise. Each of our discussions has opened new perspectives and pushed my thinking further.

I would also like to express my appreciation to Kristopher Campbell, Myra Lydon, and their team, who provided the original monitoring data used in this thesis. My thanks also go to Xuehui Zhang for sharing thoughtful insights and valuable suggestions on the monitoring framework that underpins this work.

Last but not least, I am deeply thankful to my friends and family. It is your companionship that has made this journey so joyful, fulfilling, and full of light.

Luyuan Long
Delft, July 2025

Abstract

Scour has become one of the most significant hazards affecting masonry bridges. Existing scour monitoring techniques often fail to meet the requirements for continuous and time-domain tracking of scour evolution. Moreover, existing scour early-warning systems predominantly rely on threshold-based risk assessment and management frameworks. A critical limitation of these systems is the difficulty in accurately defining threshold values, which are often derived from historical monitoring experiences. Given the variability in foundation conditions and river scour characteristics across different bridges, standardized threshold setting is highly challenging. Furthermore, threshold determination often lacks correlation with the health condition of the superstructure, which is an aspect engineers care most about. These deficiencies highlight the urgent need for a more intelligent monitoring framework that can integrate multiple monitoring techniques and facilitate interactive associations between monitoring data and the health condition of the superstructure.

This study explores the use of digital twin (DT) technology to overcome the shortcomings of current monitoring and maintenance strategies. By integrating real-world monitoring measurements with finite element modeling, the DT framework provides the opportunity to simulate ”what-if” scenarios under high-fidelity conditions. Such advancements offer novel prospects for detecting scour-induced damage and intervening for the maintenance. This study utilizes DT technology within the context of a scour monitoring project for a masonry bridge in Northern Ireland, United Kingdom. A digital twin-based SHM and maintenance framework is developed to achieve seamless communication between the virtual model and the physical structure using sensor data. The developed model addresses limitations associated with traditional monitoring and maintenance approaches and demonstrates the potential of digital twins in forward model calibration and backward decision-making.

Digital Twin-Based Scour Monitoring of Masonry Bridges

Case Study of the Regent Bridge

by

Luyuan Long

to obtain the degree of Master of Science
at the Delft University of Technology,
to be defended publicly on July 21, 2025.

Student number:	5917026
Supervisor:	Maria Pregnolato
Supervisor:	Eliz-Mari Lourens
Committee member:	Kenneth Gavin

Cover: Mehmed Paša Sokolović Bridge; Image from Holamon.cat.

TU Delft

Contents

Nomenclature

Abbreviations

Abbreviation	Definition
DT	Digital Twin
SHM	Structural Health Monitoring
FEM	Finite Element Method
FBG	Fiber Bragg Grating
TLS	Terrestrial Laser Scanning
UAV	Unmanned Aerial Vehicle
GPR	Ground Penetrating Radar
BIM	Building Information Modeling
OMA	Operational Modal Analysis
EMA	Experimental Modal Analysis
VIV	Vortex-Induced Vibration
NDT	Non-Destructive Testing
MAC	Modal Assurance Criterion

Symbols

Symbol	Definition	Unit
ρ	Density	[kg/m^3]
ν	Kinematic viscosity	[m^2/s]
ν	Poisson's ratio	[-]
E	Elastic modulus	[GPa]
f_{num}, f_{exp}	Numerical / Experimental natural frequency	[Hz]
f_c, f_t	Uniaxial compressive / tensile strength	[MPa]
ϕ_{num}, ϕ_{exp}	Numerical / Experimental mode shape	[-]
ϕ_i	Inclination angle (in scour pit)	[°]
Re	Reynolds number	[-]
u, v, w	Velocity components in x, y, z directions	[m/s]
w_i, λ_i	Weights in optimization function	[-]
V/H	Shear-to-normal force ratio	[-]
ΔT	Temperature difference	[°C]

1 Introduction

1.1. Background

Bridges near waterways or oceans are susceptible to the impact of scour, which is defined as the erosion of bed material caused by flowing water due to local acceleration, turbulence, and sediment transport imbalances [1, 2, 3]. Scour is a leading cause of bridge failure worldwide, especially during extreme hydraulic events such as flooding. With global climate change, flood risks are expected to increase significantly in the future [4], which will accelerate the scour processes of bridges.

Masonry bridges serve as transportation mediums and are part of the cultural heritage. Some representative masonry bridges are shown in Figure 1.1. In regions such as Northern Ireland, masonry bridges still account for 53% of the total bridge stock [5]. Those masonry bridges are typically constructed from brick and stone units bonded by mortar and generally have lower resistance to scour compared to reinforced concrete bridges. Moreover, masonry bridges are often supported by shallow foundations, which are particularly vulnerable to scour during flood events [6, 7].

Figure 1.1: Representative masonry bridges. (a) Servatius bridge in the Netherlands [8]; (b) Ponte Vecchio bridge in Italy [9]; (c) Charles bridge in Czech [10]; (d) Old Bridge of Gien in France [11]

Masonry bridges are threatened by scour. This concern is proved by global evidence indicating that scour is a primary cause of bridge failure [12], with studies showing that approximately 50% to 60% of bridge failures in the United States are associated with scour [13, 14]. In China, approximately 45% of bridge failures are due to scour [15].In regions like Europe, particular attention

should be paid to the risks of masonry bridge failure, as these areas often have a high stock of historic masonry bridges while facing increasing flood risks. Besides, to better characterize the impact of scour on masonry bridges, it is important to clarify the concept of structural failure. In this study, structural failure is defined not as complete collapse but as the loss of serviceability, that is, the bridge's inability to fulfill its intended structural and functional roles. As shown in Figure 1.2, many reported scour failures do not involve full structural collapse; rather, they reflect localized damage, such as cracking or sliding, that compromises safety and function.

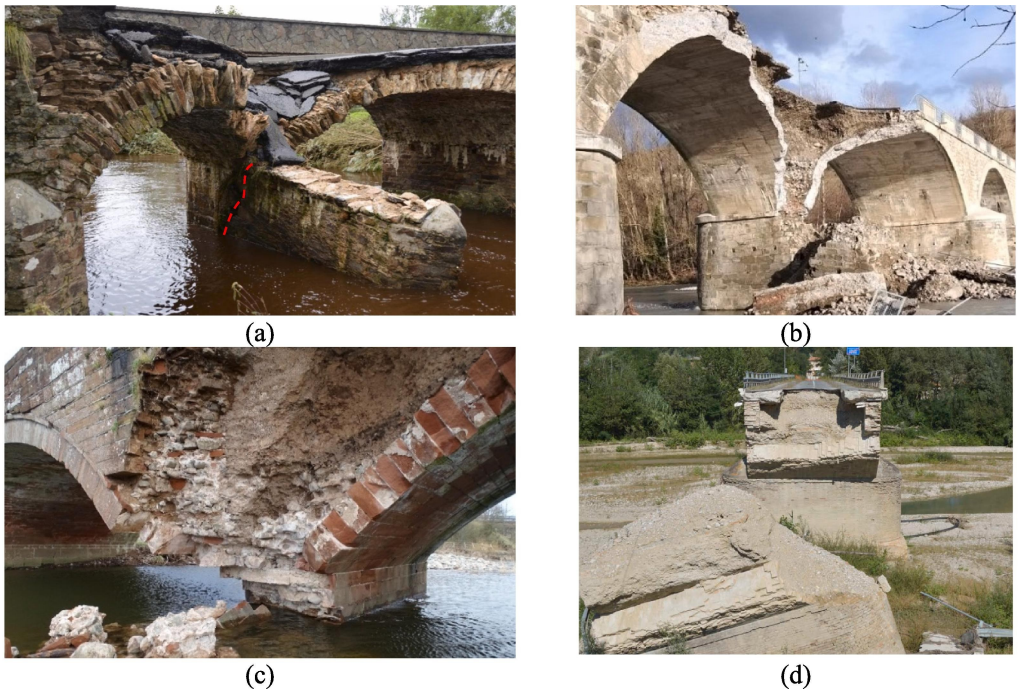

Figure 1.2: Some failure cases of masonry bridges due to scouring: (a) Ballynameen bridge; (b) Samonee bridge; (c) Brougham Old bridge; (d) Rubbianello bridge [16]

To assess how different scour mechanisms may trigger structural failure, it is necessary to first classify and understand the dominant types of scour. Scour is typically classified into three types: general scour, contraction scour, and local scour [1, 17]. General scour refers to the uniform lowering of the riverbed caused by natural hydrological and geological processes. Contraction scour occurs when the flow area is constricted due to the presence of bridge piers, leading to increased flow velocity and erosion. Local scour develops near bridge piers or abutments, driven by flow impact and vortex formation. Local scour often causes localized deformation of the riverbed. Notably, because local scour acts directly on piers or abutments and poses an immediate threat to bridge safety, it has been the most extensively studied and closely monitored scour mechanism.

The mechanism of bridge scour is highly complex, involving interactions among soil, structure, and fluid. At present, for a given flood event, it remains difficult to accurately predict changes in river boundaries. This challenge is not only due to the complexity of this interaction problem but also to the fact that different bridges have entirely distinct geometry and material properties [18]. In addition, the failure mechanisms of masonry bridges under scour conditions differ from those

of modern bridges primarily constructed with reinforced concrete. In modern bridges, failure typically behaves as a loss of bearing capacity in the vertical direction, bending or sliding of pile foundations in the horizontal direction, and in some cases, tilting or overturning of the foundation caused by asymmetric lateral scour [15]. For masonry bridges, although the triggering factor is also the reduction in soil stiffness around the pier or abutment foundation, the process is more characterized by stress redistribution within the masonry arch ring. The final failure mode often presents as local failure between the arch and the spandrel wall [6].

Regarding the scour patterns, as shown in Figure 1.3, both symmetric and asymmetric scour can occur laterally (x-x direction). In symmetric scour (Case 1), the development of scour holes on both sides is similar, and the scour primarily results in vertical foundation settlement. In contrast, in asymmetric lateral scour (Case 2), one side scours significantly slower than the other, such as the right side in the figure, which leads to a gentler scour pit on that side (reflected by $\varphi_4 < \varphi_3$), potentially causing tilting of the pier foundation toward the right. Another scour pattern is longitudinally asymmetric scour along the river flow direction (z-z direction), as illustrated in Case 3 of the figure. In this case, the upstream face is exposed to stronger hydrodynamic forces compared to the downstream side, resulting in an asymmetric scour pit (reflected by $\varphi_6 < \varphi_5$) that may cause tilting and rotation of the pier. It should be noted that actual scour scenarios are often a combination of one or more of these three cases.

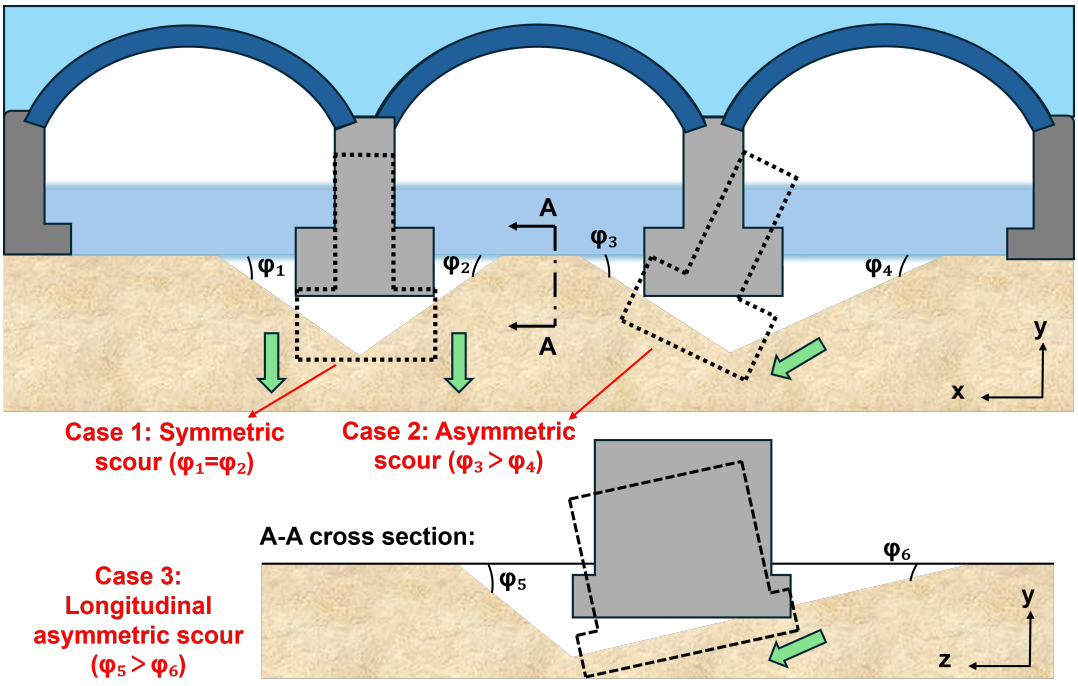

Figure 1.3: Scour pattern

Due to the aforementioned issues related to bridge scour, the monitoring of scour has long attracted significant attention from both industry and academia. The most traditional method is manual visual inspection, where trained divers perform underwater surveys to observe and measure the morphology and depth of scour holes. However, this method has several evident drawbacks.

First, it is labor-intensive and costly; in countries with a large number of bridges, conducting regular diving inspections for each bridge needs large expenditures. Second, diving is not possible during flood events, which are unfortunately the periods when the risk of scour-induced failure is highest. Third, the inspection process itself involves safety risks. And lastly, manual visual inspections are discrete, which means they cannot provide continuous time-domain measurement about the scour depth. As an alternative to underwater inspection, nondestructive testing (NDT) methods, such as radar and sonar [19, 20], have been applied to scour monitoring. While these techniques reduce the need for direct human involvement in underwater inspections, they remain expensive and provide only discrete data. Since local scour is a time-dependent process [18], such methods are insufficient for capturing the continuous evolution of scour over time.

Recent advances in sensing technologies, including fiber Bragg grating (FBG) sensors and piezoelectric sensors, have been increasingly adopted for monitoring scour [21, 22]. Additionally, accelerometers have been used to detect scour development through changes in structural modal properties [23, 24]. Compared to traditional methods, these techniques enable low-cost, low-maintenance, and continuous monitoring of bridge scour. However, a remaining issue in nearly all structural health monitoring (SHM) systems (including scour monitoring) is the disconnection between the monitoring data and the actual structural mechanical response. For instance, while commonly used sensors can detect strain or vibration at localized points, they do not directly reveal whether the global stress state of the structure remains within safe limits. Engineers need to assess the health state of the structures to support the decision-making process, where actions such as maintenance are involved. These questions are difficult to answer from the traditional SHM perspective.

Finite element (FE) models offer a means to simulate internal stress states and evaluate "what-if" scenarios. However, these models are typically static and rely on manually defined parameters, making them insensitive to time-dependent changes of geometry, boundary condition, and material. This limitation is especially critical for historic masonry bridges, where design documentation is often unavailable and both geometric and material properties are highly uncertain [25]. In particular, the geometric uncertainty of such structures manifests in various forms, including severe shape distortion, cracking or spalling of masonry units, separation between the arch and spandrel walls, and displacement or rotation of piers [26, 27, 28, 16]. In terms of material uncertainty, the sources of the uncertainty could be the inevitable aging of materials over time [29], as well as the spatial heterogeneity of masonry components [30, 31].

Due to the aforementioned limitations of SHM and FEM, bridge maintenance strategies remain largely reliant on preventive maintenance. This approach involves scheduled inspections and interventions at fixed time intervals or cycles. Although widely adopted, it is empirical in nature and often results in two unfavorable outcomes: excessive maintenance, which leads to unnecessary costs, or insufficient maintenance, which increases the risk of structural degradation or even failure.

Recent advances in SHM have led to a gradual transition toward condition-based maintenance (CBM) strategies [32]. CBM is a maintenance strategy that triggers interventions based on the

health condition of the structure rather than at fixed time intervals. The difference between preventive and condition-based maintenance is illustrated in Figure 1.4. The figure demonstrates that the overall structural performance, represented by the global performance envelope, is partially restored after each maintenance intervention.

In preventive maintenance, interventions are triggered by predefined time intervals (e.g., ΔT), regardless of actual structural condition. As shown in Case 1, this may lead to premature maintenance during early stages of service life, causing unnecessary expenditure. In contrast, Case 2 illustrates delayed intervention at later stages, which can bring the structure close to its critical failure threshold. Failure may even occur before the end of the intended design life.

Condition-based maintenance addresses this issue by detecting anomalies using sensor data and determining intervention timing based on mechanical response quantities. The intervention is initiated once the measured variables (such as strain, stress, and rotation angle) exceed a predefined threshold, such as the intervention level in Figure 1.4. This strategy aims to optimize maintenance by avoiding both premature interventions and failure risks, thereby achieving a more efficient and reliable maintenance regime. Nevertheless, a fundamental limitation of current CBM practices is how the intervention level is determined. In most cases, the intervention strain is determined empirically or based on design codes, introducing considerable subjectivity in practical engineering applications.

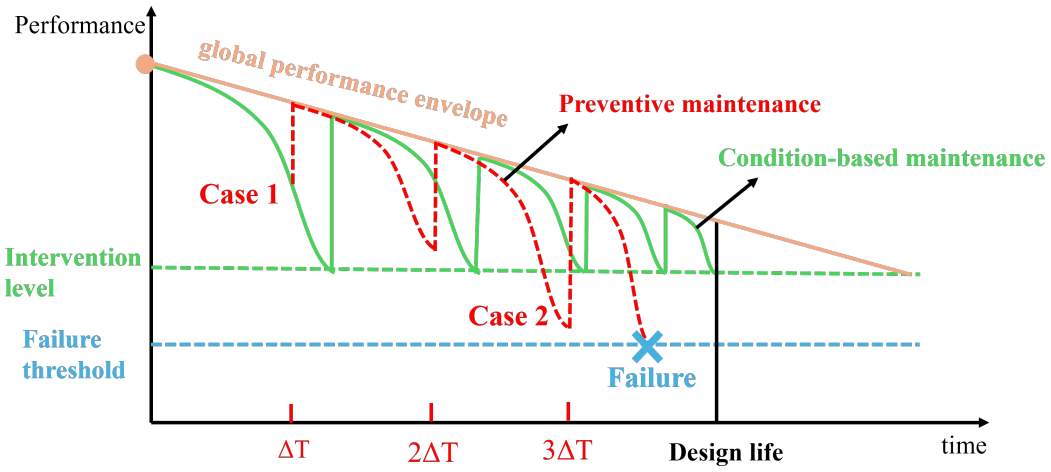

Figure 1.4: The comparison between preventive maintenance and condition-based maintenance in SHM

It is worth investigating how to propose a framework that can address the limitations of monitoring and FE analysis when applied separately to masonry bridges. This framework is proposed to reduce the subjectivity of traditional preventive and condition-based maintenance. Specifically, within this framework, the monitoring system provides accurate time-dependent information about the scour depth evolution in the field. Meanwhile, the FE module is capable of simulating "what-if" scenarios for scour progression and identifying the critical state at which structural failure is imminent. This failure condition corresponds to a so-called *maximum allowable scour depth*, which represents the critical scour depth under near-failure conditions. By comparing the monitored

scour depth with the critical depth predicted from simulations, and incorporating an appropriate safety margin, a more advanced predictive maintenance framework can be developed. Although previous guidelines and case studies have proposed determining the maximum allowable scour depth via structural back-analysis [33], these methods have rarely been implemented in practice. Moreover, the failure criteria adopted in such methods are primarily based on the lateral stability and vertical bearing capacity of the foundation, however, those principles are not fully applicable to masonry bridges. In the case of masonry bridges, failure is more often governed by the degradation of foundation stiffness due to scour, which then causes stress redistribution in the superstructure and triggers equilibrium instability of the arch mechanism [34, 6]. Most importantly, the maximum allowable scour depth is not a fixed value. It evolves dynamically with the structural condition of the bridge and varies with changes in geometry, material aging, and boundary conditions. These influencing factors are highly uncertain and time-dependent, especially in historical masonry bridges [25, 29]. As a result, a static FEM cannot reliably predict the true structural limit state. Therefore, defining predictive maintenance strategies for masonry bridges under scour scenarios remains a crucial topic.

In recent years, the emergence of the digital twin (DT) concept has provided a viable solution to the aforementioned challenges. The term ”digital twin” was introduced in 2005 by Grieves [35]. While definitions of digital twins vary depending on the application fields, in general, a digital twin is considered a virtual representation of a real physical system, including the physical object itself, its surrounding environment, and the physical processes it undergoes. The virtual representation should be dynamically updated using data from the physical system [36]. Although the concept of digital twins has existed for decades, its application in the field of SHM has only gained significant attention in recent years. Digital twins have changed the operation and maintenance of structures to a more intelligent and data-driven level. An ideal digital twin is capable of continuously updating the virtual model based on monitoring data from the field, such as geometric information and stress-strain responses. Within the digital environment, simulations of the actual structure can be performed, enabling feedback on the structural health condition to be transmitted to the physical asset. At a more advanced level, a digital twin also supports remaining useful life prediction and predictive maintenance of the structure [37, 38].

1.2. Problem statement

Digital twins can integrate scour monitoring data with numerical models to support predictive maintenance strategies [38]. However, existing digital twin applications still largely remain at the conceptual level. In the limited case studies, digital twins often encounter several challenges. One of the most commonly reported issues is their high computational cost, especially when applied to large-scale engineering systems that require real-time updates and the assimilation of massive data streams [39, 40]. Another limitation is that most existing digital twin applications are still confined to the visualization stage [41], whereas the true value of digital twins lies in establishing a closed-loop interaction between the physical structure and its virtual model. This interaction involves updating the virtual model with sensor data and using simulation results to guide real-world

maintenance decisions. Research addressing this bidirectional feedback loop remains rare.

Another critical challenge is the fusion of heterogeneous monitoring data, with only a few relevant case studies reported [42, 43]. Furthermore, to the best of the authors' knowledge, existing digital twin frameworks rarely focus explicitly on scour maintenance for masonry bridges. Definitions of what constitutes a functional DT in this context are vague. Thus, a significant research gap remains in this area.

The core problem to be addressed in this study is how to transition from traditional monitoring and preventive maintenance towards a predictive, state-informed approach enabled by a digital twin framework. This framework integrates sensing data, numerical modeling, and structural assessment to timely evaluate the health condition of bridges and support maintenance decisions. Specifically, the study investigates the implementation of this framework in the context of masonry bridges affected by scour.

1.3. Research objective

The objective of this thesis is to propose a digital twin framework for scour monitoring and maintenance in masonry bridges. Building upon existing research, a case study is conducted to demonstrate the feasibility of the framework. The proposed framework is designed to support a bidirectional physical-virtual loop. In the forward direction, geometric information, structural monitoring data, and other heterogeneous inputs (e.g., river flow measurements) from the physical entity can update and synchronize the virtual model, enabling a high-fidelity digital representation of the real-world system. In the backward direction, the virtual entity, through its simulation and predictive capabilities, can provide decision support for scour-related maintenance scenarios in the physical domain, such as structural condition assessment [44], risk evaluation and early warning [45], and sensor placement optimization [46, 47].

Current monitoring and maintenance systems for masonry bridges often suffer from limited accuracy, delayed decision-making, and insufficient utilization of available data, leading to unnecessary maintenance expenditures or elevated structural risks. This thesis aims to harness the capabilities of digital twin ideas to address and mitigate these limitations. This aim is achieved through the following objectives:

1. Review the state-of-the-art in scour monitoring techniques and the maintenance strategies of bridge, the uncertainties in masonry bridges and model calibrations, and the potential scour failure mechanisms.
2. Perform FE analysis on the calibrated FE model to investigate potential scour failure mechanisms and the indicators of a failure. Then simulate the maximum allowable scour depth which represents the corresponding scour depth when the bridge structure is in its critical state of failure.
3. Evaluate the performance of a vortex flow-based FBG sensor system by analyzing the simulation signals and validating its ability to track scour depth evolution.

4. Propose an improved monitoring and early warning maintenance strategy by integrating results from calibrated FE models and scour sensing data to achieve quantitative analysis of the current health state and detection of potential failure signals.

The remainder of this thesis is as follows: Chapter 2 provides a comprehensive literature review on scour monitoring and maintenance techniques, model uncertainties in masonry bridges, and the failure mechanisms of bridges under scouring. Chapter 3 introduces the methodology of the digital twin framework and the background of case study. Chapter 4 presents the FE analysis of the Regent bridge. Chapter 5 is the structural health monitoring of the Regent bridge. Chapter 6 elucidates the connection layer of the digital twin framework. Chapter 7 starts with a discussion, followed by a summary of study limitations and future recommendations. Finally, Chapter 8 concludes the thesis by summarizing the key findings and contributions.

2 Literature review

This chapter will focus on reviewing the existing literature in four key areas: (1) monitoring techniques of bridge scour; (2) uncertainties in masonry bridge and model calibrations; (3) failure mechanisms of bridges under scour; and (4) digital twin applications in bridge management.

2.1. Monitoring and maintenance strategies for bridges

2.1.1. Traditional monitoring techniques of bridge scour

Traditional methods for scour assessment rely heavily on visual inspections, which typically require inspectors to dive beneath the riverbed to observe and measure the degree of foundation exposure caused by scour. These inspections are conducted on a fixed periodic basis. For example, in the United Kingdom, general inspections occur every two years, while principal inspections are carried out every six years [48].

However, this approach presents several limitations:

1. It provides only discrete snapshots, offering no insight into the temporal evolution of scour.
2. It is unable to capture the scour depth during flooding, since the sediment refilling after flooding can obscure the scour hole [1].
3. It lacks the capability for early warning and cannot provide real-time data during flood events, which are precisely along with the highest risk of bridge failure.
4. The inspection outcome is highly dependent on the experience of the inspector, introducing subjectivity and lacking quantitative support.
5. Manual inspections of large bridge inventories are extremely labor-intensive and costly.
6. Diving operations themselves pose significant safety risks to inspection personnel.

To address the limitations of manual inspections, NDT techniques have been developed. Representative methods include sonar [20, 49], radar [50, 51, 19], interferometric synthetic aperture radar (InSAR) [52], and time domain reflectometry (TDR) [53, 54]. Those NDT techniques have, to some extent, overcome the limitations of traditional visual inspections, particularly in terms of safety and accessibility. They offer good performances in detecting scour conditions before and after flooding. However, they still largely belong to discrete monitoring, which means measurements can only be acquired intermittently, and continuous monitoring is not possible. Futhermore, since most NDT devices cannot be conducted during flooding, they are unable to capture the maximum scour depth that may occur under such critical conditions.

2.1.2. Fiber Bragg grating sensor for scour monitoring

To mitigate the issues of traditional monitoring techniques, FBG-based scour monitoring has emerged as a promising solution that could overcome the temporal and spatial limitations. Since

unlike sonar or radar-based systems that provide discrete measurements, FBG sensors are able to deploy continuous, time-domain monitoring. In addition, while many other existing monitoring devices are effective in detecting the extent of scour, few are capable of capturing the onset of scour development, thereby limiting their ability to provide early warning of scouring [55]. In contrast, FBG sensors have demonstrated great potential for tracking both the onset and the progression of scour.

FBG sensors monitor scour based on the principle of wavelength shift in reflected light, which occurs due to strain induced by hydrodynamic pressure or flow impact [21, 56, 57]. As FBG sensors become exposed to water flow due to rising water levels and scour-induced sediment removal, the resulting strain alters the reflected wavelength. Owing to this sensing mechanism, FBG has emerged as one of the most promising scour monitoring technologies in recent years.

Lin et al. [56] were among the first to explore the potential of FBG for tracking scour hole development. In their experiment, FBG sensors were installed on a cantilever beam and embedded in a sand layer. When the beam experienced deformation due to water flow impact or sediment displacement, such as exposure above the riverbed or burial within the sand, the induced strain was detected in real time via the FBG sensor. This mechanism makes it feasible to monitor the progression of scour depth. In a later field study, Lin et al. [58] encapsulated FBG sensors in rubber protective shells and deployed them on an actual bridge. During the monitoring period under flood conditions, several FBG sensors were gradually exposed due to scour and recorded flow impact signals. After the flood event, as sediment refilled the scoured area, the FBG signals returned to a stable state, demonstrating successful monitoring of the full ”scour–refill–re-scour” cycle.

Xiong et al. [21] proposed three FBG-based scour monitoring device designs and ultimately recommended an open-structure sensor protected with epoxy resin. Laboratory experiments confirmed that this configuration offered high durability, immunity to electromagnetic interference, and real-time monitoring capabilities for the entire scour process.

Zhou et al. [57] mounted two FBG sensors on opposite sides of a fiber-reinforced polymer (FRP) beam, which was secured to bridge piers or riverbeds using steel protective covers or anchoring devices. Laboratory results demonstrated the device’s capability to track water flow velocities. Moreover, signal changes under typical scour flow conditions were significantly larger than background noise, indicating strong anti-interference performance.

To enhance FBG sensitivity to the water–sediment interface, Kong et al. [59] integrated a water-swellable polymer (WSP) around the FBG. Flume tests revealed that the axial strain induced by WSP expansion peaked near 500 με, considerably higher than strain levels caused by water flow impact alone.

Ding et al. [60] developed a distributed FBG-based scour monitoring system that identifies sediment surface position based on the pressure difference between water and soil. The basic principle is that when the sensor is in water, the lateral pressure is approximately equal to hydrostatic pressure (near zero), while in soil, the lateral pressure increases with depth. By identifying the

location where lateral pressure equals zero, the system can infer the sediment surface depth and thus enable real-time monitoring of scour and refilling. The feasibility of this approach was validated through laboratory testing.

Crotti et al. [61] developed a field FBG system called BLESS (bed level seeking system) for bridge scour monitoring. The system employs an FBG-based sedimentation probe that exploits the difference in thermal diffusivity between water and saturated soil. By analyzing the FBG's thermal response, namely, the temperature rise (ΔT) and time constant (τ), the sensor can determine whether it is located in water or sediment, therefore indicating the location of the riverbed.

Campbell et al. [62] proposed a novel FBG-based vortex flow sensor that leverages vortex-induced vibrations (VIV) to detect scour progression. Compared to directly measuring strain with conventional FBG sensors, this new optical design enhances monitoring sensitivity by utilizing the dynamic response of rubber fins to amplify flow-induced effects. As a result, it enables more accurate detection of scour depth development. The sensor also facilitates time-domain monitoring of both scour and refilling processes. Its simplified mechanical configuration ensures the durability under complex environmental conditions. Additionally, the resolution of this monitoring device can be quantified by considering the number of the fins and the spacing between each fin. The larger number and smaller spacing will bring higher resolution, as illustrated in Figure 2.1(C). The design drawing and on-site installation sketch are shown in Figure 2.1(A) and (B) respectively.

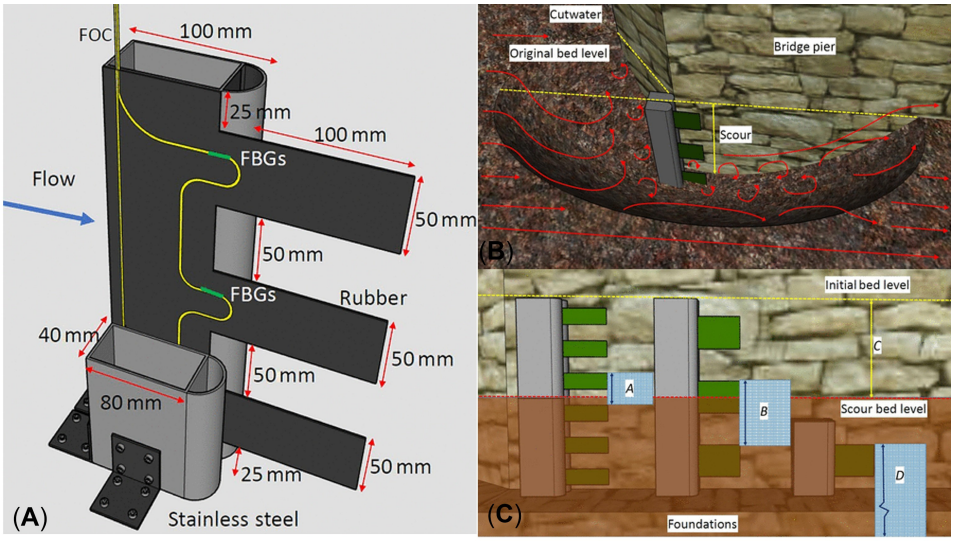

Figure 2.1: The FBG-based VIV sensor monitoring: (A) The design of VIV sensor; (B) The field installation; (C) The resolution of VIV sensor (edited from [62])

2.1.3. Traditional maintenance strategies in bridges

Early maintenance strategies during the operational phase were predominantly based on a "reactive maintenance" approach, also referred to as corrective maintenance [63, 64]. In the context of bridge engineering, this approach involves carrying out repairs only after significant defects have occurred, essentially representing a post-failure maintenance strategy. However, this approach is considerably risky for critical infrastructures like bridges, where structural failures can lead to

severe human and economic consequences [65]. As such, corrective maintenance is inadequate to meet the performance and safety requirements of long-term bridge service.

Later on, in the maintenance practices, management strategies typically relied on the results of regular inspections to guide maintenance decisions, evolving into what is known as preventive maintenance. For example, the U.S. National Bridge Inspection Standards (NBIS) require that most highway bridges in the United States be inspected at least once every 24 months. Additionally, NBIS mandates regular underwater inspections, with intervals not exceeding 60 months, to identify and quantify the extent of scour below the water surface [66]. In another guideline, the U.S. Federal Highway Administration (FHA) specifies that the frequency of scour inspections should be determined based on ratings of underwater inspection results, channel conditions, and scour severity. If these ratings fall below a certain threshold, the scour inspection interval must be reduced to less than 24 months; if the ratings are favorable, the interval may be appropriately extended to 48 months or even up to 60 months depending on the score [67]. The United Kingdom adopts a similar approach, requiring general bridge inspections every two years, with the inspection interval shortened based on scour risk ratings [68].

However, a major limitation of preventive maintenance is that maintenance intervals are typically based on empirical rules and do not reflect the actual health condition of the structure. This approach may result in unnecessary costs during the early stages of the structure's life cycle. In the later stages, when significant damage or material degradation occurs, it often leads to missed opportunities for timely and optimal maintenance interventions.

With the development of structural health monitoring, maintenance strategies have increasingly shifted towards condition-based maintenance (CBM). This approach determines whether maintenance actions are needed based on the actual operational state of the structure. CBM emphasizes proactive maintenance based on the condition of the structure and advocates for performing maintenance only when necessary. Several practical implementations have demonstrated that CBM can effectively avoid the dual problems of ”over-maintenance” and ”under-maintenance” [69]. In terms of implementation, there are two main logical pathways. One is to determine the need for maintenance by comparing current monitoring values against predefined thresholds. The other is to predict the future state of the structure based on trends observed in the monitoring data and to schedule maintenance accordingly [64].

The commonly used maintenance strategies are illustrated in Figure 2.2. It can be observed that bridge maintenance strategies have generally shifted from passive maintenance towards more proactive approaches. With the development and maturation of SHM technologies, the widespread adoption of CBM is foreseeable [70], as this strategy has significant advantages in terms of cost efficiency and maintenance effectiveness compared to other approaches. However, existing CBM strategies still have several notable limitations: (1) Data management is complex. The data formats provided by multiple sensors are often heterogeneous, and there is a lack of unified health assessment indicators among different sensors, resulting in poor data fusion capabilities. (2) Threshold-based CBM approaches often rely on empirical knowledge or expert systems to determine the critical value of the monitoring variables, such as strain, temperature, or

force, which can easily lead to misjudgments. (3) Prediction model-based CBM faces two main challenges. First, there is often a lack of sufficient training data. Second, the predictive models themselves require model updating capabilities, meaning that the models must be continuously retrained with new incoming data. This requirement is difficult to achieve under traditional CBM frameworks.

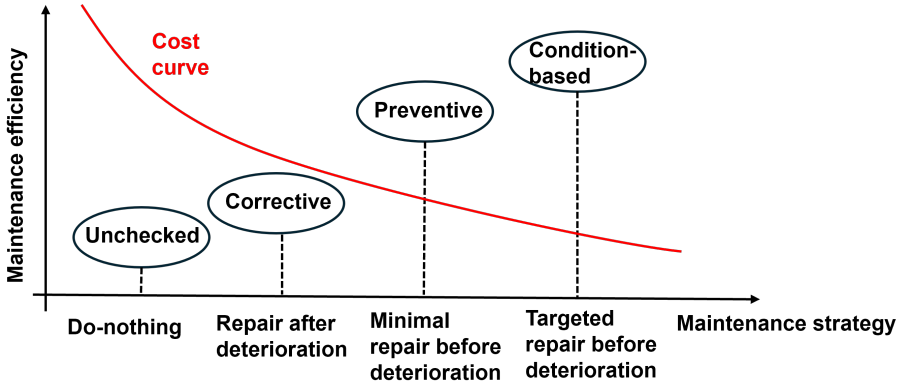

Figure 2.2: The assessment of various maintenance strategies

2.1.4. Digital twin-based predictive maintenance in bridges

Digital twins in bridge engineering typically consist of three layers: the physical layer, the virtual layer, and the connection layer that links them through timely data exchange.

In the physical layer, key aspects include the acquisition, processing, transmission, and storage of monitoring data. Data acquisition involves selecting appropriate sensor types and specifications, determining sensor placement strategies in the field, and defining suitable sampling frequencies [71]. Data processing includes procedures such as smoothing, noise reduction, and filtering [72]. Data are then uploaded and stored via wired (traditional method) or wireless transmission systems [73]. In addition, the physical layer also encompasses the monitored structure and its surrounding environment. This includes the bridge's structural configuration and material composition, as well as external factors such as temperature and humidity, which may contribute to the aging and localized damage of bridges.

In the context of bridge engineering, there are generally two types of virtual models used in digital twin systems. The first is semantic building information model (BIM) [74], which emphasizes visualization and incorporates engineering attributes for virtual inspection. The second type is finite element-based virtual models, which establish input–response relationships. Those two types of virtual twins are shown in Figure 2.3.

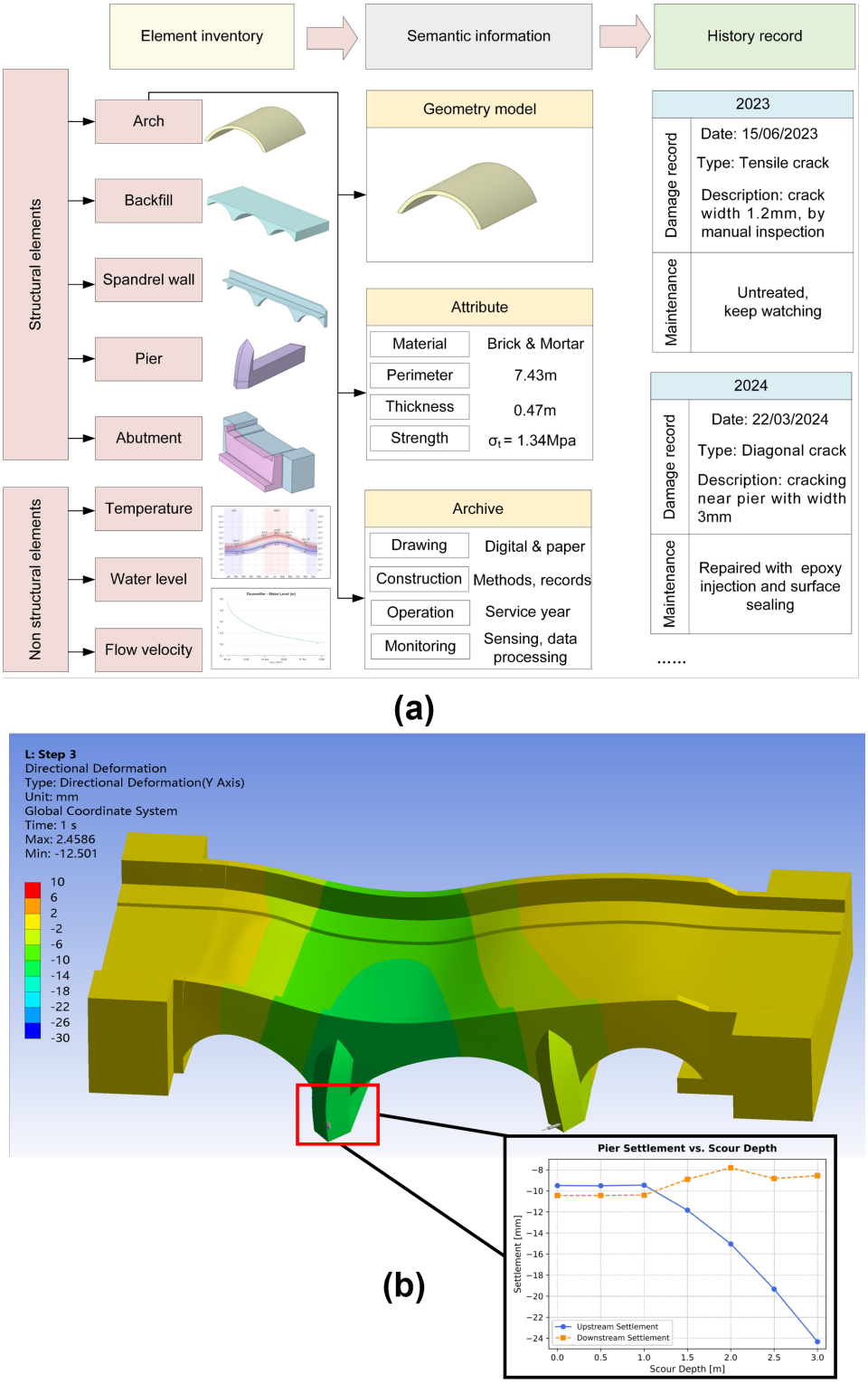

Figure 2.3: Two types of virtual twin model: (a) BIM-based virtual twin for bridge management; (b) FEM-based virtual twin for bridge scour management (case study of this thesis)

The connection layer serves as the critical communication channel between the physical and virtual layers, enabling data transfer and system synchronization. The timely connection between the physical entity and the virtual model distinguishes a digital twin from other digital replicas, such

as three-dimensional models or building information model [43]. Conceptually, this layer facilitates bidirectional information flow: (1) a forward path from the physical entity to the virtual model and (2) a feedback path from the virtual model back to the physical system.

Forward transmission delivers collected physical data into the virtual model and establishes a feature mapping between the two domains. This mapping is typically achieved through model updating techniques [75, 76]. The reverse path, from the virtual model to the physical system, is essential for smart decision-making and active control. This functionality allows the digital twin to issue control instructions or maintenance decisions to the physical entity. Advanced techniques such as intuitive user interfaces, holographic environments, and virtual reality are increasingly adopted to facilitate this process [77, 78, 79]. In addition, this reverse feedback should provide operators and decision-makers with critical structural information, such as threshold exceedances, localized damage, or settlement warnings. These insights are derived from the simulation and dynamic evolution of the virtual model, which has been continuously updated using field data from the physical system.

Current applications of digital twin technology in bridge management are largely focused on bridge predictive maintenance [80, 42, 81]. For instance, Zhang et al. [82] proposed a digital twin framework applied to the prediction and simulation of vortex-induced vibration (VIV) in bridges, thereby providing technical support for maintenance decision-making. In this study, VIV field measurements were used to inversely update the parameters of the VIV model, and a mapping relationship between the VIV parameters and wind characteristics (such as wind speed and turbulence intensity) was established for future predictions. Similarly, Lin et al. [83] proposed a digital twin-based method for assessing the seismic collapse fragility of bridges. In their work, structural response data (acceleration and displacement) were first collected through seismic shake table experiments. Based on these data, model updating was performed, and a nonlinear digital twin model was developed to predict the collapse process under future seismic events. Furthermore, Hu et al. [84] systematically constructed a digital twin framework for fatigue life assessment. In this framework, robotic inspection systems were employed to collect structural data, deep learning techniques were used for crack detection, and finite element–crack co-simulation was applied for rapid prediction of the remaining fatigue life. Ultimately, fatigue life contour maps were generated to support decision-making for predictive maintenance.

In summary, this digital twin-based predictive maintenance approach has transformed the traditional maintenance strategy landscape. It not only offers high-fidelity simulation and prediction capabilities but also incorporates more intelligent decision-making mechanisms [85].

2.2. Uncertainties in masonry bridge and model calibrations

A distinctive feature of masonry bridges compared to other bridge types is their high level of uncertainty, particularly in terms of geometric features and material properties [25]. Geometric uncertainty occurs due to two factors: first, the lack of historical design drawings; and second, structural deformations or changes in support conditions caused by long-term service effects, such

as traffic loading, foundation settlement, and scour [86].

In addition to geometric uncertainty, material property variability presents another significant modeling challenge [87]. These variations include not only differences in mechanical parameters across different locations of the structure, but also time-dependent degradation effects such as aging. For instance, Dorji et al. [31] conducted coring and experimental testing on various locations of a masonry bridge in Australia that had been in service for over 100 years. Their results showed that the compressive strength of the sampled cores ranged from 8.7 MPa to 13.1 MPa, while the tensile strength ranged from 0.6 MPa to 2.1 MPa. This variability indicates significant spatial heterogeneity in material properties. Moreover, the geometry uncertainty is further exacerbated by the time-dependent aging behavior of masonry materials [88].

However, obtaining such property data through direct sampling is extremely challenging in practice. The vast majority of masonry bridges are protected as historical structures, where invasive testing is strictly prohibited. This constraint further increases the difficulty in obtaining accurate material parameters for structural assessment and modeling.

Both geometric conditions and material properties of masonry bridges are closely related to their scour behavior. From a geometric perspective, scour-induced failures are fundamentally caused by changes in the boundary conditions of the foundation, leading to the loss of structural support. From a hydraulic standpoint, both the depth and morphology of scour are highly influenced by the geometry of the pier foundation, particularly the embedment depth of the foundation top and the ratio between pier shaft and foundation diameter [89]. In addition, the dimensions of local components, contact conditions, and geometric imperfections also play critical roles in determining failure modes. For instance, the interaction between spandrel walls and backfill materials significantly affects structural behavior [90], and the thickness of the arch ring is often a dominant factor in the ultimate load-bearing capacity of masonry bridges [91].

Material properties also have a significant impact on failure risks and mechanisms. For example, failure modes between adjacent arches are found to depend on the mechanical properties of the mortar joints, such as cohesion, tensile strength, and friction angle [92]. Furthermore, the global structural response of masonry bridges is strongly influenced by the density, compressive strength, and tensile strength of the masonry units and the fill material [93].

In summary, geometry and material uncertainties are the main issues of accurately modeling the features of a masonry bridge, at the same time these uncertainties have a profound impact on the mechanical response of the structure. Therefore, it is crucial to calibrate the geometry and materials of a masonry bridge.

2.2.1. Calibrations in geometry

For historical structures such as masonry bridges, engineering documentation is often unavailable or incomplete, making geometric reconstruction necessary. Common reconstruction methods include total station surveying, photogrammetry, and terrestrial laser scanning (TLS) [93].

A traditional manual measurement method for masonry structures is total station surveying. It

enables the accurate measurement of key parameters such as span length, arch rise, and intrados radius, and can also be used to locate cracks and surface irregularities. The method offers high precision for short-range measurements, with a typical distance accuracy of ±2 mm [94]. However, manual surveying can be limited by accessibility issues, particularly when parts of the bridge are difficult to reach. In such cases, long-range measurements tend to introduce larger errors.

Photogrammetry is a 3D reconstruction technique based on image processing and geometric computation. It involves capturing multiple photographs from different viewpoints and orientations, followed by image alignment and matching with high overlap. Through processes such as image orientation, dense point cloud generation, and mesh reconstruction, a high-fidelity 3D model of the structure can be created [95].

The application of photogrammetry methods began with the use of handheld high-resolution cameras. For example, Riveiro et al. [96] employed a Canon EOS 10D to perform photogrammetric measurements of the Cernadela bridge. Control points were first placed, and their 3D coordinates were determined using a total station. The images were then processed using PhotoModeler software to reconstruct a high-precision 3D model containing approximately 25,000 points. Stavroulaki et al. [97] combined photogrammetry with ground penetrating radar (GPR) to assess the same bridge. During image acquisition, the camera's principal directions were kept at a 90° convergence angle to optimize stereoscopic coverage. In the data processing phase, internal, external, and absolute orientation steps were applied to reconstruct a globally referenced 3D model. The general process of geometry reconstruction is illustrated in Figure 2.4.

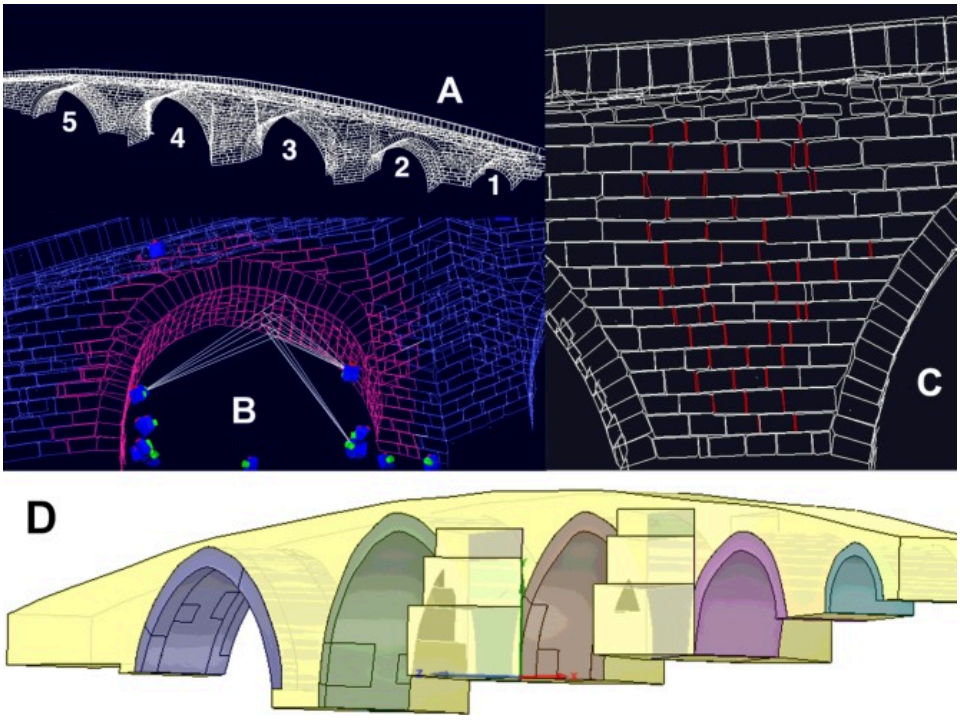

Figure 2.4: the process of creating the 3D model by photogrammetry [97]

In recent years, the use of unmanned aerial vehicles (UAVs) equipped with high-resolution cam-

eras for photogrammetry has gained increasing attention. Compared to handheld cameras, UAVs offer improved accessibility to bridge deck areas and allow for 360° image acquisition without blind spots. For instance, Pepe and Costantino [98] utilized an Anafi Parrot UAV equipped with a 21 MP CMOS camera to capture approximately 800 images of the Ponte del Diavolo arch bridge. A total station was employed to obtain 3D coordinates for image registration and georeferencing. Then, mesh and texture reconstructions were performed using standard photogrammetric processing techniques. The notable feature of this study is that each bridge component was modeled individually and linked with maintenance metadata to construct a BIM. Other relevant research using UAVs for the reconstruction of geometry can be found in [99, 100].

Another powerful tool for geometry reconstruction is TLS. TLS provides non-contact, high-density point cloud data with millimeter-level accuracy, making it superior to traditional total station surveying or photogrammetry in capturing fine surface details and textures. Other key advantages of TLS include its independence from natural light sources, and the elimination of the need for wiring or physical markers [101]. Furthermore, TLS offers a higher degree of automation in both data acquisition speed and post-processing compared to image-based methods [102].

For example, Riveiro et al. [103] conducted a TLS survey of the Cernadela bridge using ten scan stations, successfully capturing the full 3D point cloud of the entire structure. The data enabled the identification of key structural features such as span asymmetry and spandrel wall protrusions, demonstrating the potential of TLS for high-precision geometric measurement of masonry structures. Similarly, Armesto et al. [104] applied TLS to the Segura arch bridge for geometric modeling and deformation analysis. Their study also successfully revealed asymmetries between the two arches.

Talebi et al. [105] proposed a digitally enhanced visual inspection framework for non-contact structural assessment of masonry railway bridges in the United Kingdom. The framework integrates multiple technologies, including TLS, UAV, infrared thermography (IRT), and 360-degree imaging. In this context, TLS was mainly utilized to generate accurate geometric models of the bridge and to localize surface damage such as swelling, spalling, and cracking.

Willkens et al. [106] integrated TLS with BIM for bridge documentation. A total of 72 scans were conducted using a laser scanner with an accuracy of ±2 mm to generate dense point cloud data. The point cloud was imported into ReCap and Revit for model development. The process is shown in Figure 2.5. The study also highlighted certain limitations; specifically, parts of the bridge, such as underwater piers, were difficult to capture using TLS. These components were instead modeled using available engineering drawings or other data sources.

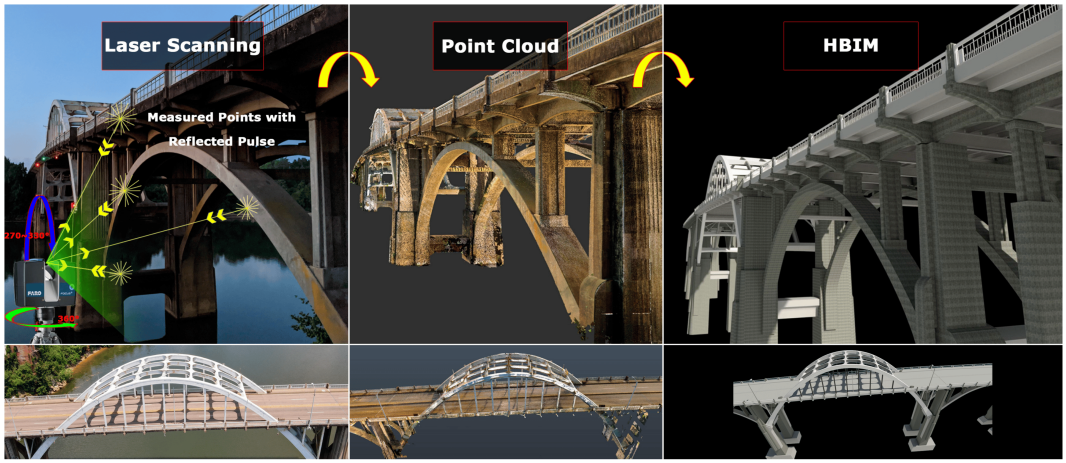

Figure 2.5: The process from laser scanning to BIM [106]

Lubowiecka et al. [107] proposed a nondestructive testing methodology for masonry bridges that integrates TLS, GPR, and FE analysis. The TLS component involved ten scan stations and employed a dual-resolution strategy combining high- and low-resolution scans. Post-processing steps included point cloud registration using the iterative closest point (ICP) algorithm, triangulated mesh generation, orthophoto creation, and CAD output. GPR was used to supplement information on internal fill materials. The final geometric model was subsequently applied in FE modal analysis.

2.2.2. Calibrations of material

The material uncertainty of masonry bridges is reflected not only in the variability of mechanical parameters, but also in the spatial heterogeneity of material distribution. There are two main approaches to address this uncertainty. The first involves the use of NDT methods to estimate key mechanical properties and investigate the non-uniform distribution of materials. The second approach is to apply modal analysis for model updating.

A commonly used nondestructive testing technique for masonry bridges is GPR, which can detect the thickness of the arch ring, the interface between the arch and the backfill material, and potential voids within the backfill [107, 108]. As previously discussed, GPR is often integrated with other geometric surveying techniques such as photogrammetry and terrestrial laser scanning [109, 99, 107, 110] to create a complementary system. While photogrammetry and TLS provide high-resolution external geometry, GPR offers internal subsurface profiles in one or two dimensions, which is crucial for the completeness of geometric and material data for structural modeling.

Another commonly used NDT method is the sonic or ultrasonic technique. In theory, ultrasonic testing can be used to estimate the dynamic Young's modulus of masonry materials, based on classical wave propagation theory. However, as demonstrated in the study by Brencich and Sabia [111], where the sonic wave method was compared with core sampling tests, the results of sonic testing were found to be largely influenced by the heterogeneity and anisotropy of masonry

materials. This discrepancy highlights the limitations of classical assumptions, which presume wave propagation in an elastic, homogeneous, and isotropic medium. Therefore, sonic technique may be suitable only for preliminary estimations of the elastic modulus.

Comparative studies show that only a limited number of NDT techniques are capable of capturing the spatial distribution of mechanical properties. This limitation is largely due to the high heterogeneity of masonry, which complicates the identification of representative material parameters for numerical modeling.

Due to the challenges in accurately determining material parameters through NDT techniques, and the limitations imposed on destructive testing by the heritage value of historical structures, alternative approaches are required. One widely adopted solution is modal updating based on structural dynamic parameters. This method first measures the dynamic response of the structure, typically in the form of accelerations [112], under either artificial or ambient excitation. Modal identification techniques are then used to extract key dynamic properties, including natural frequencies and mode shapes. These modal parameters are compared with the results from finite element modal analysis [113, 114]. The next step is to minimize the discrepancy between the experimental and numerical modal characteristics by iteratively adjusting mechanical parameters using an optimization algorithm [115, 116]. This iterative process allows the structural model to be calibrated for a more accurate representation of the actual behavior of the masonry bridge.

A clear distinction must be made between operational modal analysis (OMA) and experimental modal analysis (EMA), as the choice of method can significantly affect its applicability to masonry bridges. OMA utilizes ambient excitations such as wind, traffic, or water flow, whereas EMA requires controlled artificial excitations, typically through impact hammer tests. In practice, OMA is more suitable for masonry bridges, since EMA demands strong and well-controlled excitations. Such requirements are difficult to achieve due to the high mass of masonry structures and may even risk causing damage, particularly in heritage assets.

One notable application of OMA in masonry bridges is presented by Scozzese et al. [114], who employed the stochastic subspace identification (SSI) method to extract modal parameters from acceleration data for model calibration. Similar ambient-based calibration methodologies have been employed in other studies as well [117, 118, 119].

2.3. Failure mechanisms of bridges under scour

In the context of bridge structures, *failure* is defined as the incapacity of a bridge or its components to perform as intended in the original design and construction [14]. Besides total or partial collapse, substantial damage or deformation that prevents the structure from fulfilling its intended function is also considered failure.

In masonry bridges, scour-induced failure may behavior locally as stress redistribution and globally as overall structural instability, particularly when pier foundations become exposed. Current research on scour-induced failure mechanisms follows two main approaches. The first involves analytical models based on classical static equilibrium, as exemplified by Heyman's work on ma-

sonry arch behavior under limit conditions [34]; The second relies on finite element analysis to simulate local and global structural responses under scour-induced boundary changes [114, 120, 6, 121].

2.3.1. Analytic solution

Heyman [34] introduced the four-hinge mechanism based on static equilibrium and plastic theory, which remains a widely used analytical model for describing arch failure mechanisms. When scour occurs, it alters the distribution of internal bending moments within the arch. This redistribution is the fundamental principle behind the four-hinge mechanism. A plastic hinge forms when the internal bending moment at a specific location reaches the material's yield threshold. As plastic hinges form, the arch transforms from a statically determinate structure into a hinge-connected system that allows rotational movement. This transformation reduces the structural stability and may eventually result in collapse.

Building upon Heyman's limit analysis theory, Audenaert et al. [122] formulated differential equilibrium equations for masonry continuum elements based on fundamental static equilibrium. A perfectly elastoplastic material model was assumed, accounting for the compressive strength of masonry while neglecting its tensile capacity. Within this framework, the authors defined a plastic hinge formation criterion using a normalized axial force–moment space, in which the interaction between axial force and bending moment is represented through a failure envelope.

Similarly, based on limit analysis theory, George and Menon [123] assumed that masonry structures are characterized by zero tensile strength and infinite compressive strength, and structural instability occurs when a sufficient number of plastic hinges form. They classified scour-induced failures of masonry bridges into four potential mechanisms, as illustrated in Figure 2.6. The first mechanism, two abutment rotation (TAR), is featured by simultaneous rotation at both abutments, leading to the progressive formation of a complete collapse mechanism starting from the arch springings. The second mechanism, one abutment rotation (OAR), involves instability at only one abutment, along with a partial mechanism that causes localized cracking and deformation of the arch ring. The third mechanism, two pier rotation (TPR), involves hinge formation within a three-span structure spanning between two scoured piers. The final mechanism, one pier rotation (OPR), involves the rotation of a single pier foundation due to scour.

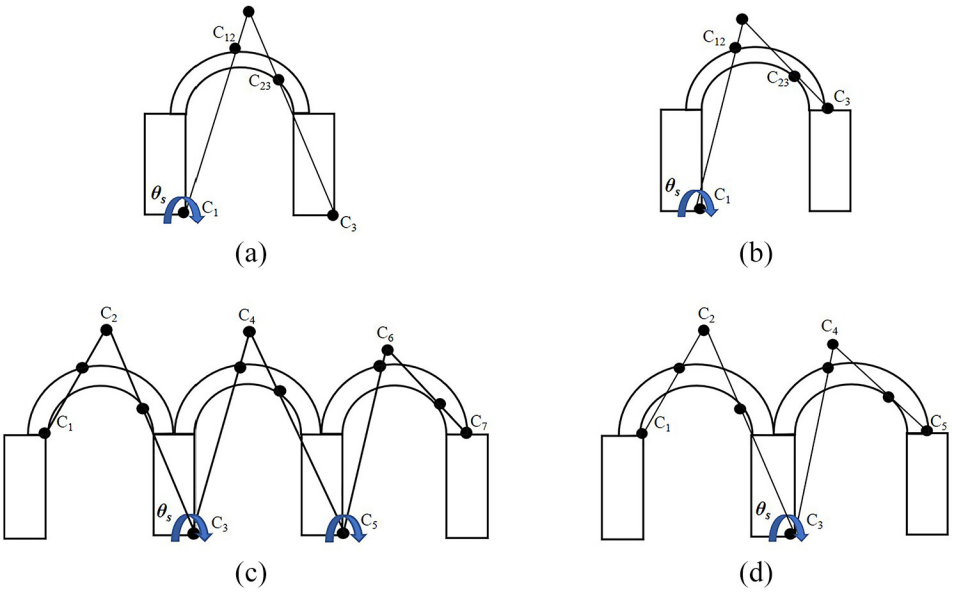

Figure 2.6: Failure mechanism for a masonry arch bridge by limit analysis: (a) two abutment rotation (TAR); (b) one abutment rotation (OAR); (c) two pier rotation (TPR); (d) one pier rotation (OPR) [123].

2.3.2. Finite element analysis

FE modeling approaches for masonry structures are commonly classified into two major categories: micro-modeling [124, 125] and macro-modeling [126, 90]. In micro-modeling, individual bricks and mortar joints are modeled separately, with interface elements introduced to simulate cracking between them. While this method offers high fidelity, it demands a high computational cost. Micro-modeling approaches are generally unsuitable for structures with large dimensions and complex geometry due to their computational cost. In contrast, macro-modeling treats the masonry as a homogenized anisotropic continuum, without explicitly differentiating between bricks and mortar. This approach is widely adopted for large-scale structural analyses due to its computational efficiency and stability.

As mentioned earlier in Figure 1.3, scour can be classified into symmetric and asymmetric types in the transverse direction. Symmetric scour occurs when the scour around the pier or abutment is geometrically symmetric, typically resulting in vertical settlement of the foundation. In contrast, asymmetric scour arises when the scour pattern is geometrically asymmetric, leading to tilting rotation or inclined displacement [127]. In the other research, Zampieri et al. [6] showed that masonry bridge failure is mainly caused by global settlement or local stress concentrations. The global failure mode results from uniform pier settlement under symmetrical scour. In contrast, local failure occurs when asymmetrical scour induces stress concentrations, especially in critical components like the arch ring. Both failure modes are represented as rigid body block sliding rather than material crushing failure, since it is understandable that masonry usually has a considerably high compression strength.

Moreover, existing studies typically consider severe damage and loss of serviceability of masonry bridges as the basis. The focus is on identifying strong indicators from finite element analyses to

assess and describe structural health state. For example, in the study by Zampieri et al. [6], the considered indicators included crack propagation in the arch ring, pier settlement, and the shear-to-normal force ratio (V/H). Among these, V/H (namely, shear force V and normal force H) was identified as a critical quantitative indicator of failure; numerical simulations revealed that when V/H>0.6, sliding instability occurs in the arch segments.

Similarly, Scozzese et al. [114] simulated the scour process by simplifying the soil–structure–water interaction into a Winkler spring system, sequentially removing springs on the upstream and downstream sides. In their study, both structural and dynamic response-based indicators were proposed. Structural indicators included pier settlement, plastic strain in critical regions, Von Mises stress, and the development of diagonal cracking. Dynamic indicators mainly involved reductions in natural frequencies and changes in mode shapes. Through numerical simulation of the scour-induced failure process, they determined that a scour depth of 5.5 m corresponded to the critical structural failure state. In a following study, Scozzese et al. [16] further defined damage states using the development of plastic strain and crack patterns.

2.4. Summary

This section systematically reviews the current state of research on scour monitoring and maintenance, uncertainty quantification, and failure mechanisms in the context of masonry bridges.

Scour monitoring techniques have evolved from conventional visual inspections to NDT methods such as sonar and radar. This transition addresses the subjectivity and safety risks associated with visual assessments. However, most NDT techniques provide only discrete, one-time measurements and are ineffective during flood peaks, making it difficult to determine the actual maximum scour depth.

FBGs have been increasingly utilized for scour monitoring. They can track changes in scour depth over time. When protected by suitable layers, FBGs also enable dynamic monitoring during pre-flood, peak-flood, and post-flood conditions. Nonetheless, such systems only provide strain information. Engineers must then infer the position of the water–sediment interface based on the strain data and use it to estimate how the scour depth evolves. Ideally, FBGs can inform about on-site scour progression; however, these systems do not directly assess structural performance or identify the critical threshold for failure. Maintenance decisions are still dependent on empirical guidelines, such as classifying foundations as shallow or deep and prescribing ”maximum allowable scour depths [128],” which often lack physical justification. Moreover, in field applications, FBGs often face durability issues during flood events. The sensors are vulnerable to damage from debris impacts and struggle to maintain performance under such harsh conditions [56, 129].

SHM has facilitated the evolution of bridge maintenance strategies from preventive maintenance to condition-based maintenance. However, existing CBM approaches still rely on SHM systems that provide structural response data under specific, and often unknown, loading conditions. Typical response variables include strain, changes in natural frequencies, and mode shapes. It remains unclear whether these responses accurately reflect the safety and serviceability of the

bridge superstructure. Consequently, CBM often depends either on expert systems with empirically defined thresholds, which may introduce subjectivity, or on machine learning models trained on limited datasets, which are prone to overfitting due to insufficient high-quality training samples.

To assess the safety and serviceability of the structure under a given scour depth, FEM serves as an effective tool. As discussed in Section 2, FE modeling of masonry bridges involves two major sources of uncertainty compared to other bridge types: geometric and material uncertainties. Geometric uncertainties arise from the lack of historical design drawings and long-term deformation due to aging and environmental exposure. To reduce such uncertainties, three geometric reconstruction methods have been considered: total station-based manual surveys, photogrammetry, and TLS. Among these, TLS is particularly promising for masonry structures, as it captures finer geometric details and is less sensitive to ambient lighting conditions [130].

Material properties are also uncertain due to the prohibition of destructive testing and inherent material heterogeneity. Although NDT techniques like GPR and sonic testing have been explored, their effectiveness in characterizing internal variability is limited. Model updating offers an alternative. This method corrects the material parameters in FEM through modal identification and optimization algorithms, improving accuracy in representing structural behavior.

After model calibration, it becomes essential to understand the failure mechanism of masonry bridges so that FE analysis can be deployed. Classical limit analysis based on the four-hinge arch theory assumes that the formation of a fourth plastic hinge potentially induced by pier rotation due to scour, which then destroys the static determinacy of the structure and finally leads to failure. However, such approaches assume zero tensile strength and infinite compressive strength for masonry, which are not realistic. Consequently, recent studies prefer FE analysis to simulate the failure process under scour conditions. Most existing work focuses on identifying effective indicators to define failure. However, to the best of the author's knowledge, no study has yet addressed how these failure indicators can be integrated with SHM systems or how both can be jointly utilized for predictive maintenance of masonry bridges.

To address this gap, the present study develops a digital twin framework that integrates sensor data with physics-based FE simulations. Unlike previous approaches that treat monitoring and modeling in isolation, the proposed framework enables dynamic model updating, allowing structural behavior to be assessed under evolving scour conditions with enhanced accuracy. To the best of the author's knowledge, this study is the first to integrate SHM-based scour monitoring and FE-based modeling into a unified digital twin system. It is specifically designed for historical masonry bridges that are at risk of scour failure.

3 Methodology

3.1. DT-based framework for scouring

This section introduces a digital twin-based monitoring and maintenance framework tailored for scour assessment in masonry bridges. As shown in Figure 3.1, the framework consists of three main components: the physical entity, the connection layer, and the virtual twin model. These components collaborate in a closed-loop configuration to achieve timely condition awareness of bridges under scouring.

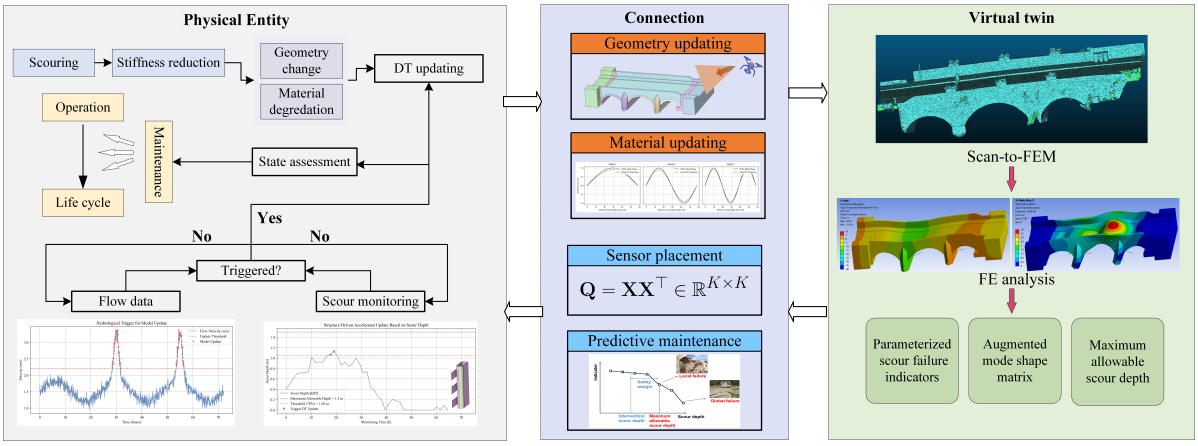

Figure 3.1: Digital twin framework for scour

Physical entity The physical entity refers to the actual bridge structural system, including its operational conditions, maintenance activities, lifecycle data, environmental monitoring data (such as flow data), and structural geometry. In this study, the evolution of the physical entity is primarily characterized by stiffness degradation at the bridge foundations, induced by scour processes. The physical entity consists of two main modules. The first is the digital twin updating module, which employs both routine and event-based updating mechanisms, where events are primarily triggered by hydraulic and scour measurements. The second module is the scour maintenance module, which integrates finite element analysis with field measurements of scour depth and structural failure indicators to develop targeted maintenance strategies. A detailed discussion of these two modules is provided in Section 6.2.

Connection layer The connection layer links the physical system and the virtual model through two loops:

- *Forward loop:* Structural response data collected by sensors are used to correct and update the material parameters of the finite element model, enabling a digital mapping of the physical system. In addition, point cloud data obtained through laser scanning can be used for geometric model corrections.

- *Backward loop:* This loop aims to utilize the feedback information from the virtual layer to inform engineering decisions at the physical layer. In this study, decision support includes two aspects: optimizing sensor placement and predictive maintenance strategies.

Virtual twin The virtual twin is the core component for predictive simulation and comprises the following modules:

- *Scan-to-FEM:* Structural geometric modeling based on three-dimensional laser scanning point cloud data, generating finite element models suitable for analysis.
- *Finite element analysis:* Construction of a Winkler foundation model with spring boundaries to simulate structural response variations under different scour depths.
- *Output indicators:* Outputs include augmented mode shape matrices, maximum allowable scour depth, and other failure indicators to support the sensor placement optimization, the establishment of early warning thresholds and the maintenance planning.

This framework establishes a closed-loop system of perception, modeling, prediction, and decision-making. It enables timely awareness of structural conditions, tracking of scour evolution, and informed maintenance support. In contrast to conventional monitoring and maintenance systems, this framework offers not only improved predictive capabilities but also supports more intelligent resource scheduling.

3.2. Engineering background of Regent bridge

The Regent bridge is a three-arch masonry road bridge spanning the River Lagan, located in the town of Dromore, Northern Ireland, UK, as shown in Figure 3.2. According to historical records, it was constructed in 1811. Due to its distinctive architectural design and historical meaning, the bridge has been designated as a protected heritage structure. To date, the bridge still plays a critical role in regional transportation.

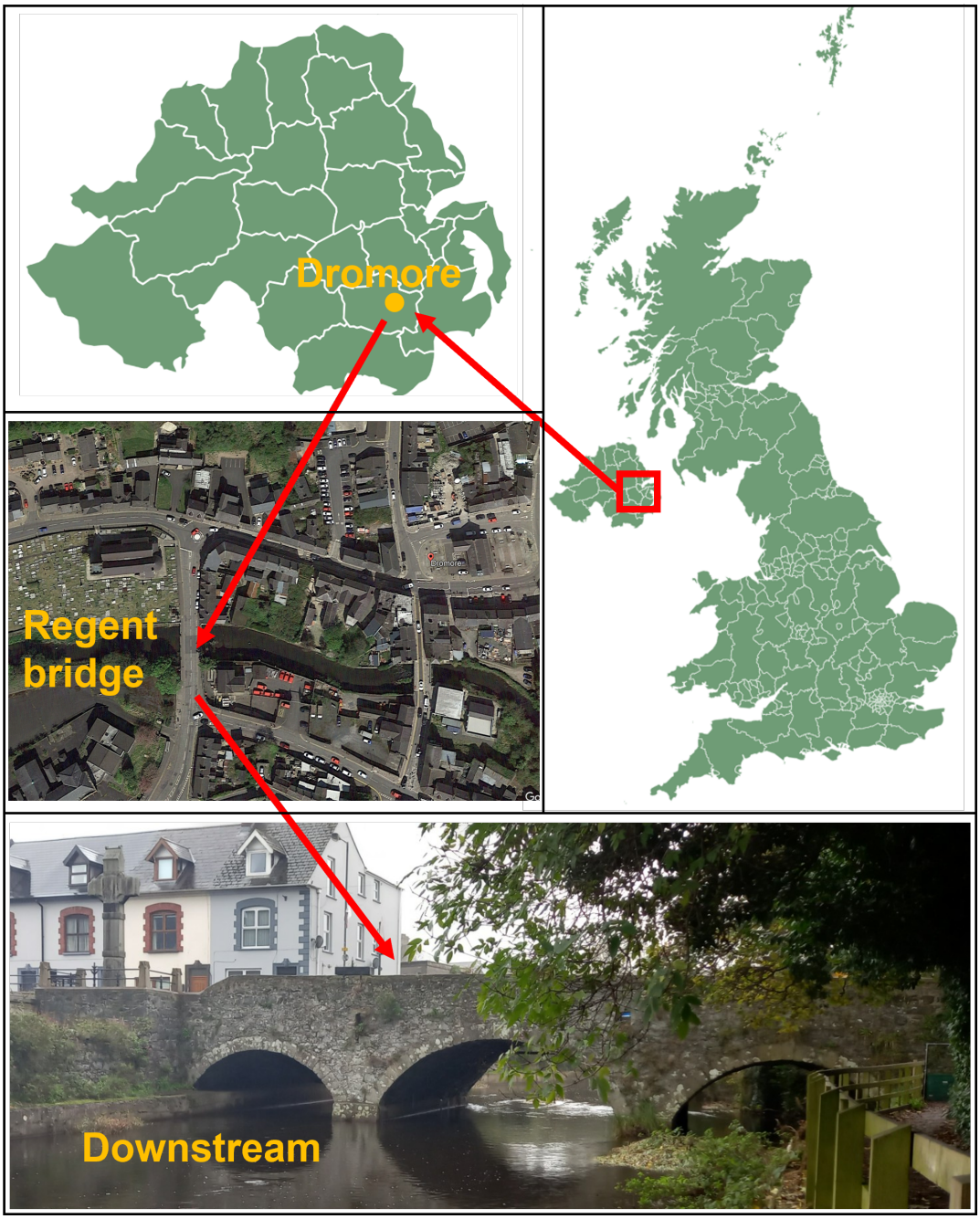

Figure 3.2: Regent bridge in the Dromore, Northern Ireland, United Kingdom

The key geometric dimensions of the Regent bridge are summarized in Figure 3.3. Due to prolonged exposure to water flow, the masonry bridge has experienced significant scour at the base of its piers. Additionally, localized issues such as cracking between joints and material loss can be observed on site.

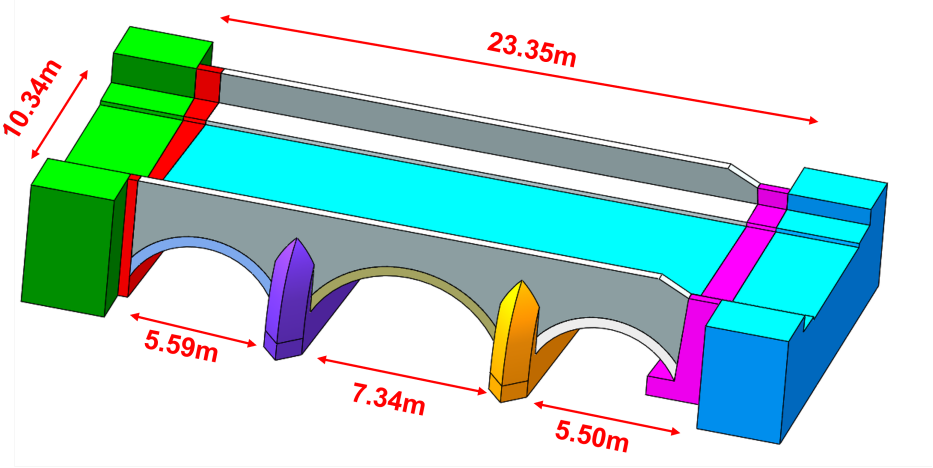

Figure 3.3: Longitudinal view of Regent bridge

3.2.1. Risk of flooding

Flooding is the external trigger of hydraulic hazards such as scour; therefore, investigation of the flooding risk is necessary. The Regent bridge is situated in Dromore, spanning the River Lagan. The River Lagan originates from the western slope of Slieve Croob in eastern Northern Ireland and flows for a total length of 45 miles (73 km) before emptying into Belfast Lough [131]. The nearest hydrological monitoring station to the bridge is the Drumiller House Station, which provides continuous measurement of water level.

Flood management in the Lagan River basin follows the three-step process established by the EU Floods Directive (Directive 2007/60/EC), which includes preliminary flood risk assessment (PFRA), flood hazard and risk mapping, and the development of flood risk management plans (FRMPs). In Northern Ireland, this directive was transposed into domestic legislation through the Water Environment (Floods Directive) Regulations (Northern Ireland) 2009, and its implementation is overseen by Department for Infrastructure (DfI) Rivers. The agency has developed the ”Strategic Flood Map (NI)” [132], which provides comprehensive flood risk information across the region to support spatial planning and risk management efforts aimed at reducing flood impacts.

According to records maintained by DfI Rivers, the Lagan River basin has experienced multiple flood events, particularly during periods of intense rainfall. For instance, as shown in Figure 3.4, the Dromore area has been affected by flooding on several occasions over the past decades, causing infrastructure damage and transportation disruptions. These historical events reflect the need for ongoing flood risk assessment and management in the region.

Figure 3.4: The flooding history near Dromore, based on official data from the Northern Ireland Flood Maps. *Data source: Flood Maps (NI), Department for Infrastructure (DfI), Northern Ireland.*

Given its location within the flood-prone zone of Dromore, the Regent bridge is susceptible to foundation scour during flood events. Therefore, it is essential to develop a targeted monitoring and maintenance framework, along with appropriate technical measures, to ensure the preservation of this historic structure.

3.2.2. Current monitoring and maintenance system for Regent bridge

Currently, a SHM system integrating multiple sensing technologies has been deployed on the Regent bridge to enable long-term tracking of scour risk and structural response behavior of this historic masonry arch bridge, as illustrated in Figure 3.5.

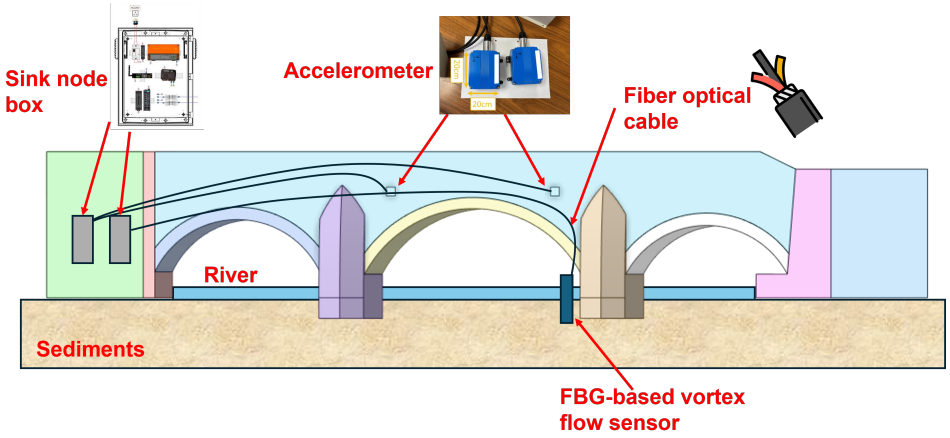

Figure 3.5: Current structural health monitoring system in the Regent bridge

First, a set of triaxial accelerometers has been installed on the upstream spandrel wall of the bridge to enable long-term vibration monitoring. These accelerometers are connected via LAN cables to a sink node, allowing real-time transmission of vibration data to a remote server. A fast Bayesian FFT algorithm is employed to detect changes in lateral modal frequencies from the measured signals. This setup aims to detect variations in modal parameters when scour occurs.

Second, the bridge is also equipped with FBG-based vortex flow sensors installed within an ex-

isting scour hole around the pier. The sensor structure consists of three rubber fins embedded at different depths, each containing an FBG optical fiber. When exposed by flowing water, the fins undergo vortex-induced vibrations, generating strain responses that indicate the initiation, progression, and backfilling phases of the scour process. Each time a fin transitions from a buried to an exposed state, a significant increase in strain is observed and transmitted in real time to the data acquisition system. However, this monitoring system has not yet accumulated a sufficient volume of long-term historical data at present, and further monitoring and analysis are being planned.

In Northern Ireland, current bridge inspections are predominantly conducted in accordance with standards such as CS 450 [133], which categorizes inspections into general inspection, principal inspection, and special inspection. The typical inspection frequency is once every two years for general inspections and once every six years for principal inspections. Special inspections are triggered in cases of high scour risk or abnormal events. Additionally, CS 469 is utilized to classify the flooding risk level of bridges [134]. Engineers can make maintenance measures according to the risk level of specific masonry bridges.

4 Finite element analysis of masonry bridge under scour

4.1. Model calibration

The accuracy and reliability of a DT model depend on an appropriate calibration process that aligns the virtual representation with the physical structure. In this study, two main calibration approaches are considered: geometry calibration and material calibration.

Geometry calibration involves acquiring high-resolution point cloud data of the bridge using laser scanning technology. The point cloud is processed to reconstruct a three-dimensional geometric model of the structure, which is then used for the development of the FEM. This approach effectively reduces uncertainties in the geometric parameters of conventional structural models; thus, the high fidelity of FEM-based analysis can be assured.

The laser scanner emits laser beams and receives reflected signals to measure the distance between the device and the target point while simultaneously recording the horizontal angle and vertical angle. The spatial coordinates of the target point can be transformed from polar to local Cartesian coordinates. Point cloud data acquired from multiple scanning stations reside in different local coordinate systems and must be aligned into a unified reference frame through registration techniques. One of the most widely used methods is the iterative closest point (ICP) algorithm [135], which aims to compute a rigid transformation and a translation vector that best align the transformed point set to its corresponding reference points. After obtaining the three-dimensional coordinates via laser scanning and performing coordinate alignment, a 3D point cloud model can be constructed. This process involves planar or surface fitting, as well as point cloud denoising, which can be implemented using mainstream commercial software, such as CloudCompare employed in this study.

The second approach is the model updating method for material calibration. This technique involves placing accelerometers at key locations of the bridge structure to extract dynamic features such as natural frequencies and mode shapes. These experimental modal parameters are then compared with those obtained from finite element modal analysis to inversely calibrate the material properties. This method is considered highly feasible and has been widely applied in the field of structural health monitoring [117, 136]. However, due to the limited number of accelerometers currently installed in the present case study, the spatial resolution and accuracy required for effective modal identification cannot be achieved. As such, this method has not been implemented in the current work. Nonetheless, it remains a promising direction for future research, particularly when sensor deployment strategies are further optimized and data acquisition systems are upgraded.

4.2. Scour progression simulation in FEM

To accurately simulate the scour process of the Regent bridge, a qualitative analysis of potential scour patterns is required. As illustrated in Figure 1.3, three typical scour patterns can be generally identified: symmetric lateral scour, asymmetric lateral scour, and asymmetric longitudinal scour along the river flow direction. The first step is to assess the likelihood of significant lateral asymmetry. Based on on-site inspections, no distinct asymmetrical scour pits were observed on either side of the piers. Furthermore, the bridge is located along a relatively straight reach of the River Lagan and does not sit on the outer bank of a meandering section, which are the conditions most often associated with asymmetric lateral scour. Based on these observations, this study considers only the symmetric lateral scour scenario in the direction perpendicular to the river flow. In other words, scour is assumed to occur symmetrically on both sides of the pier foundations along the bridge's transverse axis.

After understanding the lateral distribution of scour and the corresponding scour hole geometry, it is essential to examine its longitudinal distribution along the pier axis. Various experimental studies have provided valuable insights in this regard. For example, Pagliara and Carnacina [137] observed that the front portion of the scour hole has a steeper slope, while the rear part extends more gently, forming a characteristic "fish-tail" shape. Dargahi [138] provided a detailed description of the development of local scour around cylindrical bridge piers, summarizing the horizontal cross-section of the scour hole as a semicircle upstream and an elongated half-ellipse downstream. This concept was further simplified by Hoffmans [3], who reported that the upstream slope is approximately equal to the soil's natural angle of repose, while the downstream slope is generally more gradual, typically half that value.

In terms of numerical modeling, the scour geometry is often simplified as an inversed pyramidal shape in finite element simulations, as seen in the works of Tubaldi et al. [120] and Scozzese et al. [114]. Building upon these prior studies, the scour simulation concept adopted in this study is illustrated in Figure 4.1. The overall scour hole is idealized as an inverted pyramid in the longitudinal direction (z-z), where the upstream slope is set to the repose angle of 37°, based on soil sampling data from the surrounding site and observation that the angle of repose for loose sand is usually very close to the frictional angle [139]. The downstream slope is taken as half of this value. The scour process is simulated by progressively shifting the position of point O (from O1 to O2, then to O3, O4, etc.), with a fixed vertical increment of 0.5 m at each step. Throughout this evolution, the inverted pyramidal shape is maintained, and each O point corresponds to the location of maximum scour depth d. The ultimate goal of this simulation is to determine the maximum allowable scour depth, which represents the critical state at which the upper structure of the bridge loses its functional performance, that is, a generalized form of structural failure.

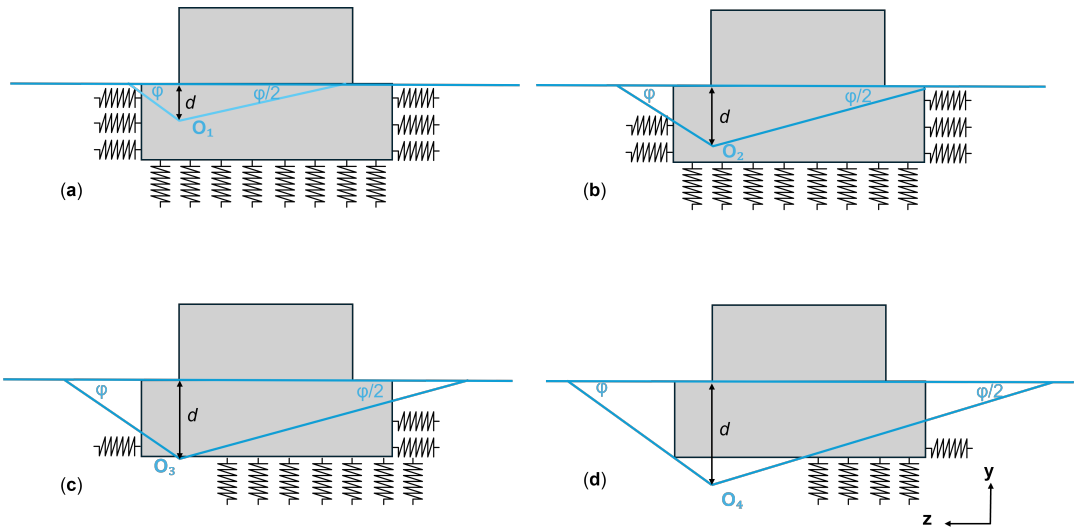

Figure 4.1: Illustration of the scour simulation process. (a) Scour depth = 0.5 m (Step 1); (b) Scour depth = 1.0 m (Step 2); (c) Scour depth = 1.5 m (Step 3); (d) Scour depth = 2.0 m (Step 4). Step 0 corresponds to the initial condition without any scour. The parameter d denotes the maximum scour depth, which progressively increases with each simulation step. Note that Steps 5, 6, and subsequent stages follow the same procedure, with further increases in scour depth.

4.3. FE Modeling

Finite element modeling serves as a critical component in this study, enabling the simulation of scour-induced failure processes and structural degradation in masonry bridges. Macro-models are adopted for the FE model and analysis because they are capable of effectively capturing the global failure mechanisms of masonry bridges [140, 141, 142]. The objective of the FE analysis is to simulate the scour-induced failure process and to identify indicators of structural degradation. These indicators will be integrated with time-domain scour monitoring techniques, forming the basis for the maintenance strategy within the proposed digital twin framework. In addition, FE simulations can provide the critical scour depth associated with structural failure, referred to as the maximum allowable scour depth in this study. This indicator is combined with field scour measurements, forming another key component of the predictive maintenance strategy.

4.3.1. Laser scanner data converted to FEM

To construct the finite element model, the geometric input was derived from terrestrial laser scanning (TLS) data of the Regent bridge. The original point cloud was reported in the .xyz file format. The .xyz format is a plain text (ASCII) point cloud data file that records the spatial coordinates of each point and, in this case, also includes RGB color information.

CloudCompare is an open-source 3D point cloud processing software [143], which was used in this study to process the point cloud data through denoising, filtering, downsampling, and registration. Through this series of procedures, the final meshed file was produced, as shown in Figure 4.2. It can be observed that the point cloud data miss some information within certain regions, particularly concerning the underwater parts of the piers and foundations. This limitation

is due to the rapid attenuation of visible light in water, which impairs laser scanner performance. In this study, the missing sections were primarily supplemented manually through on-site visual inspections and photographs. Although some uncertainty remains regarding the underwater geometry, this approach was deemed sufficient for generating a representative 3D model for the subsequent analysis. Future improvements may consider integrating sonar or underwater LiDAR to more precisely map the submerged regions.

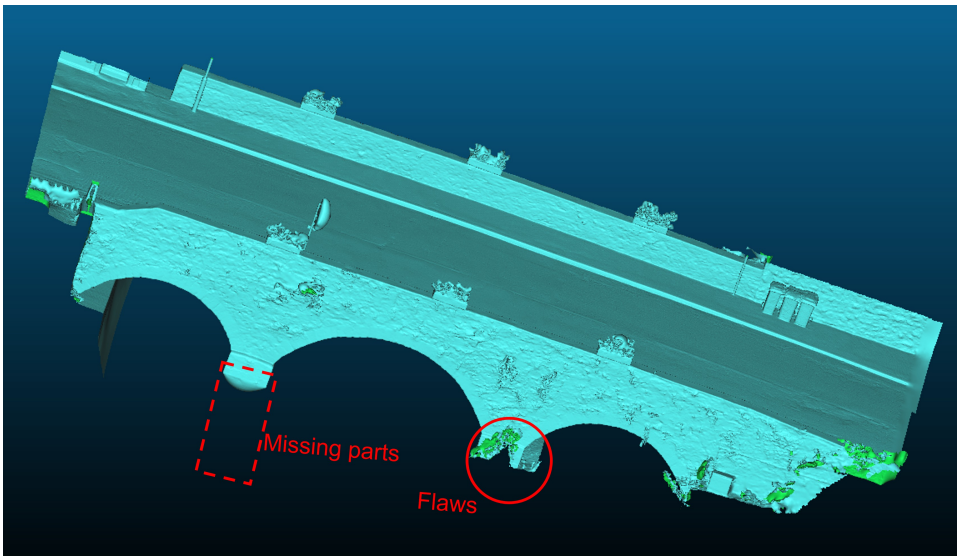

Figure 4.2: Mesh file generated from raw point cloud (by CloudCompare)

4.3.2. Geometry

The geometric model of the bridge was generated by importing an `.obj` file, which is obtained from processed point cloud data, and imported into a 3D modeling software. During this process, manual refinement was performed, mainly involving the following aspects: (1) Non-structural features such as decorations and railings on the bridge were manually removed; (2) As shown in Figure 4.2, the pier on the left side in the downstream direction showed evident scanning defects, which were repaired manually; (3) simplification of the foundation shape. Due to the inability of laser scanning to capture submerged components and the fact that the foundation is embedded in riverbed sediments, the actual foundation shape remains unknown. The foundation type of masonry bridges is typically shallow, with common forms including strip and spread footings. Regarding embedment depth, existing studies have shown that masonry bridges in Europe generally feature foundations embedded to depths between 1.5 m and 3 m [144, 145, 146]. As foundation geometry significantly influences post-scour stress redistribution, this study adopts a conservative modeling strategy by representing the foundation as an extension of the pier with an embedment depth of 1.5 m, which reflects the most likely scour-prone condition.

The final 3D geometry is illustrated in Figure 4.3, where the masonry bridge is discretized into components including the arch, spandrel walls, backfill, piers, and abutments.

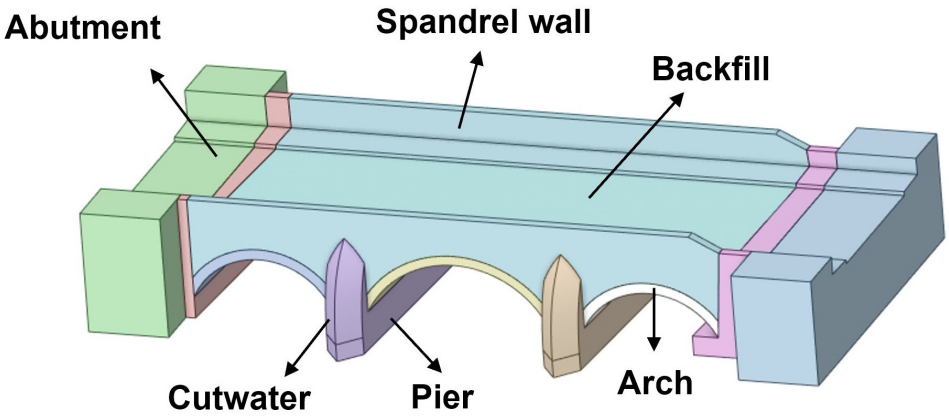

Figure 4.3: 3D geometry of the Regent bridge

4.3.3. Material parameters and constitutive models

The material parameters adopted in this study are partially derived from laboratory tests conducted on similar masonry bridges [31], and partially from values reported in existing literature [114, 120]. Table 4.1 summarizes the basic mechanical properties assigned in the simulation.

Table 4.1: Elastic material parameters used in the FE model

Material	E (GPa)	Poisson's ratio	Density (kg/m^3)
Abutment	11.0	0.20	1700
Backfill	0.22	0.25	1700
Brick of pier	1.45	0.20	1750
Brick of stone arches	3.10	0.20	1800
Spandrel walls	2.50	0.20	1800

In the masonry structure, the piers and spandrel walls are modeled using isotropic linear elasticity, which is a simplified strategy that reduces computational cost [147, 148]. However, the arch serves as the main load-bearing component and is often the critical location where transverse scour failure occurs [6]. Therefore, a more advanced material model is required. Previous studies have shown that the Drucker–Prager (DP) model can capture the plastic behavior of masonry [6, 149]. However, the classical version of this model uses a single yield surface and cannot reflect the significant difference between the tensile and compressive strengths of masonry [150]. Since masonry is typically much weaker in tension, this study uses the Drucker–Prager Concrete model in ANSYS, which defines separate yield surfaces for compression and tension to better simulate the behavior of weak-in-tension materials.

The general Drucker–Prager yield criterion is a pressure-dependent model commonly used to simulate geomaterials and concrete-like materials. The yield function is defined as:

$$F = \alpha I_1 + \sqrt{J_2} - k \leq 0 \tag{4.1}$$

where:

- I_1 is the first invariant of the stress tensor,
- J_2 is the second invariant of the deviatoric stress tensor,
- α and k are material parameters related to the internal friction angle and cohesion, respectively.

The post-peak softening behavior of masonry is captured using a linear hardening/softening model HSD6 [150]. This model defines the stress degradation in both tension and compression based on the hardening variable κ, which evolves during plastic loading. The evolution of κ is governed by the plastic flow and the current state of the stress field:

$$d\kappa = \sum_n d\lambda^n \left(\frac{1}{R\Omega} \boldsymbol{\sigma} \cdot \frac{\partial Q^n}{\partial \boldsymbol{\sigma}} \right)$$

Here, n denotes the number of active yield surfaces, $d\lambda^n$ is the plastic consistency parameter increment, R is the strength parameter, and Ω is the current value of the degradation function.

The hardening and softening behavior of the material (as shown in Figure 4.4) is governed by two degradation functions, $\Omega_c(k)$ for compression and $\Omega_t(k)$ for tension, both defined as piecewise functions of the k.

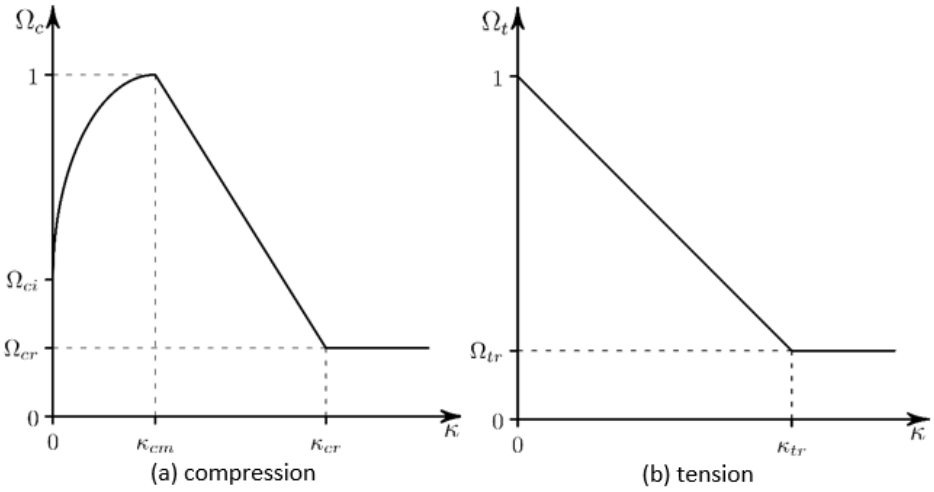

Figure 4.4: Hardening and softening in compression and tension of Drucker-Prager Concrete model [150]

Hardening and softening in compression

$$\Omega_c(\kappa) = \begin{cases} \Omega_{ci} + (1 - \Omega_{ci}) \sqrt{\dfrac{2\kappa}{\kappa_{cm}} - \left(\dfrac{\kappa}{\kappa_{cm}} \right)^2} & \text{if } 0 < \kappa \leq \kappa_{cm} \\ 1 - \dfrac{1 - \Omega_{cr}}{\kappa_{cr} - \kappa_{cm}} (\kappa - \kappa_{cm}) & \text{if } \kappa_{cm} < \kappa < \kappa_{cr} \\ \Omega_{cr} & \text{if } \kappa \geq \kappa_{cr} \end{cases} \tag{4.2}$$

Softening in tension

$$\Omega_t(k) = \begin{cases} 1 - (1 - \Omega_{tr})\dfrac{k}{k_{tr}} & \text{for } 0 < k < k_{tr} \\ \Omega_{tr} & \text{for } k \geq k_{tr} \end{cases} \tag{4.3}$$

Here, κ_{cm} and κ_{cr} represent the onset and ultimate values of compressive plastic strain, while κ_{tr} corresponds to the ultimate tensile plastic strain. The degradation functions are modulated by residual strength ratios: ω_{ci} and ω_{cr} for compression, and ω_{tr} for tension. The model also includes uniaxial and biaxial strength values to define the yield surface and flow behavior.

For quasi-brittle materials such as masonry, the plastic shear failure process is often accompanied by non-zero volumetric strain, known as dilation. This phenomenon affects the crack propagation path and the development of localization zones. To describe the volumetric expansion during inelastic deformation, the Drucker–Prager Concrete model uses two dilation parameters, C_1 and C_2. These parameters control the magnitude of volumetric strain associated with shear failure. Eventually, the parameters of DP Concrete model used in this study are as follows:

Table 4.2: Material parameters used in the Drucker-Prager Concrete (HSD6) model

Parameter	Description	Value
f_c	Uniaxial compressive strength	10.6 MPa [31]
f_t	Uniaxial tensile strength	1.34 MPa [31]
f_b	Biaxial compressive strength	12.72 MPa
κ_{cm}	Plastic strain at f_c	0.01026
κ_{cr}	Ultimate compressive plastic strain	0.05
ω_{ci}	Residual ratio at κ_{cm}	0.5
ω_{cr}	Residual ratio at κ_{cr}	0.5
κ_{tr}	Ultimate tensile plastic strain	0.002
ω_{tr}	Residual tensile stress ratio	0.3
C_1	Tensile dilation parameter	0.005
C_2	Compression dilation parameter	0.005

The backfill material of the masonry bridge behaves with pressure-dependent plastic behavior characteristic of granular media. Therefore the Drucker–Prager Concrete model is also used to describe its nonlinear shear response and plastic flow under loading. In this study, the ultimate strength parameters of the backfill material were assigned the following values:

- Uniaxial tensile strength = 20 kPa,
- Uniaxial compressive strength = 200 kPa,
- Biaxial compressive strength = 300 kPa.

4.3.4. Boundary conditions, load and contact relations

The boundary conditions of the finite element model are defined by constraining vertical displacements at both abutments to zero, which reflects the actual situation. As the abutments of the masonry bridge are connected to the main roadway, they are constrained only by the overall stiffness of the roadbed and the process of drainage consolidation. Under scour scenarios, the portions of the structure located within the river channel may experience relatively considerable displacements due to reduced foundation stiffness, whereas the abutments have negligible settlement. These areas with abutments predominantly exhibit slow, long-term settlements, namely secondary consolidation or long-term creep settlements of the subgrade.

A vertical pressure of 1.5 kPa was applied to the bridge deck to represent the weight of the asphalt pavement layer. This simplification aims to efficiently simulate deck loading while focusing computational efforts on the effects of scour.

The definition of contact interactions is important for correctly analysis the interaction between two or more structural parts. In the ANSYS environment, contact interfaces are classified into *Contact* and *Target* surfaces. During interaction, the contact surface is constrained from penetrating the target surface, whereas the target surface is allowed to penetrate the contact surface. The general modeling rule is to assign the contact surface to the component with lower stiffness or a higher likelihood of undergoing sliding or separation, and the target surface to the stiffer component.

Contact behavior can be broadly categorized into two types: linear and nonlinear. Linear contact assumes that the surfaces are either perfectly bonded or cannot separate, whereas nonlinear contact allows for separation and potential collision. Since nonlinear contact modeling significantly increases computational demand, a trade-off strategy is adopted in this study. Specifically, nonlinear *frictional* contact is defined between the backfill and the arch with a friction coefficient of 0.6, where strong nonlinear interaction is expected. In addition, critical contact pairs, namely, those between the arch and spandrel walls, and between the arch and piers, are also defined as frictional contacts with a friction coefficient of 0.3. This choice of friction coefficient is motivated by field observations of visible existing cracks at these interfaces, which may suggest initial sliding behavior; hence, a relatively low friction coefficient is assigned to ensure a conservative structural assessment. In contrast, the remaining contact piers, such as the spandrel wall-abutment contact pier, are assumed to be bonded (linear contact), since those piers are less important to the analysis of scour, and computational cost can be largely saved by this measure.

To improve the numerical convergence of nonlinear contact analysis, the *penalty method* is employed to enforce contact constraints. This method introduces virtual springs between the contact and target surfaces to establish their mechanical interaction. When no penetration occurs, the springs exert no force. Once penetration is detected, the springs generate a repulsive force according to Hooke's law to resist further penetration.

4.3.5. Element and mesh

To accurately represent both regular and irregular domains of the bridge geometry, two main types of elements were employed in the finite element model. The first is SOLID186, which is a second-order (20-node) 3D structural solid element and typically used for meshing regular regions. The second is SOLID187, which is a second-order (10-node) tetrahedral element and usually well-suited for irregular volumetric domains.

A region-based mesh refinement strategy was adopted in this study. Specifically, a coarse mesh size of 0.2 m was assigned to the abutment regions, as these components are unimportant, mainly serving to apply boundary conditions, and do not participate significantly in stress transfer. A medium mesh size of 0.1 m was applied to the spandrel wall and backfill areas, which are moderately sensitive to load transfer and thus require intermediate resolution. In contrast, a fine mesh sizing of 0.05 m was used in key structural components such as the arch rings and piers, where high stress concentrations and deformation gradients are expected, thereby calling for a more accurate mechanical response capture. This mesh configuration aims to ensure sufficient numerical accuracy while optimizing computational cost.

The final mesh consists of 13,986,319 nodes and 7,900,974 elements, including 6,885,093 second-order tetrahedral (Tet10) elements, 1,014,377 hexahedral (Hex20) elements, and 1,504 wedge (Wedge15) elements.

4.3.6. Stiffness of the Winkler model

To simulate the local scour process around the bridge foundation, this study adopts a staged scour modeling approach. As illustrated in Figure 4.1, an idealized inverted pyramidal scour hole geometry is used, with the slope of the upstream face set to the soil's angle of internal friction ϕ, and the downstream slope defined as $\phi/2$. The simulation begins from the initial state and incrementally increases the maximum scour depth d, with each stage representing a 0.5 m increment in depth. At each stage, elements located below the current d level are identified and progressively deactivated, thereby replicating the gradual degradation of foundation support due to scour.

A key aspect of employing the Winkler foundation method is to determine the coefficient of subgrade reaction, among which the axial stiffness of the Winkler springs is the most critical. Gazetas [151] proposed an approximate method for estimating the static stiffness of springs in the x-, y-, and z-directions based on the foundation's geometric dimensions, given by the following expressions:

$$K_z = \left[\frac{2GL}{1-\nu}\right]\left(0.73 + 1.54\,\chi^{0.75}\right) \tag{4.4}$$

$$K_y = \left[\frac{2GL}{2-\nu}\right]\left(2 + 2.50\,\chi^{0.85}\right) \tag{4.5}$$

$$K_x = K_y - \left[\frac{0.2}{0.75-\nu}\right] GL\left(1 - \frac{B}{L}\right) \tag{4.6}$$

where:

- G is the shear modulus of the soil, taken as 246 MPa, based on [152];
- ν is the Poisson's ratio, taken as 0.45;
- ρ is the soil density, taken as 1900 kg/m^3;
- L and B are the foundation length and width, respectively, measured as $L = 12.34$ m and $B = 1.52$ m;
- χ is the foundation shape factor, defined as $\chi = \dfrac{B}{4L} \approx 0.0308$;
- D is the foundation embedment depth, which was difficult to measure on-site; thus, following the modeling assumption in [146], it is taken as 1.5 m, which is a representative value for masonry bridge modeling.

Substituting the above values yields: a stiffness in the z-direction of $K_z = 9.31 \times 10^8$ N/m, a stiffness in the y-direction of $K_y = 8.34 \times 10^8$ N/m, and a stiffness in the x-direction of $K_x = 6.57 \times 10^8$ N/m.

4.4. Failure pattern and corresponding indicators of scour

In the context of scour, structural failure in masonry bridges is often localized rather than global. As shown in Figure 1.2(b), bridges in the real world usually did not collapse entirely; instead, significant localized structural damage occurred, making the bridge incapable of fulfilling its intended service performance. Therefore, such localized failure should also be regarded as structural failure. These findings highlight that failure should not be defined solely based on whether a full-span longitudinal tensile crack has formed. Even localized tensile failure in the arch may result in subsequent instability of the backfill and compromise the serviceability of the masonry bridge.

Moreover, in masonry structures, localized cracking typically results from a principal stress state exceeding the material's low tensile strength [153], as masonry material typically has much higher compression strength than tensile strength. This material property suggests that identifying potential local failure signals requires first examining the evolution of principal stress distributions during the scour process.

4.4.1. Stress redistribution during scour and the failure mechanism

To investigate the stress redistribution behavior during scour, this study examines the variation in maximum principal stress at representative nodes #162036 (left arch) and #216616 (middle arch). location of measurement points can be seen in Figure 4.6. As defined in Section 4.2, the scour progression was discretized into incremental stages by sequentially modifying the boundary stiffness of the Winkler foundation. As shown in Figure 4.5, the maximum principal stress remains approximately constant during the early stages of scour. This response is attributed to the gradual reduction of lateral soil confinement, while the bottom soil support remains relatively intact. However, once the scour depth exceeds approximately 1.5 m, the maximum principal stress at the left arch and middle arch sharply increase. This clearly demonstrates the potential stress redistribution process of the Regent bridge under scour conditions.

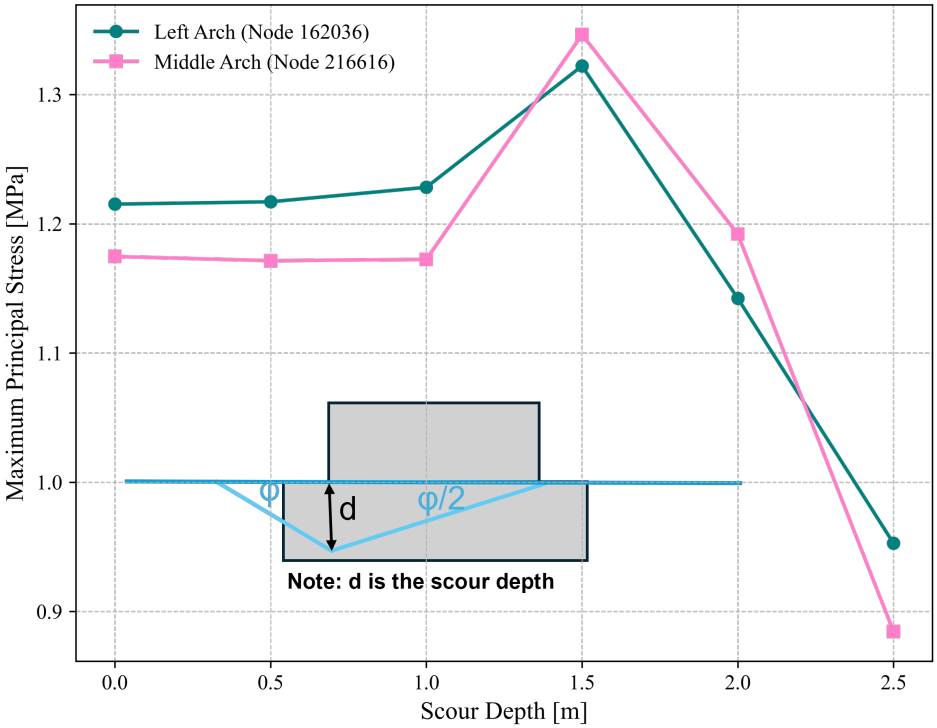

Figure 4.5: Maximum principal stress development under scour in the left and middle arch

According to tensile strength measurements of masonry bridges reported by Dorji et al. [31], the average tensile strength of masonry is approximately 1.34 MPa. As shown in Figure 4.5, the two arch measurement points are very close to this threshold at Step 3 (scour depth = 1.5 m), indicating the likely onset of localized failure and a partial loss of load-carrying capacity. At this stage, the maximum principal stress at both arches initially increases and then decreases with progressive scour. After scour depth 1.5m, with further scour, the structure likely enters a stress-releasing or softening state, leading to a decline in principal stress in both measurement points. This softening behavior corresponds to the material softening stage illustrated in Figure 4.4.

Figure 4.6 further illustrates the maximum principal stress distribution at Step 3 (corresponds to a scour depth of 1.5 m). At Step 3 of the simulation, continuous plastic stress bands were identified across the left and middle arches. Those stress concentrations were observed in the lower regions of the left and central arches, considerably higher than in other regions. This stress concentration phenomenon suggests that, due to the reduction in foundation stiffness and asymmetric structural geometry, the arch begins to exhibit a potential failure mode dominated by tensile stress at this stage, indicating a localized cracking risk.

Interestingly, this failure mechanism closely resonates with actual cases, as shown in Figure 1.2(a), (b), and (c), and is also similar to other numerical research [120, 6]. These cases suggest that the ultimate failure may involve localized tensile failure on both sides of an arch adjacent to a pier. The underlying mechanism is that scour progressively reduces the support stiffness of the pier foundations, leading to substantial vertical displacement in these zones. This stiffness reduction

creates a stress concentration region between the pier and the adjacent arch, where the arch intrados experiences combined bending moment and axial force. As a result, localized tensile stress is concentrated, promoting crack initiation and potential structural failure. Thus, tensile failure near the piers, typically around the quarter-span regions of the adjacent arches, represents a characteristic failure mode under scour conditions in masonry bridges.

In this study, the localized tensile cracking in Step 3 evolved from a single-span failure to simultaneous large-scale cracking in both side arches. These cracks formed a continuous failure plane, causing localized structural failure. As a result, the scour depth at Step 3 (1.5 m) is defined as the maximum allowable scour depth for this structure, beyond which structural safety can no longer be guaranteed.

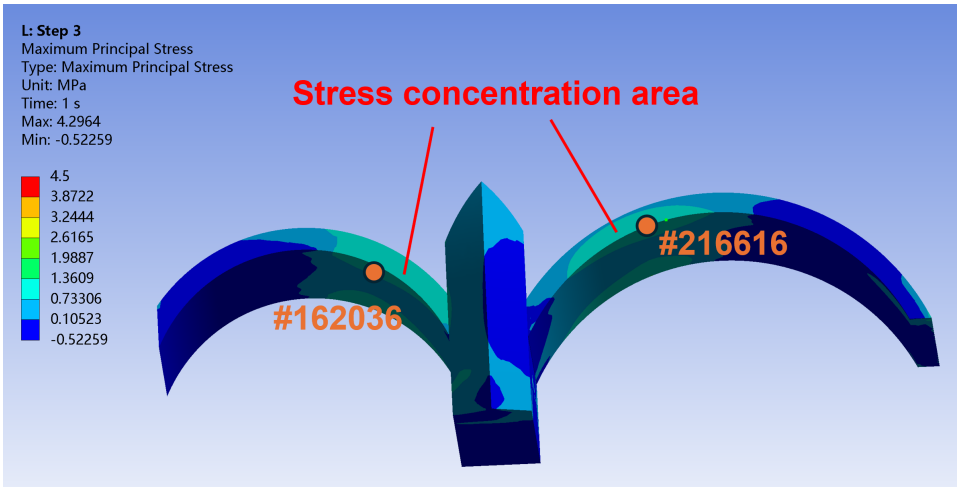

Figure 4.6: Stress concentration zones in the left and middle arches under Step 3 scour condition

The observed local failure occurs at the interface between the left and middle arches rather than on the right side. This asymmetry in failure location is attributed to the geometric asymmetry of the bridge, as the left span is longer than the right. Under uniform vertical loading on the deck and stiffness reduction on the piers, the longer left arch develops higher tensile strain at the intrados due to increased bending moments. This geometric sensitivity becomes more pronounced when the foundation stiffness beneath the left pier is reduced as a result of scour (Step3). As shown in Figure 4.7, this results in significant deformation at the left springing region, while the right spans remain relatively stable.

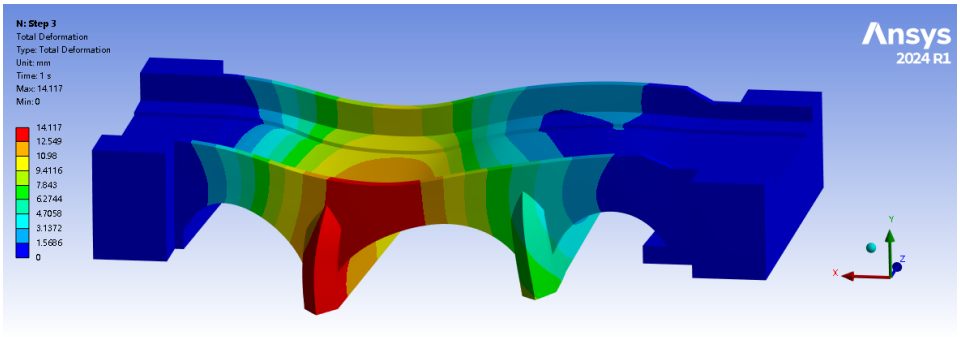

Figure 4.7: Total deformation when scour depth is 1.5m

Figure 4.5 and Figure 4.6 highlight the feasibility of using maximum principal stress as a failure indicator. However, in practical applications, directly measuring this parameter is very challenging. This limitation suggests the need to identify alternative monitoring quantities that are easier to measure and can serve as effective indicators of the scour-induced failure process.

4.4.2. Pier settlement and rotation

Scour can be interpreted as a gradual degradation of foundation stiffness. This degradation increases strain at the pier base and behaves as vertical displacement (y-y direction) and longitudinal rotation (z-z direction). Hence, pier settlement and rotation serve as direct indicators of scour progression. As shown in Figure 4.8, both the left and right piers show measurable settlement as scour depth increases, and the left shows a more pronounced response. In FE simulation, after the external loading and self-weight is applied, there is an initial settlement around 10mm, which is the benchmark value. The settlement is stable before the scour depth of 1 m. As scour depth increases, a distinct increase in settlement is observed after the scour depth reaches 1.5 m (Figure 4.9). More specifically, the pier settlement increases about 25% between scour depth 1 m and 1.5 m. This deformation acceleration coincides with the sharp variation in principal stress (as illustrated in Figure 4.5), further supporting the conclusion that 1.5 m can be regarded as a critical scour depth with the bridge approaching the failure.

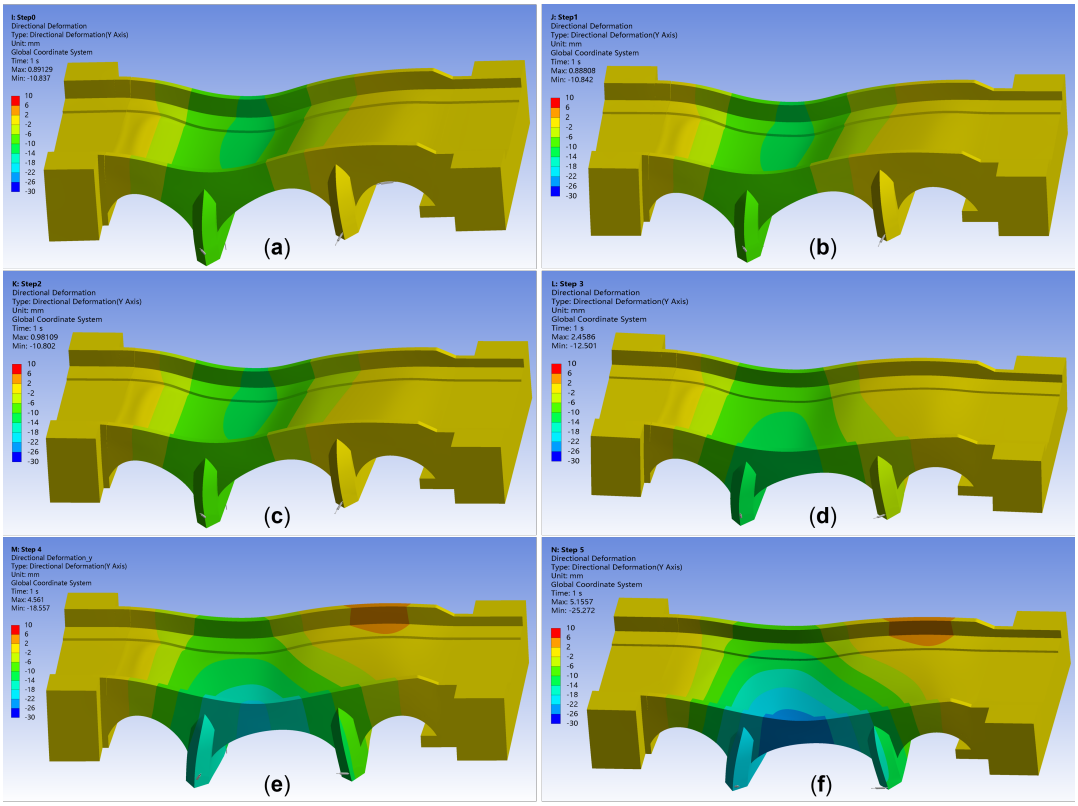

Figure 4.8: Pier settlement contour as the scour progresses. (a) scour depth 0m; (b) scour depth 0.5m; (c) scour depth 1m; (d) scour depth 1.5m; (e) scour depth 2m; (f) scour depth 2.5m. And note that the legend is from -40mm to +10mm, the Y axis is the same direction of the pier settlement

Settlement is relatively easy to monitor in practice. The displacement can be continuously captured by FBG sensors or strain gauges and can also be obtained from regional monitoring technologies such as interferometric synthetic aperture radar (InSAR). Moreover, compared to other monitoring techniques such as the vibration-based monitoring, settlement monitoring is usually less affected by the environment.

Another critical aspect to consider is the differential settlement. Due to the asymmetrical development of scour, the upstream side typically experiences a much faster progression of scour depth than the downstream side. This phenomenon is simulated in the FEM, where the repose angle of the upstream scour hole is set to be twice that of the downstream side. As shown in the FE analysis (Figure 4.9), in the early stage of scour (e.g., at a depth of 0.5m), the differential settlement between the upstream and downstream sides is limited to approximately 2mm. However, as scour deepens, particularly when the scour depth is beyond 1.5m, the differential settlement increases dramatically, eventually reaching approximately 16mm.

An interesting observation is that the downstream side shows a slight uplift during the early stage of scour. This can be explained by the simulation process illustrated in Figure 4.1. The masonry bridge has an unusually long foundation (12.34m), causing the initial scour to be concentrated primarily on the upstream side. As a result, the upstream pier experiences noticeable settlement,

while the downstream side remains largely unaffected at this stage. This leads to a slight rotational behavior of the entire pier foundation, resulting in a minor uplift at the downstream end. As scour progresses further and the scour pit gradually extends toward the downstream side, settlement also begins to develop there. As shown in Figure 4.9, once the scour depth reaches 2 m, noticeable settlement occurs at the downstream side as well.

Differential settlement between the upstream and downstream sides can cause longitudinal rotation (along z-z direction) of the pier foundation. This rotation can be effectively captured using inclinometers. Previous long-term monitoring studies have demonstrated the reliability and accuracy of such measurements [154]. More importantly, differential settlement is minimal during the initial stages of scour development, and no significant rotation is observed at this point. However, once the scour depth exceeds a critical value (approximately 1.5 m in this case), the differential settlement increases markedly, indicating the substantial rotation of the pier foundation between the upstream and downstream sides. This behavior can serve as another strong early warning indicator of potential structural failure.

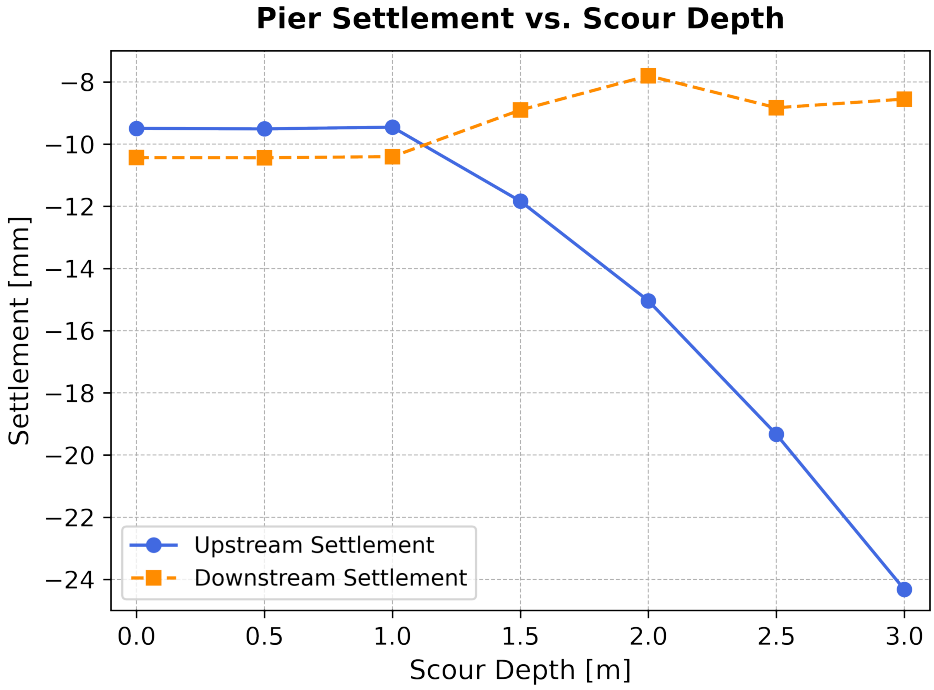

Figure 4.9: left pier settlement development as the scour progresses

4.4.3. Modal analysis

Scour can degrade foundation stiffness and affect the dynamic characteristics of structures. For instance, Prendergast et al. [155] found through experiments and field testing that the natural frequencies of pile foundations decrease notably as scour depth increases. In structural dynamics, scour reduces structural stiffness k_i, which in turn lowers modal frequency ω_i. The fundamental

relationship for modal frequency is given by:

$$\omega_i(y_s) = \sqrt{\frac{k_i(y_s)}{m_i}} \tag{4.7}$$

where y_s is the scour depth, and m_i is the effective mass corresponding to the i-th mode. Since scour weakens the foundation support, $k_i(y_s)$ is generally a monotonically decreasing function, which can be approximated linearly as:

$$k_i(y_s) = k_{i,0} \cdot (1 - \alpha_i y_s), \quad \text{for small } y_s \tag{4.8}$$

where $k_{i,0}$ is the initial modal stiffness, and α_i represents the sensitivity coefficient of mode i to scour.

Taking the derivative with respect to y_s, the sensitivity of modal frequency to scour depth is:

$$\frac{d\omega_i}{dy_s} = \frac{1}{2} \cdot \frac{1}{\sqrt{k_i(y_s)m_i}} \cdot \frac{dk_i(y_s)}{dy_s} \tag{4.9}$$

To more generally express the differences among modal responses to scour, a simplified model is introduced:

$$\omega_i(y_s) = \omega_{i,0} \cdot \sqrt{1 - \beta_i y_s} \tag{4.10}$$

where $\omega_{i,0}$ is the initial frequency of mode i, and β_i is the damage sensitivity coefficient, reflecting how sensitively the modal frequency responds to scour depth. A larger β_i indicates a faster decrease in the modal frequency.

In this case study, the evolution of the first six natural frequencies with scour depth was tracked. The modal shape at the initial stage (Step 0) is illustrated in Figure 4.10, and the variation of natural frequencies is shown in Figure 4.11. As seen from the figure, most modal frequencies gradually decrease as scour depth increases. However, some specific phenomena in Figure 4.11 need additional interpretation. Notably, a slight increase in the second natural frequency was observed, which may be attributed to a local redistribution of mass or change in boundary conditions, since the response of this mode concentrates in the left pier area (as illustrated in Figure 4.10B), which corresponds to the location where scour develops. Additionally, the fifth mode frequency drops sharply at a scour depth of approximately 1.5 m, suggesting that this mode is particularly sensitive to localized stiffness degradation.

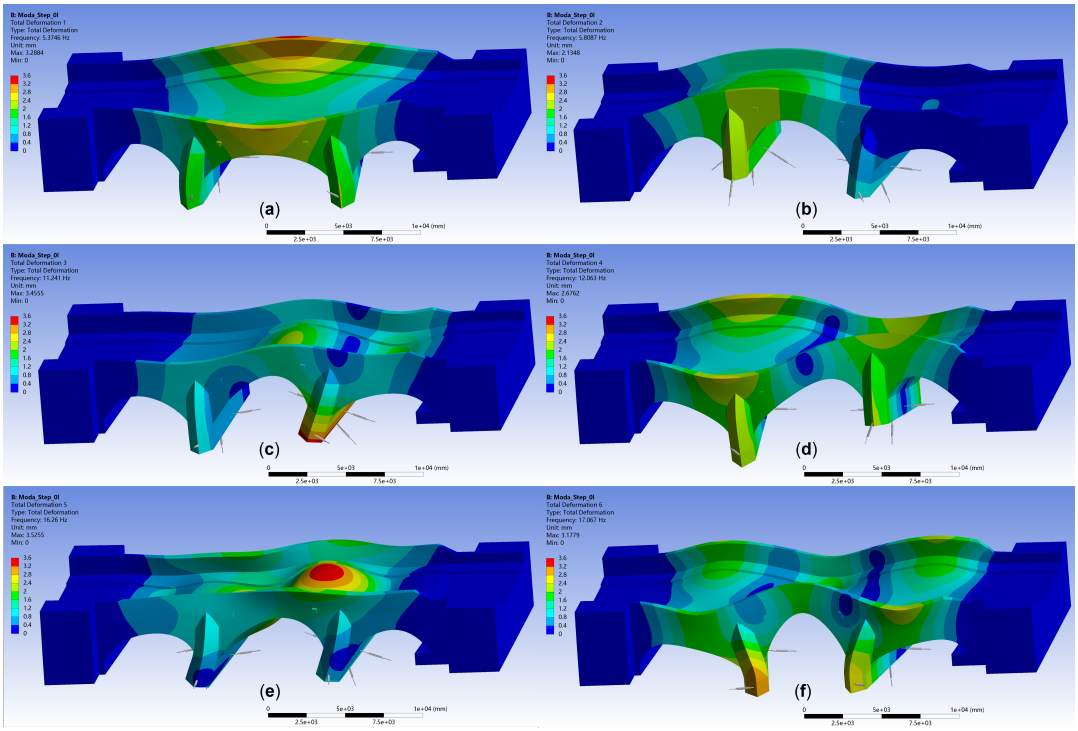

Figure 4.10: Modal shape in the Step 0 (initial state): (a) first mode; (b) second mode; (c) third mode; (d) fourth mode; (e) fifth mode; (f) sixth mode

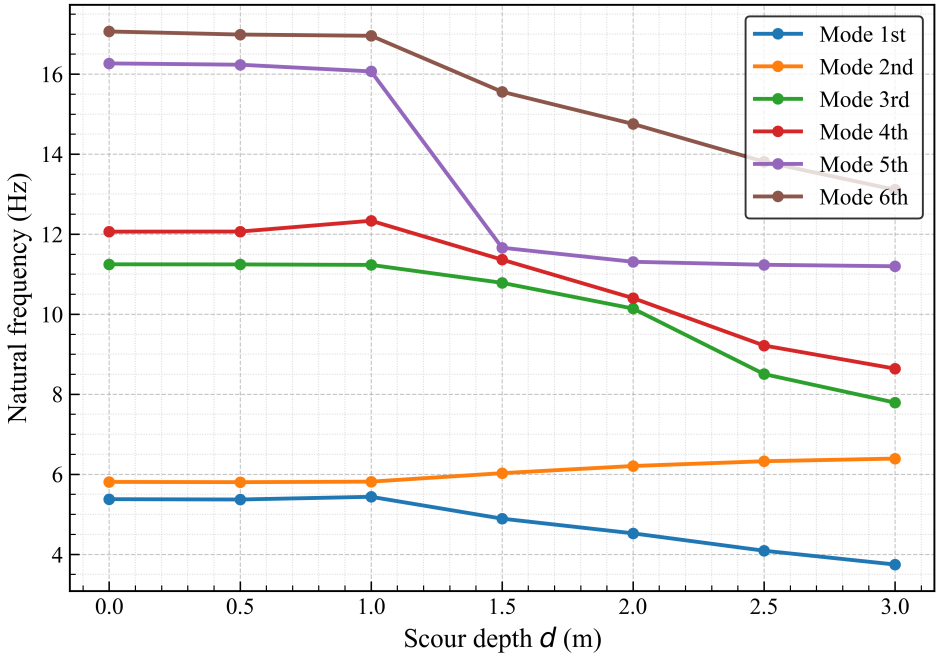

Figure 4.11: Natural frequency development as the scour progresses

When selecting modal indicators in practice, a trade-off must be considered between monitoring feasibility and the magnitude of frequency variation. Overall, the first mode remains the most suitable indicator due to its considerable variation and the lower measurement requirements com-

pared to higher modes. However, when monitoring natural frequency in real engineering, the signal is usually polluted by environmental factors such as temperature, wind and traffic load [156], those disturbances may seriously influence the successful identification of modal parameters.

4.4.4. Mode localization and transition

An interesting behavior is observed in the fifth mode as shown in Figure 4.11. The frequency is relatively stable before Step 2 and after Step 4 but drops sharply at Step 3, where it approaches the value of the fourth mode. This change in modal shape indicates a loss of localized modal characteristics, and suggests that the reduction in pier stiffness shifts the fifth mode from a localized deformation pattern to a more distributed, coupled response. Correspondingly, the modal frequency drops from approximately 16Hz to 12Hz. This process clearly reflects the stiffness degradation and can potentially serve as another indicator for scour damage.

In structural dynamics, ”mode localization” refers to the phenomenon where, due to damage or boundary condition changes, high-order modes transform from global to local participation. This transformation confines the modal response to a localized region, rather than engaging the entire structure. Higher-order frequencies (e.g., the fifth mode in this research) are more sensitive to local damage and are thus suitable for local damage detection, while lower-order frequencies (e.g., the first mode) better reflect global stiffness changes.

Specifically, when scour-induced damage occurs at the pier foundations, the structure's stiffness matrix undergoes local changes, expressed as:

$$\mathbf{K}(\tau) = \mathbf{K}_0 - \sum_{i=1}^{m} \alpha_i(\tau)\mathbf{K}_i \tag{4.11}$$

where:

- $\mathbf{K}_i$ represents the local stiffness change at the i-th support point due to scour;
- $\alpha_i(\tau) \in [0, 1]$ is the scour weight coefficient, increasing with scour depth τ.

When $\alpha_i(\tau)$ becomes sufficiently large, a sudden change in overall stiffness distribution may trigger modal reordering, referred to as ”mode transition”. The theoretical explanation of modal transition is given in Appendix C.

When significant local damage occurs, higher modes (e.g., the fifth mode) experience considerable frequency drops, which can be characterized by the mode localization factor (MLF) $F_j(\tau)$ [157]:

$$F_j(\tau) = \frac{\sum_{k=1}^{N} [\Phi_j(k,\tau)]^4}{\left(\sum_{k=1}^{N} [\Phi_j(k,\tau)]^2\right)^2} \Bigg/ \frac{\sum_{k=1}^{N} [\Phi_j(k,0)]^4}{\left(\sum_{k=1}^{N} [\Phi_j(k,0)]^2\right)^2} \tag{4.12}$$

Here, $\Phi_j(k,\tau)$ denotes the displacement of the j-th mode shape at the k-th measurement point in state τ, and N is the total number of measurement points. The numerator represents the

compactness index of the current (possibly damaged) state, while the denominator serves as a reference value in the undamaged state $\tau = 0$.

The MLF quantitatively characterizes the degree of mode localization:

- When $F_j(\tau) < 1$, the vibration energy of mode j becomes more spatially concentrated, indicating the emergence of mode localization.
- A significantly low value (e.g., $F_j(\tau) \ll 1$) suggests strong localization, often due to severe structural degradation such as cracks or stiffness detuning, or sudden change of the boundary conditions.

In masonry bridges, the structure can be conceptualized as a serial arch-beam system with dense modes in higher frequencies. When local scour, cracking, or detachment occurs, coupling stiffness between adjacent spans weakens, promoting local stiffness weakening and mode localization.

As illustrated in Figure 4.12, during scour stages, local loss of support at cutwaters leads to sharp reductions in localized stiffness, triggering distinct mode localization (e.g., $F \approx 0.485$ of the total deformation at Step 3). However, as scour progresses and global stiffness uniformly decreases, mode localization tends to diminish, and F gradually recovers toward 1.0.

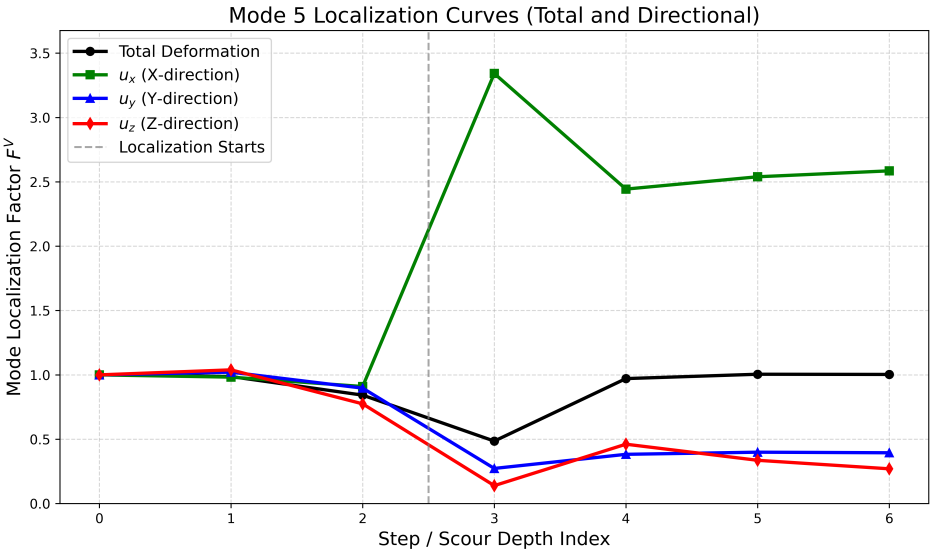

Figure 4.12: Mode localization of total and directional 5th mode

Therefore, for the multi-span masonry bridge investigated in this study, scour occurring at the piers leads to a transition in system behavior from global to localized responses. Notably, the fifth mode appears to be a highly sensitive indicator for identifying critical stages of scour development, as it has a distinct signature of mode localization. An important advantage of using this indicator is that mode localization itself is a parameterized indicator, which can be fully computed, updated, and output by the digital twin framework in an automated manner. However, this modal localization also has some drawbacks hindering it from being deployed on-site, such as the difficulty in sensing higher-order modes and the disturbance from noise, which will be discussed in the following

section.

4.5. Failure indicator-based monitoring

4.5.1. Monitoring principle

Effective predictive maintenance in a digital twin framework requires the identification of structural indicators that reliably capture scour-induced failure mechanisms. Since both local and global failures are typically triggered by abrupt changes in boundary conditions, such boundary changes inevitably lead to alterations in modal shapes, localized settlements, and other structural responses. These events can be effectively captured through structural indicators, which tend to exhibit sharp variations prior to failure [114]. Therefore, this study suggests an indicator-based monitoring approach. The concept is schematically illustrated in Figure 4.13. The advantage of this approach is the strong physical correlation between these indicators and the underlying structural mechanics. Scour tends to cause abrupt shifts in these indicators, making it possible to define critical states and safety margins (e.g., through a simple safety factor). These thresholds enable more effective predictive maintenance before local failure develops.

The point at which the indicator exhibits a sudden change can be defined as the maximum allowable scour depth, representing the critical state of local structural failure. To enable predictive maintenance, a safety margin should be set in advance of this depth, thereby defining an intervention scour depth. Once the on-site scour depth approaches this intervention level, the digital twin system should automatically issue alerts, then engineers or fully automated systems can develop appropriate scour countermeasures (the specific methods for scour protection are beyond the scope of this study).

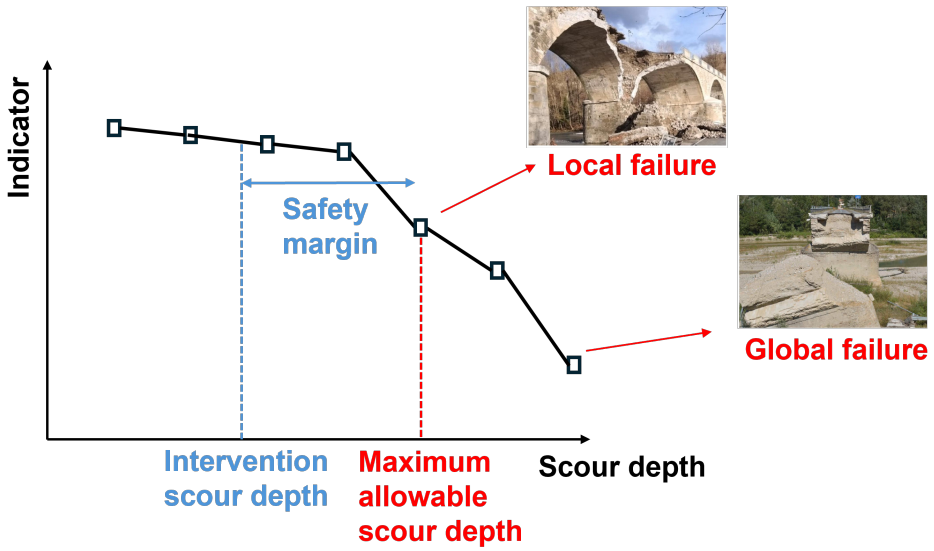

Figure 4.13: Failure indicator-based predictive maintenance (scour failure diagrams modified from [16])

Figure 4.13 also illustrates the two-tier monitoring and early warning mechanism emphasized in this study. The first tier involves updating the digital twin model either on a regular schedule

or in response to events. Finite element analysis is then performed to simulate the progressive development of scour and determine the maximum allowable scour depth. By applying a safety margin, this allows the definition of an intervention scour depth, which marks the point at which preventive actions should be taken. The second tier focuses on real-time field monitoring of a selected failure indicator. A sharp increase or decrease in the monitored indicator signals that the structure is approaching or has reached a critical failure state.

The two-tier approach has distinct advantages: the first tier enables proactive deployment of scour protection measures, while the second provides timely warnings that may require immediate responses such as traffic restrictions and emergency interventions upstream and downstream of the bridge.

4.5.2. Assessment of failure indicators in practice

From a numerical perspective, two key requirements must be satisfied to implement this two-tier monitoring and early warning strategy. First, appropriate indicators must be identified that are sensitive to local stiffness degradation and exhibit pronounced variations as failure approaches. Second, these indicators must be practically observable, ideally through real-time monitoring technologies.

According to these criteria, indicators such as maximum principal stress are not suitable for monitoring purposes. Although maximum principal stress directly reflects the stress distribution and potential failure mechanisms within the structure. However, it is difficult to measure in practice. This is because stress cannot be obtained directly and must be deduced from strain measurements using constitutive models. However, material heterogeneity and boundary condition variability make the application of constitutive models very complex because many assumptions may be violated. As a result, maximum principal stress is mainly suitable for theoretical and numerical investigations rather than practical monitoring. In contrast, pier settlement and natural frequency not only show clear responses as the structure approaches a critical state but also offer practical observability. These characteristics make them more appropriate as failure indicators within a digital twin framework. The assessment of the five failure indicators in this study is summarized in Table 4.3. In general, indicators based on displacement and rotation are sensitive to the scouring process while remaining relatively robust against environmental noise, such as vibrations, water flow, and temperature fluctuations. Moreover, commercially available monitoring systems for these indicators are well-developed, which make them the most practical and reliable options for field deployment.

In contrast, changes in dynamic characteristics tend to lag behind structural deformation and are more susceptible to external disturbances. Environmental factors can significantly affect the identification of modal parameters; for instance, temperature variations alone may introduce an uncertainty of 5% to 10% in the estimation of natural frequencies [158, 159, 160]. These problems hinder the deployment of vibration-based monitoring and early warning systems that use dynamic indications to work well.

Table 4.3: Comparison of candidate failure indicators for scour monitoring in masonry bridges

Indicator	Sensitivity to scour	Noise resistance	Monitoring feasibility
Pier settlement	High (strong signal after certain level of scour)	Very high (robust against ambient disturbance)	High (GNSS, leveling, etc.)
Pier rotation / inclination	Very high (early sign of asymmetric scour)	High (resilient to noise with filtering)	Very high (can be monitored by tiltmeters)
Maximum principal stress	High (in FE models)	N/A (not directly observable)	Low (requires stress field modeling)
Natural frequency (1st or higher)	Medium (changes only after severe scour)	Low to medium (sensitive to temperature, humidity)	Medium (usually requires stable excitation)
Mode localization	High	Medium	Very low (needs multiple accelerometers)

4.6. Maximum allowable scour depth

This section defines the maximum allowable scour depth based on several failure indicators identified through numerical simulations:

1. **Macroscopic arch damage:** At Step 3 (scour depth of 1.5 m), typical tensile cracking failure was observed on both sides of a single pier arch. This local failure of the arch ring may subsequently induce sliding of the backfill, eventually leading to local structural failure. Such failure patterns have been observed in real-world cases, as illustrated in Figure 1.2(b).
2. **Stress redistribution:** When the scour depth reaches 1.5 m, the maximum principal stress in the left and middle arch increases rapidly, and after 1.5 m, the measured areas show softening behavior which strongly indicate the structural capacity is no longer increasing, but rather decreasing due to internal cracking and load path disruption (Figure 4.5). This stress redistribution causes concentrated tension near the pier, eventually leading to cracking failure between the two adjacent arches.
3. **Rapid pier settlement:** As illustrated in Figure 4.9, pier settlement accelerates rapidly after a scour depth of 1.5 m, corresponding to a critical state when the bridge structure is near the failure.
4. **Modal response anomalies:** Changes in natural frequencies and the localization of mode shapes are also indicative of localized failure mechanisms.

The determination of the maximum allowable depth in this study is based on several factors. The most critical feature when the masonry bridge is approaching a failure state is the redistribution of the maximum principal stress. As shown in Figure 4.5, a clear stress redistribution pattern

emerges with increasing scour depth. Similar failure phenomena have also been recorded in real-world engineering cases, as illustrated in Figure 1.2. In those cases, typical local failure modes at the arch–pier interface are characterized by significant stress concentration and the formation of plastic strain zones. These features correspond closely with the simulation results, which reveal similar stress intensification in the middle arch region. The dashed line in Figure 1.2(a) and (b) shows local instability at the scoured pier, which is similar to the failure scenario observed in the numerical model. Figure 1.2(c) shows pronounced masonry spalling and collapse at the intrados of the arch due to scouring. This failure pattern aligns with the simulation result of pier settlement and the corresponding stress redistribution observed in the middle arch. Figure 1.2(d) is the complete collapse of the main arch span, that is, the final limit state of global structural instability. However, the definition of failure in this study is constrained in the loss of serviceability rather than a macroscopic collapse of the bridge structure.

Figure 4.9 shows that the pier settlement and differential settlement also have a certain degree of development, particularly after the scour depth reaches 1.5m. Other indicators, such as variations in natural frequency and mode shape localization index, also have a pronounced variation after this certain scour depth. Therefore, in summary, once the scour depth exceeds 1.5 m, considerable changes occur in many aspects, including stress distribution, settlement, and modal parameters. The maximum principal contour of Step 3 (as shown in Figure 4.6) further reveals localized tensile failure, especially in the quarter-span regions on both sides of the left pier, where the stress state has gone into the softening area.

In summary, the maximum allowable scour depth should be set at 1.5 m. This threshold provides a physically informed basis for establishing intervention scour depth levels, ensuring that early warnings can be issued well before critical failure occurs in a digital twin monitoring framework.

4.7. Sensitivity analysis of material parameters

Given that the modeling process in this study involves a wide range of material mechanical parameters, which inherently contain uncertainties, a sensitivity analysis is essential. It helps identify which parameters most strongly influence the structural response, thereby providing a strong foundation for the model calibration in the future.

This subsection analyzes how changes in two key parameters, namely *density* and *stiffness*, affect the modal behavior of the structure. The focus is on their effect on natural frequencies. Results for the first-order natural frequency are shown in Figure 4.14. Additional results for higher-order modes are provided in Appendix D.

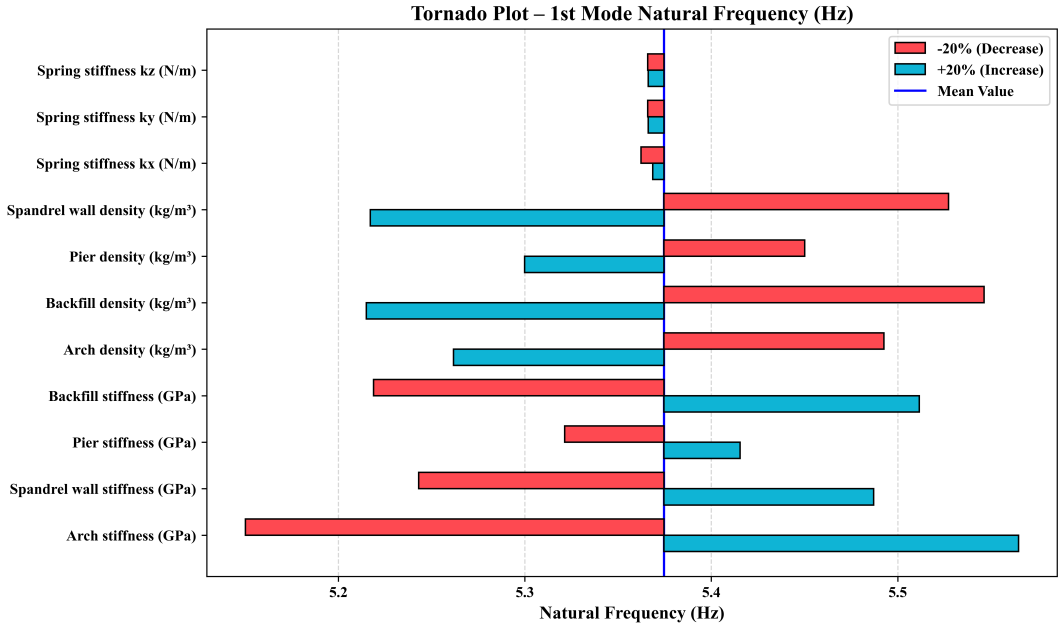

Figure 4.14: Sensitive analysis of material parameters to first mode natural frequency

As illustrated in the figure, the *arch stiffness* substantially affects the modal properties, followed by the *backfill density*, *backfill stiffness*, and the *spandrel wall density*. In contrast, the influence of other parameters, such as the *Winkler spring stiffness*, is relatively small. Moreover, it can be observed that *density* and *stiffness* show opposite trends in their impact on natural frequencies, which is consistent with the fundamental solutions of structural dynamic equations.

5 Structural health monitoring

5.1. Scour depth monitoring by FBG-based vortex flow sensor

The vortex flow sensor (VFS) is a passive flow velocity monitoring device based on the principle of vortex-induced vibration (VIV). In this study, the VFS structure consists of a bluff body, three vibration-sensitive fins, each equipped with an embedded FBG sensor near its junction with the bluff body, as illustrated in Figure 2.1.

Traditionally, vortex flow sensors measure flow velocity indirectly by detecting structural vibrations generated by periodic vortex shedding. In this study, however, we adopt an FBG-based VFS following the design proposed by Campbell et al. [62], in which the FBG directly senses the vibration signals. As shown in Figure 5.1. When water flows past the bluff body, vortices shed alternately on either side downstream, forming a Kármán vortex street. Due to the alternating shedding of vortices, the bluff body experiences periodic lateral oscillations. Each time a vortex sheds from the bluff body, it exerts an asymmetric transverse force on the structure, with the force direction perpendicular to the flow direction. This periodic transverse force is referred to as vortex-induced vibration, and the role of the FBG is to detect the strain generated in the fins by such vibrations.

Compared to classical vortex flow sensors described by Venugopal et al. [161] and Igarashi [162], which are designed for precise flow measurement, the FBG-based VFS developed by Campbell et al. [62] focuses primarily on qualitatively identifying the presence or absence of vibration to track the development of scour.

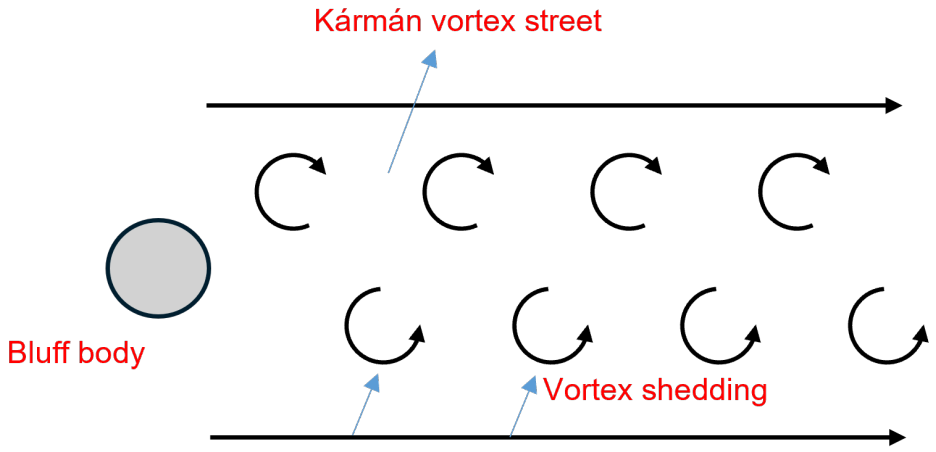

Figure 5.1: Conceptual diagram of Kármán vortex street

5.1.1. Relationship between vortex shedding and frequency

When a fluid with velocity U flows past a bluff body, alternating vortex structures are formed downstream, known as a Kármán vortex street. This vortex shedding generates periodic pressure fluctuations on both sides of the bluff body, inducing vibrations in the sensing beam structure. The

vibration frequency f can then be extracted by the sensing element. The relationship between the vortex shedding frequency and the flow velocity is expressed as follows:

$$f = \frac{St \cdot U}{D} \tag{5.1}$$

where:

- f: Vortex shedding frequency (Hz);
- St: Strouhal number, a dimensionless constant related to the geometry of the bluff body and the Reynolds number;
- U: Local flow velocity (m/s);
- D: Characteristic width of the bluff body (m).

Within a certain Reynolds number range (typically $Re \approx 10^3 \sim 10^5$), the Strouhal number can be approximately regarded as constant, resulting in a linear relationship between vortex shedding frequency and flow velocity. Conventional devices such as vortex flowmeters mainly utilize the linear relationship described in Equation 5.1 to measure the flow velocity.

5.1.2. FBG sensing principle

The pressure differences generated by vortex shedding induce periodic vibrations in the sensing beam. This vibration bends the beam, and the FBG affixed to the beam experiences periodic strain. This strain causes a shift in the reflected wavelength, which can be described by the following equation:

$$\Delta\lambda_B = \lambda_B \cdot (k_\epsilon \cdot \epsilon + k_T \cdot \Delta T) \tag{5.2}$$

where:

- $\Delta\lambda_B$: Variation of the Bragg wavelength;
- λ_B: Initial Bragg wavelength;
- ϵ: Axial strain;
- ΔT: Temperature change;
- k_ϵ, k_T: Sensitivity coefficients for strain and temperature, respectively.

Environmental temperature variations can also cause changes in the Bragg wavelength, as indicated in Equation 5.2. Since conventional measurements primarily focus on strain, it is necessary to either ensure stable environmental conditions or apply temperature compensation to attribute the wavelength variation predominantly to strain.

5.1.3. Pressure difference induced by vortex shedding

During vortex shedding, alternating pressure differences are generated on the upper and lower surfaces of the bluff body, acting on the sensing beam structure. This pressure difference can be approximately expressed as:

$$\Delta p = \frac{1}{2} \cdot \rho \cdot U^2 \cdot C_p \tag{5.3}$$

where:

- Δp: Pressure difference between the two sides (Pa);
- ρ: Fluid density (kg/m^3);
- U: Flow velocity (m/s);
- C_p: Pressure coefficient associated with the bluff body.

The greater the pressure difference, the more pronounced the bending of the sensing beam, leading to a more significant FBG wavelength shift, which is favorable for signal extraction.

5.1.4. Advantages compared to conventional FBG monitoring systems

Conventional FBG scour monitoring systems typically employ cantilever beam structures (as shown in Figure 5.2), where scour caused by flowing water gradually exposes the cantilever beam, leading to strain changes used to estimate scour depth. However, such systems face two evident challenges during flood events or when floating debris is present:

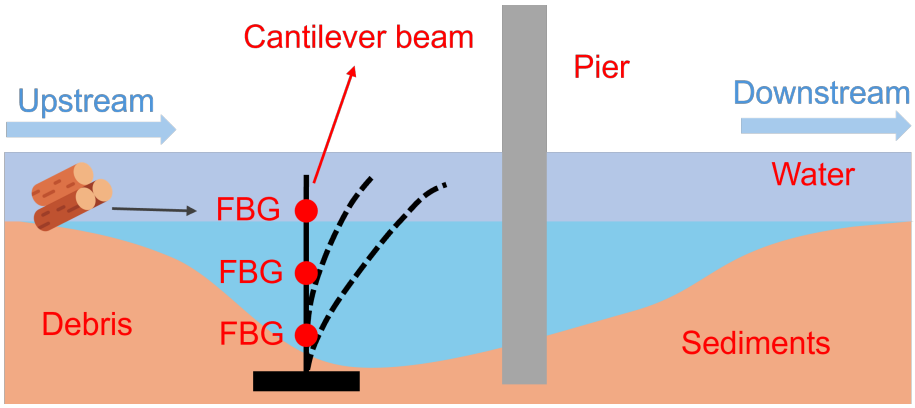

Figure 5.2: Traditional FBG layout for scour monitoring

Firstly, flood events are typically accompanied by substantial floating debris, including tree branches, stones, construction materials, and household appliances [154]. An example of debris accumulation after flooding is shown in Figure 5.3. Those debris often collide with the sensors, generating substantial impact forces that can severely damage the cantilever-type FBG structures. Since traditional FBG structures are designed to deform under load to sense strain, cantilever beams (such as the one shown in Figure 5.2) typically require a certain degree of deformation to enable

effective FBG sensing. However, this also introduces a drawback: they are particularly vulnerable to damage from sudden large impacts, especially from debris. Those impacts can easily strike structural components such as piers and arch springings, leading to structural damage or blockage of bridge openings, and can also readily destroy conventional FBG monitoring systems. Secondly, floating debris adhering to the sensor surface can alter the projected frontal area facing the flow, thus affecting the hydrodynamic forces and reducing measurement accuracy.

Figure 5.3: An example of debris accumulation after flooding [154]

In contrast, the FBG-based vortex flow sensing system in this study shows evident advantages in terms of structural design and sensing mechanisms:

- Non-reliance on deformation of the main body: The measurement is based on the deformation of fins located behind the bluff body, rather than on the deformation of the bluff body itself. As a result, the bluff body can be constructed from rigid materials (such as the stainless steel used in this study), allowing the device to effectively resist debris impact.
- Indirect measurement: Drag force is very easily influenced by environmental factors such as debris. However, in the proposed device, scour depth is detected qualitatively without disturbance from drag forces.
- High structural rigidity: The use of stainless steel structures provides strong resistance against flood and debris impacts.
- Tolerance to debris attachment: Even in the presence of debris, vortex shedding characteristics are largely stable, with only minor effects on the Reynolds number, thus exerting limited influence on signal integrity.

Overall, this FBG-based monitoring system demonstrates superior stability and measurement reliability under variable hydrological conditions and debris disturbances. These advantages make it more suitable for long-term monitoring in real-world engineering applications.

5.2. FBG-based vortex flow sensor analysis

In previous work, Campbell et al. [62] conducted laboratory flume experiments to validate the sensor design. Their results showed that, even under low flow velocity conditions, the rubber fins experienced certain strain due to the vibrations induced by the vortex shedding. Moreover, the sensor successfully captured a positive correlation between vibration intensity and flow velocity.

Based on this previous research, this study investigated the performance of the FBG-based vortex flow sensor through numerical simulation. ANSYS Fluent was employed to model the sensor under controlled fluid conditions. The aim is to validate its suitability for scour depth monitoring in the time domain.

5.2.1. Study on the formation conditions of Kármán vortex streets

The formation of a Kármán vortex street mainly depends on the fluid velocity U, the kinematic viscosity of the fluid ν, and the characteristic length of the bluff body D. The criterion is typically described using the Reynolds number (Re), defined as:

$$Re = \frac{UD}{\nu} \tag{5.4}$$

where:

- U: Mean inlet velocity (m/s);
- D: Characteristic length of the bluff body ($D = 0.02\ \mathrm{m}$ in this case);
- ν: Kinematic viscosity, approximately $\nu \approx 1.0 \times 10^{-6}\ \mathrm{m^2/s}$ for water at room temperature.

For a cylindrical bluff body, a Kármán vortex street forms when $Re > 40$ [163]. For rectangular bluff bodies with sharp edges, such as the one in this study, the required Reynolds number for vortex street formation is slightly lower [164]. This is because sharp corners promote earlier flow separation, which facilitates the formation of vortex streets. When the Reynolds number further increases to approximately 10^3, the vortex street becomes more complex but still exhibits stable periodic shedding.

In this study, the inlet velocity is set to $U = 1.0\,\mathrm{m/s}$, and the characteristic length of the bluff body is 20 cm. Substituting into the equation yields: Re = 20,000. This result indicates that the Reynolds number far exceeds the critical value for vortex street formation, and thus typical Kármán vortex street structures are expected to form behind the sensor under the simulated conditions.

5.2.2. Fluid–solid coupled domain and field setup

The fluid domain setup is illustrated in Figure 5.4. The upstream section (where the sensor is located) is set to a length of 450 mm to ensure sufficient development of the inlet velocity profile. The downstream wake region is considerably longer, at 1500 mm, to allow for the full development of the Kármán vortex street. The height of the fluid domain is set to 350 mm.

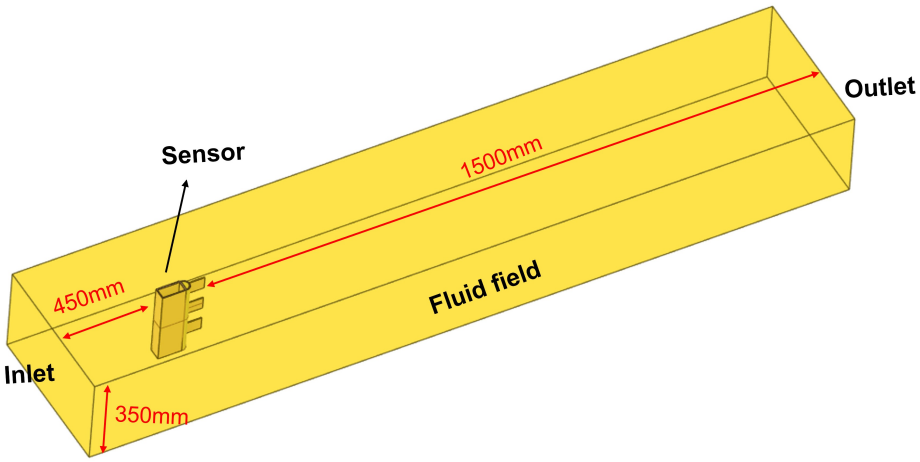

Figure 5.4: Fluid domain size and sensor relative position

5.2.3. Fluid field model setup

An unstructured mesh with a grid size of 8 mm and tetrahedral (Tet4) elements is used for meshing. The total number of nodes is 510,970, and the number of elements is 2,738,758. The mesh quality check shows that most elements have a quality greater than 0.5. This value means an overall acceptable mesh quality.

The fluid material is set to default water properties, with $\rho = 998.2\ \mathrm{kg/m^3}$ and $\mu = 0.001003\ \mathrm{Pa \cdot s}$. A flow velocity is set as 1 m/s, reflecting typical river scour flow conditions. The outlet is set as a pressure outlet, and no-slip wall boundary conditions with a relative roughness of 0.5 are applied. Other parameters follow default settings, as summarized in Table 5.1.

The flow is modeled as transient and incompressible. The turbulence model adopted is the shear stress transport (SST) k–ω model, which combines the high accuracy of the k–ω model near walls with the robustness of the k–ε model in free flow regions [165]. The corresponding control equations of the SST model can be seen in [166].

The simulation uses 8000 time steps, with a time step size of 0.005 s and a maximum of 20 iterations per step, using residual convergence criteria to ensure numerical stability.

Table 5.1: Summary of boundary condition settings

Region	Boundary type	Setting parameters	Remarks
inlet	velocity-inlet	Velocity: 1 m/s Turbulence intensity: 5% Turbulent viscosity ratio: 10	Flow along the x-axis
outlet	pressure-outlet	Back pressure: 0 Pa (relative)	Free outflow
wall-sensor	wall	No-slip condition Standard wall functions Relative roughness: 0.5	Monitoring wall for calculations
wall-domain	wall	Default no-slip condition Relative roughness: 0.5	Domain boundary
interior-fluid	interior	–	Internal flow region

5.2.4. Solid field model setup

A simplified structural model is employed to simulate the response of the sensor device under scour conditions. The device consists of a stainless steel main body and three rubber fins: the top fin, middle fin, and bottom fin. The assumed scour progression is illustrated in Figure 5.5. Initially, the top fin is fully exposed to the fluid domain, while the scour depth has just reached the upper edge of the middle fin, this condition is defined as Step 0. Step 1 corresponds to the scour reaching the mid-height of the middle fin, at which point the sensor FBG 2 is at the critical threshold of exposure. Subsequently, Step 3 represents the condition where scour has reached the lower end of the middle fin. This process continues through Steps 4 and 5, until Step 7, in which all three fins are fully exposed. The aim of this solid-field modeling approach is to demonstrate the potential of the sensor for scour monitoring by simulating this progressive exposure scenario. During this scouring process, the function of soil to the sensor structure is simplified as fixing support.

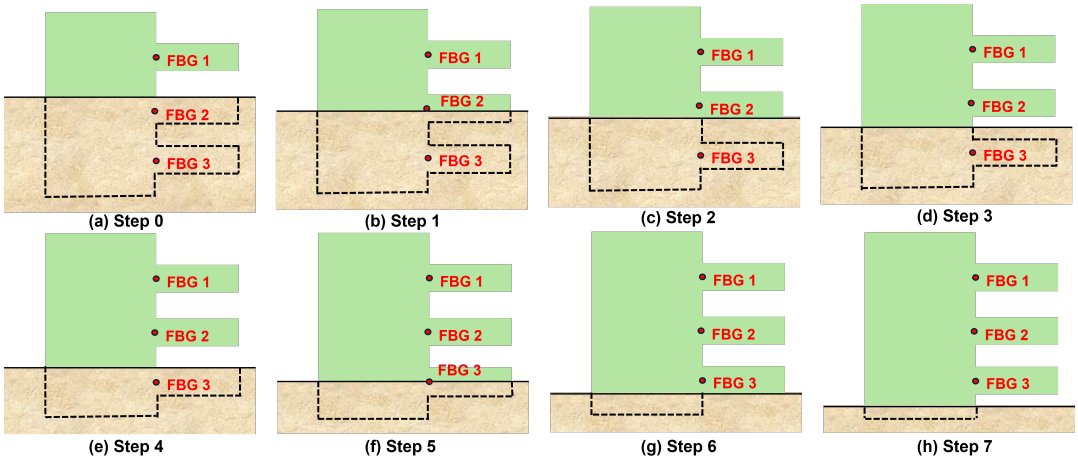

Figure 5.5: The process of gradual exposure of the FBG-based vortex flow sensor. Where (a) to (h) respectively correspond to Step 0 to Step 7 (8 steps in total)

Two material models are defined to reflect the mechanical properties of different parts of the sensor: rubber for the fins and stainless steel for the bluff body (as shown in Figure 2.1). The flexible fins are modeled using the Mooney–Rivlin two-parameter hyperelastic material model, which is usually suitable for moderate strain levels (not exceeding 200%) [167]. The Mooney–Rivlin strain energy function is given by [168] as shown in Equation 5.5.The material constants are adopted from literature, with $C_{10} = 1.5590\ \mathrm{MPa}$, $C_{01} = 0.3118\ \mathrm{MPa}$ [169].

$$W = C_{10}(I_1 - 3) + C_{01}(I_2 - 3) \tag{5.5}$$

where C_{10} and C_{01} are material constants, and I_1, I_2 are the first and second invariants of the deformation tensor. To ensure material monotonicity and numerical stability, the following conditions must be satisfied:

$$C_{10} + C_{01} > 0, \quad C_{01} > 0$$

The parameters used in this study meet these criteria.

The main support structure (the stainless steel) is modeled as linear elastic structural steel with a Young's modulus of $2.1 \times 10^{11}\ \mathrm{Pa}$, a Poisson's ratio of 0.3, and a density of $7850\ \mathrm{kg/m^3}$.

5.2.5. Fluid field simulation results

Figure 5.6 shows the converged velocity field. Behind the sensor, a symmetric wake develops, characterized by a central low-speed region and alternating high-speed streaks on both sides. A clear velocity difference appears between the inner and outer surfaces of the fins, implying a stagnation zone on the inner side. This creates a pressure gradient (Equation 5.3) that drives the fins to bend.

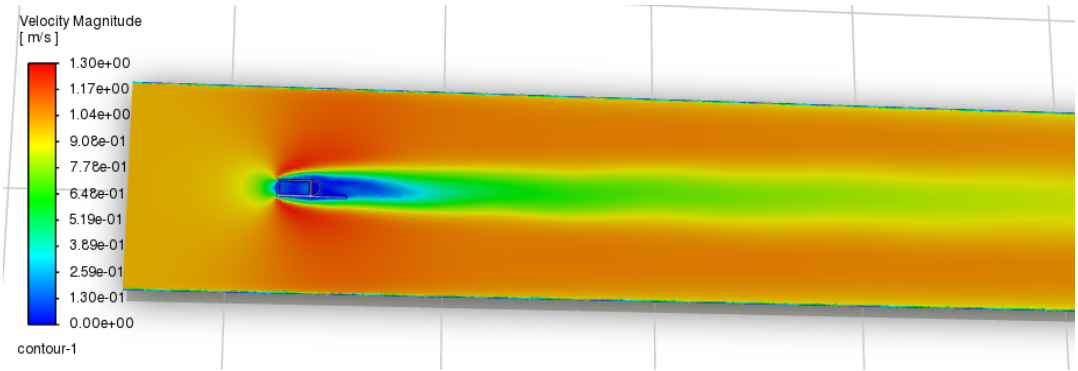

Figure 5.6: Section view of the upper fin

5.2.6. Solid field simulation results

This section presents the structural response simulation under vortex-induced flow scour, focusing on the equivalent strain distribution in key areas to verify the feasibility of using FBG sensors for scour monitoring.

Figure 5.7 illustrates the maximum elastic strain of the three FBG sensors at different scour depth.

FBG 1 is mounted on the top fin and fully exposed to the flow domain from Step 0. It consistently records a strain of approximately 3.24×10^{-3} m/m. In contrast, FBG 2 is located on the middle fin, showing negligible strain at Step 0. At Step 1, when the sensor just starts to emerge above the sediment surface, a notable increase in strain is observed. By Step 2, where the middle fin is fully exposed, the strain in FBG 2 rapidly rises and then stabilizes around 1.44×10^{-3} m/m in subsequent steps, indicating its suitability for early-stage scour detection. For the bottom fin, FBG 3 does not show an evident response until after Step 6. At Step 7, its strain sharply increases, reaching 2.61×10^{-1},m/m, suggesting that the scour depth has reached the same level as FBG 3.

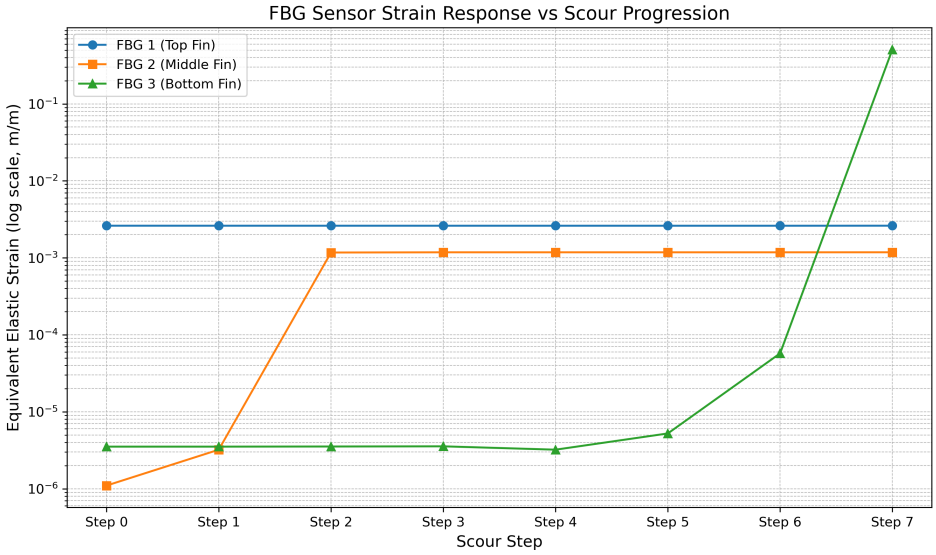

Figure 5.7: The responses of FBG-based vortex flow sensor with the development of scour depth

Collectively, the three-tier sensor layout successfully captures the entire scour progression, providing effective responses from early detection to late-stage warning. This confirms the device's potential for full-process scour monitoring. In real-world applications, the development of scour depth from Step 0 to Step 7 represents a time-dependent process, during which the current scour state can be qualitatively assessed by observing sudden changes, gradual increases, and then stabilization of strain readings from different sensors. Moreover, it should be noted that in on-site monitoring, the signal may not act exactly the same as in Figure 5.7, since the FBG sensors are also influenced by the environmental noise and measurement error. However, the general trend is similar, and engineers can easily use the response of FBG to judge the scour depth level.

6 Connection layer of digital twin

The previous two chapters introduced two main components of the digital twin system, specifically the FEM module in the virtual twin and the SHM module in the physical entity. The FEM module simulates 'what-if' scenarios to assess the structural response during scouring, while the SHM module provides real-time data from the physical system. This chapter presents the third key component, the connection layer.

In a digital twin framework, the connection layer links the physical system with its virtual counterpart via two primary mechanisms: forward and backward connections. Forward connections update the digital twin model to ensure that the virtual twin reflects the real-world conditions. In contrast, backward connections utilize the results from the digital twin to inform the dicision making in real world. In this study, the forward connection is implemented mainly through the Scan-to-FEM geometry updates, as detailed in Chapter 4. Accordingly, the current chapter focuses on explaining the backward connection and its role within the overall digital twin system.

A key feature that distinguishes digital twins from conventional digital modeling tools such as building information modeling (BIM) and geographic information systems (GIS) is the backward connection [170]. Conventional digital models mainly provide semantic representations of physical assets through visualization and documentation. They do not actively support decision-making or system control. In contrast, the backward connection enables digital twins to derive actionable insights from simulations or data analysis and apply them to guide operations in the physical world. Together with the forward connection, which focuses on model updating and synchronization, these two connections complete the closed-loop architecture of the digital twin.

In this thesis, two commonly used modules are adopted as examples of backward connections for real-world decision-making: (1) sensor placement optimization based on the finite element model, and (2) a predictive maintenance workflow that combines the maximum allowable scour depth and corresponding failure indicators derived from finite element analysis with real-world monitoring data.

6.1. Sensor placement optimization

The identification of structural dynamic system parameters is critical for effective model updating and structural health monitoring. The ability to extract meaningful information from data heavily depends on both the number and spatial distribution of sensors. However, accurate identification of modal information often requires a large number of sensors [171]. This section presents an approach to optimize sensor placement using the first mode shape data under multiple scour depths (Step 0 to Step 6), based on the Fisher information matrix (FIM).

The underlying concept is to treat the total deformation under different scour conditions as a set of "modal shapes" and then perform greedy sensor selection by maximizing the determinant of the corresponding Fisher matrix. Specifically, the modal deformation results from the seven structural

states (Step 0 to Step 6) are concatenated column-wise to form a data matrix. The objective is to ensure that the selected sensor locations can maximally distinguish the deformation patterns associated with different scour depths, thus capturing the structural response sensitivity to scour progression.

At the same time, noted that excessive sensor concentration can lead to information redundancy. This study adopted two strategies to mitigate this issue. First, information redundancy term is introduced [172], modifying the sensor placement objective function to simultaneously maximize the determinant of the Fisher matrix and minimize the information redundancy. Second, a spatial dispersion penalty term is incorporated to encourage a moderately dispersed spatial distribution of sensors.

The spatial dispersion term is introduced to address scenarios where the redundancy metric alone may not prevent excessive clustering of sensors. For example, high-frequency localized modes can still lead to dense groupings, even when redundancy thresholds are applied. Furthermore, spatial dispersion helps reduce the risk of interference effects caused by closely spaced sensors, such as cross-talk in radio-frequency (RF) systems, electromagnetic coupling in electrical sensors, or spectral overlapping in fiber optic sensors, depending on the sensing technology in use.

In this chapter, the identification of first-order natural frequency is set as an example. And it is similar for identifying other modal parameters. The detailed procedure is as follows:

6.1.1. Construction of augmented mode shape matrix

For each step s ($s = 0, 1, \ldots, 6$) of scour depth level, let the first-order mode shape be expressed as

$$\boldsymbol{\phi}^{(s)} = \begin{bmatrix} \phi_1^{(s)} \\ \phi_2^{(s)} \\ \vdots \\ \phi_N^{(s)} \end{bmatrix} \in \mathbb{R}^N, \tag{6.1}$$

where N is the total number of extracted surface nodes, and $\phi_i^{(s)}$ denotes the mode amplitude of node i at step s. By stacking the mode shapes from all steps column-wise, an augmented mode shape matrix is constructed:

$$\boldsymbol{\Phi}_{\text{aug}} = \begin{bmatrix} \boldsymbol{\phi}^{(0)} & \boldsymbol{\phi}^{(1)} & \cdots & \boldsymbol{\phi}^{(6)} \end{bmatrix} \in \mathbb{R}^{N \times 7}. \tag{6.2}$$

6.1.2. Combined response index

To quantify the total modal response of each node across multiple scour levels, a combined response index is defined as

$$R_i = \sum_{s=0}^{6} \left| \phi_i^{(s)} \right|, \tag{6.3}$$

Nodes are ranked in descending order according to R_i, and the top N_{cand} nodes are selected as candidates.

6.1.3. Fisher information matrix and objective function

Let the selected sensor node set be $\mathcal{S} \subset \{1, 2, \ldots, N_{\text{cand}}\}$ with $|\mathcal{S}| = K$. where N_{cand} denotes the total number of candidate sensor locations, and K is the number of sensors to be deployed which is determined by engineers. Then the matrix

$$\mathbf{X} = \mathbf{\Phi}_{\text{aug}}(\mathcal{S}, :) \in \mathbb{R}^{K \times 7} \tag{6.4}$$

is constructed by extracting rows of $\mathbf{\Phi}_{\text{aug}}$ indexed by $\mathcal{S}$. The proxy Q for the Fisher information matrix is given b:

$$\mathbf{Q} = \mathbf{X}\,\mathbf{X}^{\mathsf{T}} \in \mathbb{R}^{K \times K}. \tag{6.5}$$

One of the optimization objectives is to maximize the determinant of Q:

$$\max_{\mathcal{S}} \det(\mathbf{Q}). \tag{6.6}$$

Define the basic information matrix per node k:

$$\mathbf{I}_i = \mathbf{X}_i^{\mathsf{T}} \mathbf{X}_i. \tag{6.7}$$

The redundancy between nodes k and l is [172]:

$$R_{ij} = \frac{\|\mathbf{I}_i - \mathbf{I}_j\|}{\|\mathbf{I}_i + \mathbf{I}_j\|}, \tag{6.8}$$

6.1.4. Greedy sensor placement algorithm

A greedy search algorithm is employed to identify an optimal set of K sensor locations from the candidate node pool. The selection process begins with the node that has the largest combined response index R_i. In each iteration, the algorithm adds the node that maximizes a weighted score that balances spatial independence with information gain. This process repeats until the desired number of sensors is selected. The complete algorithmic steps and mathematical formulation are provided in Appendix B.

6.1.5. Optimization result

In this example, $K = 10$ sensors were selected with a dispersion term weight of $\alpha = 0.1$ and a redundancy term weight of $\beta = 0.2$. The redundancy threshold is set to 0.5. The sensor placement corresponds to the node number shown in FEM software. Thus the resulting optimal sensor indices are:

`[413880, 420923, 413858, 413842, 421415, 408748, 421039, 422526, 420266, 421044],`

and their locations are illustrated in Figure 6.1. It can be observed from the figure that the sensor placements are predominantly concentrated near the upstream cutwater side of the arch and the spandrel wall. This observation aligns with conventional intuition, as scour typically initiates on the upstream side, where modal changes are expected to be the most pronounced.

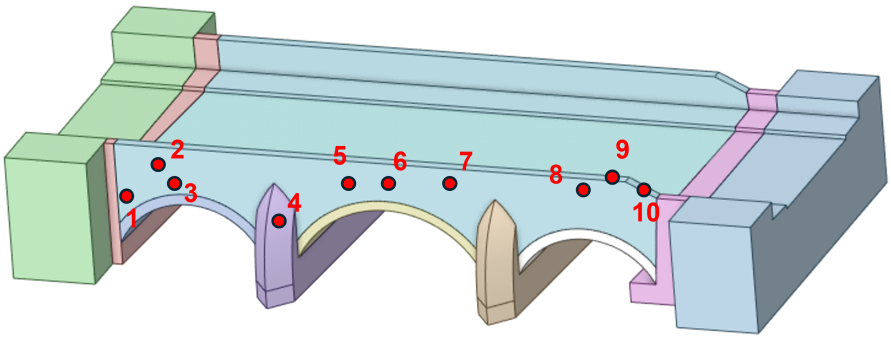

Figure 6.1: Sensor placement for tracing the first order modal shape

This method effectively constructs an augmented mode matrix using multi-step deformation data, and determines optimal sensor placements via determinant maximization of the Fisher information matrix. This process ensures that the selected sensors capture meaningful first-order modal responses under varying scour depths. Thus when scour occurs, this optimized sensing system can provide damage information in a most effective manner.

An important consideration in sensor placement is the selection of an appropriate optimization algorithm. For small-scale sensor networks, greedy algorithms is effective enough to sequentially select optimal sensor locations. However, for large-scale or dense sensor layouts, heuristic optimization techniques such as genetic algorithms or particle swarm optimization are more recommended to handle the increased complexity while still meeting the necessary physical constraints, such as the sensor spacing.

6.1.6. Noise disturbance during modal shape identification

When applying accelerometers on-site to identify modal shape information, one key challenge is the influence of noise. Under scour monitoring scenarios, the measurement output equation of an SHM system is given by:

$$\mathbf{y}(t) = \mathbf{C}_{\text{obs}}\mathbf{z}(t) + \mathbf{v}(t) \tag{6.9}$$

where:

- $\mathbf{y}(t)$: vector of measured structural responses (e.g., accelerations);
- $\mathbf{C}_{\text{obs}}$: observation matrix depending on sensor layout;
- $\mathbf{v}(t) \sim \mathcal{N}(\mathbf{0}, \mathbf{R})$: measurement noise, usually assumed to be zero-mean Gaussian with covariance $\mathbf{R}$.

Noise and environmental disturbances introduce uncertainty into the modal parameter identification process. These uncertainties can be quantitatively evaluated using the modal assurance criterion (MAC) and modal phase collinearity (MPC) [173]. Moreover, modal frequency is highly sensitive to environmental and operational conditions (EOCs), such as temperature, humidity,

wind, and traffic loads. For example, temperature-induced frequency variations may exceed 10% for bridges [156].

Within the proposed digital twin framework, sensor placement optimization is employed to enhance the observability of those modal responses that are sensitive to scour. Nonetheless, the current optimization algorithm is developed under ideal (noise-free) assumptions, and actual structural response estimations using limited sensor data may still be affected by real-world measurement uncertainties.

To mitigate the effects of noise and EOCs, various signal processing techniques have been proposed. Wavelet transforms [174] and blind signal separation (BSS) methods [175] are particularly effective in extracting modal features from noisy datasets. However, detailed implementation of these techniques is beyond the scope of this study.

6.1.7. Sensitivity analysis of sensor placement optimization

The initially optimized sensor locations on the masonry arch bridge are shown in Figure 6.1 (marked in red). The optimization objective is to capture variations in the first-order modal shapes under different scour depths with the highest information density, given a limited number of sensors. However, this optimized layout is relatively sensitive to changes in structural parameters. For example, if the stiffness of the arch or piers decreases (e.g., by 20%), the first-order bending mode shape changes accordingly, and the algorithm naturally recommends a different sensor configuration to track the new shape. To understand to what extent the sensor placement is sensitive to changes in material parameters, it is necessary to conduct a sensitivity analysis.

Referring to the previous sensitivity analysis of material parameters on the first natural frequency, as shown in Figure 4.14, the stiffness of the arch exhibits significantly higher sensitivity than other parameters. In this subsection, a 20% reduction in arch stiffness is introduced to simulate scenarios such as material aging, parameter uncertainty, or structural damage, all of which result in stiffness degradation. The updated sensor layout optimized using the FIM and greedy algorithm after the disturbance is shown in Figure 6.2.

Compared with Figure 6.1, sensors numbered 1, 4, 5, 6, and 9 (marked in yellow) demonstrate high robustness. Other sensors have slight position shifts. This is because the arch's dynamic behavior changes following stiffness reduction (e.g., modal shapes may localize or shift in frequency), and previously optimal sensor points lose their advantage. The new optimal set tends to favor locations that are likely to capture the altered mode shapes, such as moving sensors closer to the piers or toward different nodal lines of the mode shapes.

The sensitivity analysis result indicates that sensor locations associated with capturing higher-order or more spatially distributed modes are more susceptible to changes in stiffness assumptions, whereas sensors placed near supports or low-mode nodal lines (which are less sensitive to uniform stiffness changes) remain effective.

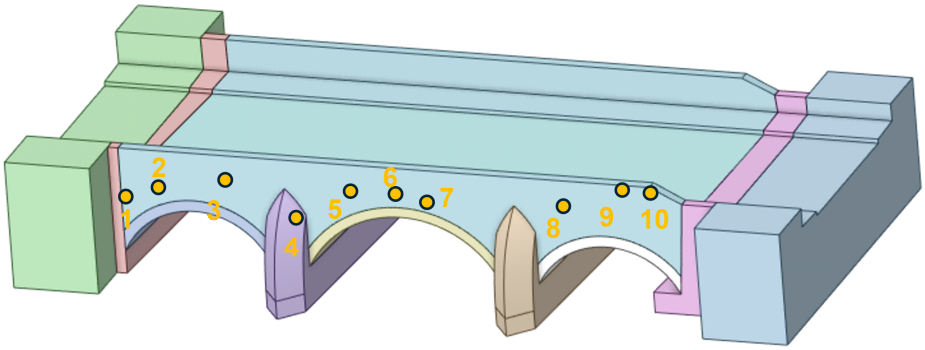

Figure 6.2: Sensor placement after reduction of the arch stiffness by 20%

Another important issue is the practical deployment strategy of sensors in the field. Within a digital twin framework, material parameters are updated either periodically or in response to events. As a result, the numerical simulation model also evolves. Changes in material properties (such as the 20% reduction in arch stiffness in this case) may lead to updates in the optimal sensor placement strategy. This update could lead to different sensor locations over time.

However, relocating sensors on a real bridge can be difficult. For example, sensors embedded within structural components cannot be repositioned. In addition, relocating sensors may cause the loss of historical data. Measurements from new locations cannot be directly compared with previous baseline data from different positions. The limitations in relocating underscore the need to introduce uncertainties into the sensor optimization in the future, which may improve the robustness of sensor placement under the uncertain material parameters.

6.2. Digital twin-inspired monitoring strategy

6.2.1. Execution of the monitoring strategy

The refined monitoring strategy proposed in this study integrates real-time sensor data with finite element analysis within a digital twin framework. Data fusion is a major challendge for scour protection [176]. However, this framework integrates data from the FBG-based vortex flow sensor, the hydrological data of the observation station, and insights from FE analysis, serving a common purpose, that is, to inform the predictive maintenance. The execution of the maintenance strategy is as follows:

1. Physical layer monitoring:
   FBG-based vortex flow sensors are deployed onsite to obtain real-time scour depth data; The hydrological data such as water level and flow velocity are measured and collected as the trigger for digital twin updating.
2. Virtual layer analysis:
   A finite element model is used to determine the *maximum allowable scour depth* based on the structural capacity.

3. Indicator-based monitoring:
   Two structural response indicators are used in the digital twin to assess scour risks:
   - Pier settlement
   - Pier rotation
4. Updating trigger
   To manage computational cost while maintaining accuracy, three update modes are proposed:
   - *Routine update:* Regular model updates at a base interval.
   - *Hydrology-driven accelerated update:* Triggered when real-time hydrological data exceed threshold values.
   - *Structure-driven update:* Triggered when any structural indicator approaches a critical limit.

This maintenance strategy is also illustrated in Figure 6.3. Note that the safety factor which quantifies the safety margin between on-site scour depth and maximum allowable scour depth is chosen to be 0.8. This factor can be adjusted based on the importance of the bridges.

6.2.2. Updating triggers of the digital twin framework

A common perception regarding digital twins (DTs) is that they must always be synchronized and updated in real time. However, this requirement often entails high computational costs and is, in many cases, unnecessary. In practice, the update frequency of a DT is typically user- or event-dependent, and depending on the engineering context, it can range from real-time synchronization to updates conducted once every few years [43]. In the DT framework proposed in this study, three update strategies are adopted:

1) Routine update mode During the normal operation phase, when the structural condition is stable and no significant hydrological anomalies are observed, the model operates under a fixed low-frequency update mechanism, with the update period denoted as T_{base}, for instance, once per month or every two weeks. The specific interval T_{base} is made according to the local norms.

2) Hydrology-driven accelerated update When the flow velocity or other external hydrodynamic indicators exceed a specified threshold, the system switches to a ”flood-sensitive mode” that reduces the update interval to T_{hydro}:

$$T_{\text{update}} = T_{\text{hydro}} < T_{\text{base}}, \quad \text{if } v(t) \geq v_{\text{th}}$$

This mode can be triggered based on real-time hydrological data, such as flow velocity and water level. Flow velocity is used here as an example; the threshold velocity v_{th} can be determined using two approaches. The first approach relies on long-term hydrological observations and historical flood event records. In this context, hydraulic models can be employed to back-calculate the minimum discharge or velocity required to reproduce observed flood extents, which allows the

estimation of threshold values associated with specific return periods such as 10-year or 50-year flood events [177]. In addition, v_{th} can also be estimated using data-driven methods, such as machine learning models trained on large-scale datasets containing flow velocity and corresponding flood occurrences [178, 179, 180].

3) Structure-driven accelerated update If a structural failure indicator shows a sudden change (increase or decrease), the system enters a "risk-enhanced mode," where the model undergoes high-frequency calibration, and the update period is set to T_{struct}:

$$T_{\text{update}} = T_{\text{struct}} < T_{\text{base}}, \quad \text{if} \quad \frac{dI_f(t)}{dt} \geq I_{\text{th}}$$

Here I_{th} is the threshold for the indicator's rate of change. I_{th} is determined based on FE simulation. For example, in the context of this study, the variation of pier settlement is approximately 25% when the bridge is approaching failure, thus the I_{th} can be determined as 10% to 15% to cover this variation. $I_f(t)$ denotes the failure indicator variable, which is monitored on site and includes:

- Pier settlement: $s_p(t)$;
- Pier rotation: $r_p(t)$;

These indicators can be measured through optical fiber sensors, accelerometers, and other sensing devices. Based on these indicators, when the system enters a risky mode, the digital twin model must be updated at a higher frequency to capture the evolving trends of structural responses and to support early warning and maintenance decision-making.

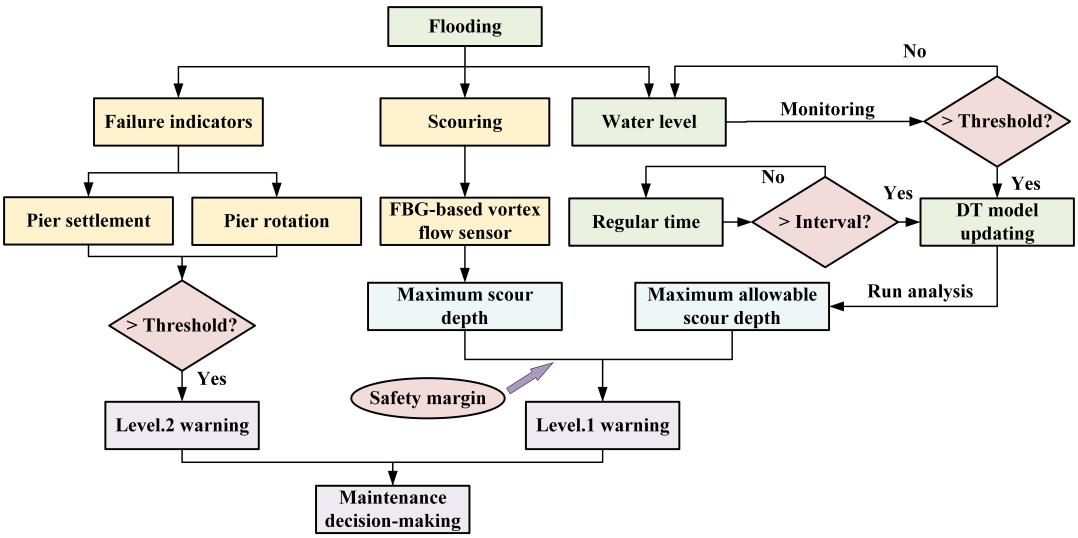

Figure 6.3: Maintenance strategy and the two-level scour warning strategy within the digital twin framework

6.3. Safety warning of the digital twin

To improve the accuracy and robustness of scour risk management, a two-level early warning strategy is implemented within the proposed digital twin framework (Figure 6.3), combining scour

depth and failure indicators as the two main methods for safety warning.

6.3.1. Level 1 warning: simulation-based threshold

A Level 1 warning is triggered when the maximum observed scour depth y_s, obtained from field monitoring (FBG-based vortex flow sensors in this case study), exceeds the safety threshold. This threshold is defined as a fraction of the critical scour depth y_{crit} derived from the digital twin simulation:

$$y_s \geq \lambda \cdot y_{\text{crit}} \tag{6.10}$$

where $\lambda \in (0.8, 0.9)$ is a safety factor set to intervene in advance. The critical scour depth y_{crit} corresponds to the limit state at which localized structural failure initiates. In this study, critical scour depth also refers to the maximum allowable scour depth.

6.3.2. Level 2 warning: structural indicator-based warning

The Level 2 warning is based on structural indicators that quantify the degradation of mechanical behavior under scour conditions. These include excessive displacement and rotation at the pier. As shown in the simulation, when scour depth increases, structural stiffness degrades and deformation localizes at the arch–pier interface. During this process, several structural indicators, such as maximum principal stress, pier settlement, pier rotation, and natural frequency, have evident responses. However, as discussed earlier, pier settlement and rotation are finally adopted as the primary indicators for on-site monitoring purpose due to their monitoring feasibility.

$$\text{Level 2 warning is triggered if} \quad \begin{cases} \dfrac{ds_p(t)}{dt} \geq r_s^{\text{th}} \\ \text{or} \\ \dfrac{dr_p(t)}{dt} \geq r_r^{\text{th}} \end{cases} \tag{6.11}$$

where:

- $s_p(t)$ is the pier settlement over time,
- r_s^{th} is the allowable settlement rate threshold,
- $r_p(t)$ is the pier rotation over time,
- r_r^{th} is the allowable rotation rate threshold.

These two structural indicators are updated through the digital twin. Once the monitored values change dramatically and the change rates exceed the defined limits, a Level 2 warning is issued, indicating urgent intervention is needed. Those rate thresholds are defined based on simulation.

6.3.3. Complementary role of the two warning levels

The two warning levels warning strategies are combined in the digital twin system. The Level 1 warning offers an early indication based on the physical progression of scour, while Level 2

focuses on the structural consequences of that progression. It should also be emphasized that Level 1 enables early warning, as scour depth evolution in the time domain can be monitored on-site. By applying an appropriate safety margin, timely alerts can be achieved before reaching critical conditions. In contrast, the failure indicators used in Level 2 often show minimal changes at early stages but show fast variation near the point of structural failure. Therefore, Level 2 is more suitable for identifying critical failure states.

The two levels of early warning can work as complementary mechanisms in practical applications. In the early stages of scour, field monitoring of scour depth, combined with finite element model updates in the digital twin environment, allows for the estimation of the critical scour depth at that time. By comparing the monitored scour depth with the simulated threshold, the appropriate timing for early maintenance intervention can be identified. In contrast, failure indicators at this stage are less effective, showing minimal variations. In the later stages of scour, when the structure approaches critical failure, real-time updates of the maximum allowable scour depth in the digital twin model may be constrained by computational limitations. In such cases, direct monitoring of failure indicators such as pier settlement provides clear evidence of the structural state. This monitoring of failure indicators at the late stage of scour informs engineers of emergency interventions such as traffic control.

7 Discussion

7.1. Contribution to the state of the art

In previous studies, finite element analysis and field monitoring were often treated as separate tasks. Although FE models can simulate the mechanical behavior of bridges under different scenarios, they usually cannot be updated once built. In particular, they cannot adjust their geometry or material parameters based on new information. Hence, this static modeling approach is not suitable for masonry bridges, which often show clear signs of aging after long service periods.

Field monitoring alone is also limited. Engineers can use SHM systems to obtain local measurements, such as strain or foundation settlement. However, these measurements do not directly indicate whether the structure remains in a healthy state or whether maintenance is required under current scour conditions.

This thesis presents an integrated digital twin framework for scour monitoring and predictive maintenance of masonry arch bridges. Unlike previous methods that separate structural modeling from sensor-based monitoring, this framework allows two-way interaction between FE simulations and field sensor data. It connects changes in scour conditions with the structural response through failure indicators that are calibrated by simulations.

A two-level early warning strategy is developed. This strategy combines a physical threshold, such as the maximum allowable scour depth, with structural indicators like pier settlement and rotation. It overcomes key limitations in existing SHM systems. These include the use of empirical thresholds and the lack of dynamic model updating. Empirical thresholds are often limited to specific locations and bridge types, which makes them hard to generalize. In contrast, the threshold values in this study are derived from finite element analysis. This makes the method applicable to a wide range of bridges in different locations. As a result, the proposed framework is scalable and transferable.

7.2. Methodological improvements and practical meanings

This section discusses the innovations introduced by the proposed scour monitoring framework. Moreover, the framework's advantages over traditional scour health monitoring and maintenance strategies are also highlighted.

7.2.1. Bidirectional loop of digital twin

The study establishes a forward model-updating mechanism that links real-world measurements with high-fidelity simulations, ensuring that the digital representation reflects the evolving condition of the physical bridge. In terms of update frequency, a hybrid strategy is adopted. With the support of external data sources, the model combines regular updates with event-based updates. This approach reduces the computational cost of the digital twin and improves its practicality.

Forward model updating is particularly relevant for scour monitoring in masonry bridges. First, most masonry bridges are in the later stages of their service life. They are prone to local damage or deformation, which requires timely updates of the finite element model to capture structural changes. Second, scour can progress rapidly under specific hydraulic conditions, such as flooding. In such cases, the reduction in foundation stiffness can quickly push the superstructure toward instability and failure. Hence, it is essential to update the model as soon as possible to ensure the FE model reflects the latest mechanical conditions.

The backward feedback in the digital twin refers to the ability to use simulation results to inform engineering decision-making. Once the finite element model is updated in real time to reflect the latest structural state, it can extract physically meaningful failure indicators, such as the maximum allowable scour depth and settlement thresholds. These indicators provide valuable insights for maintenance planning. In this way, the digital twin is not merely a passive reflection of structural conditions, but an intelligent system that actively contributes to operational and maintenance decisions.

7.2.2. Two-level early warning system.

The first level of warning is based on the maximum allowable scour depth derived from FE simulation. This value is obtained by simulating the full progression of scouring. This threshold is then compared with field-monitored scour depth to trigger early warning. A safety margin is applied to allow for advance intervention. The second level of warning is based on structural indicators such as abrupt changes in boundary conditions (e.g., pier settlement and rotation). These changes are associated with the structural failure.

The effectiveness of several failure indicators is evaluated in terms of observability, robustness to noise and environmental disturbance, and sensitivity to scour damage. Pier settlement and rotation are eventually identified as the most suitable indicators, and their monitoring is recommended for field deployment.

7.2.3. Integration of multi-source sensors and external data.

The framework incorporates multiple sensor types into a unified decision-making system. Accelerometers and laser scanners are used to calibrate geometry and material parameters in the finite element model. FBG sensors based on vortex-induced vibrations are applied for real-time scour depth monitoring. By comparing the monitored scour depth with the simulated maximum allowable depth, the framework provides a basis to inform maintenance decisions.

These innovations ensure both the technical accuracy and practical utility of the system. More importantly, the proposed framework is adaptable to a wide range of bridge. Although specific numerical thresholds (such as the maximum allowable scour depth) may vary depending on the bridge type and hydraulic conditions, the underlying methodology is broadly applicable to other bridges.

7.3. Limitations of the current study

The proposed digital twin framework has proved its feasibility and robustness through the case study of the Regent Bridge. However, there are still several limitations that should be acknowledged:

First of all, due to the absence of underwater geometry data, the current model does not explicitly include the submerged portion of the bridge foundation. This omission may reduce the accuracy of scour simulation and limit the reliability of critical scour depth predictions. Future work should incorporate ground-penetrating radar (GPR) or sonar-based reconstruction techniques to address this issue.

Another modeling limitation concerns the use of a Winkler spring model in the finite element analysis, which assumes linear elastic behavior. This is usually adequate for early-stage scour with small deformations. Nevertheless, nonlinear soil–structure interactions become increasingly important as scour progresses. Hence, linear springs may become less suitable for the late stage of scour. To improve model fidelity, future studies should consider nonlinear spring elements.

Furthermore, there are limitations from the use of a homogeneous material model. In this study, the masonry is modeled as a homogeneous continuum, where the discrete nature of brick–mortar interfaces is neglected. This approach reduces computational cost but may miss local failure mechanisms such as joint sliding and cracking. Discrete micro-modeling has greater accuracy, however, as a trade-off, it requires additional computational resources and material input parameters.

Sensor layout optimization was based on a deterministic finite element model without considering parameter uncertainty propagation. Despite a sensitivity analysis, the layout may still be suboptimal under varying model parameters. More robust layout strategies should consider the uncertainty and measurement noise in the optimization process.

In conclusion, these limitations do not present fundamental technical barriers to implementation. In many cases, they reflect practical constraints, such as data availability or field accessibility. In other cases, they result from methodological trade-offs between modeling complexity and computational cost.

7.4. Future research recommendation

Corresponding to the limitations, several future research directions are identified to improve current work:

The accuracy of the DT framework could be significantly improved in the future by incorporating geometric information of the submerged substructure. Non-destructive testing techniques can be powerful tools to reconstruct the underwater portions of masonry bridges, including foundation depth and type.

The finite element model in this study utilizes linear springs, which assume a constant elastic stiffness. This simplification is generally acceptable under small-deformation assumptions. However,

in practice, the relationship between structural deformation and spring response is often nonlinear. In the later stages of scour progression, where large deformations may occur, modeling accuracy can be improved by incorporating nonlinear springs within the finite element framework (for example, using the COMBIN39 spring element available in ANSYS). A similar enhancement may also be considered in the choice between homogenized and discrete modeling strategies. Discrete modeling treats bricks and mortar separately and uses contact elements to capture sliding and cracking between blocks. This method achieves a more realistic representation of structural nonlinearities. However, it also greatly increases computational demand. In summary, finite element modeling of masonry bridges involves a trade-off between accuracy and computational efficiency. Future studies should select modeling strategies based on the specific demands of each application scenario.

Further experimental and field validation of the FBG-based vortex flow sensor is also needed. Special attention should be given to its temporal sensitivity to scour depth variation, as well as mechanical robustness and corrosion resistance under harsh underwater conditions. Moreover, the sensor placement strategy proposed in this study demonstrates moderate robustness under stiffness perturbations. In order to develop a more resilient and reliable sensor placement algorithm, future research could incorporate uncertainty propagation into the sensor placement optimization.

The current digital twin model still contains uncertainties in material parameters. Therefore, ambient vibration tests are needed in the future to perform modal identification and update the model. This study conducted a sensitivity analysis to identify the most influential parameters affecting the structure's dynamic characteristics, serving as a preliminary step for the future model updating.

Last but not least, current efforts remain at the simulation and modeling stage. Future work should focus on incorporating these components into practical DT platforms, such as Bentley iTwin, Ansys Twin Builder, or Microsoft Azure Digital Twins, to support a broader application.

8 Conclusions

This thesis developed a digital twin-based framework for the structural health monitoring and predictive maintenance of masonry bridges subjected to scour. By integrating real-time scour data from FBG-based vortex flow sensors with physics-based finite element modeling, the framework enables closed-loop interaction between the physical structure and its virtual representation. Forward feedback from the physical layer supports dynamic model calibration, while backward feedback from the virtual model informs maintenance decisions and sensor deployment strategies. The framework addresses critical challenges in existing scour management practices, particularly the lack of model updating and calibration, mechanical feedback under scour, and limited sensor optimization methods. The main conclusions are summarized as follows:

1. Design of digital twin framework: A framework was designed for masonry bridge scour, incorporating physical, virtual, and connect layers. A closed-loop interaction was designed to realize both forward and backward feedback.
2. Structural health monitoring at the physical layer: This study explored the potential of FBG-based vortex flow sensors in scour monitoring. Compared to traditional FBG strain sensors, this system shows stronger resistance to debris interference during flooding events. Numerical simulations confirmed its capability to capture the scour depth evolution.
3. Finite element analysis at the virtual layer: A Winkler spring-based model was employed to simulate the scour process. The analysis revealed stress redistribution in the arch ring, from which the maximum allowable scour depth was determined. Several failure indicators were also evaluated, including pier settlement, first-order natural frequency, and mode localization factor. These indicators exhibited strong responses when the scour depth approached the structural limit state. For example, pier settlement undergoes a 25% variation when the bridge is near the failure state. For practical application, those indicators were further assessed, and the final options suggested by this study are the pier settlement and rotation due to their strong sensitivity to scour and ease of field monitoring.
4. Backward feedback via sensor optimization: An optimal sensor placement strategy was formulated to maximize information gain with a limited number of sensors. The Fisher information matrix and a greedy selection algorithm were applied to determine optimal sensor locations.
5. Trigger-based model updating strategy: A routine, hydrology- and structure-driven trigger mechanism was proposed to guide model updates, aiming to reduce the computational cost of the DT system when applied to real engineering cases.
6. Uncertainty quantification: Uncertainties may arise from both finite element modeling and the intrinsic degradation processes of materials. This thesis used a parameter perturbation approach to quantitatively identify the parameters that significantly influence the dynamic characteristics of the masonry bridge. Highly sensitive material parameters were identified,

providing guidance for selecting appropriate parameters for calibration during future model updating in digital twin applications. Furthermore, the impact of parameter perturbations on sensor placement optimization is also assessed. The results show that 60% of the sensor locations are robust to such uncertainties, while the remaining measurement points are susceptible to parameter variation.

In summary, this thesis develops a digital twin-inspired monitoring and maintenance framework tailored to scour management in masonry bridges. Through a case study in Regent bridge, this framework demonstrates its capability of transfering traditional maintenance to predictive maintenance.

References

[1] Luke J Prendergast and Kenneth Gavin. “A review of bridge scour monitoring techniques”. In: *Journal of Rock Mechanics and Geotechnical Engineering* 6.2 (2014), pp. 138–149.

[2] Les Hamill. *Bridge hydraulics*. CRC Press, 1998.

[3] Gijsbertus JCM Hoffmans. *Scour manual*. Routledge, 2017.

[4] Amro Nasr et al. “Bridges in a changing climate: A study of the potential impacts of climate change on bridges and their possible adaptations”. In: *Structure and Infrastructure Engineering* 16.4 (2020), pp. 738–749.

[5] Kristopher Campbell et al. “A review of the data held on 3,437 masonry arch bridges in Northern Ireland”. In: (2020).

[6] Paolo Zampieri et al. “Failure analysis of masonry arch bridges subject to local pier scour”. In: *Engineering Failure Analysis* 79 (2017), pp. 371–384.

[7] Alonso Pizarro, Salvatore Manfreda, and Enrico Tubaldi. “The science behind scour at bridge foundations: A review”. In: *Water* 12.2 (2020), p. 374.

[8] Rijksdienst voor het Cultureel Erfgoed. *Maastricht, de Servaasbrug...* Apr. 3, 2022. URL: `https://commons.wikimedia.org/...`.

[9] Sailko. *Ponte Vecchio Firenze*. Wikimedia Commons. July 14, 2008. URL: `https://commons.wikimedia.org/wiki/File:Ponte_Vecchio_Firenze.jpg`.

[10] Photographer Name. *Charles Bridge in Prague, Czech Republic*. Unsplash License. Year. URL: `https://unsplash.com/photos/photo_id`.

[11] Pline. *Vieux pont de Gien (7)*. Wikimedia Commons. June 2, 2008. URL: `https://commons.wikimedia.org/wiki/File:Vieux_pont_de_Gien_(7).JPG`.

[12] Lu Deng and CS Cai. “Bridge model updating using response surface method and genetic algorithm”. In: *Journal of Bridge Engineering* 15.5 (2010), pp. 553–564.

[13] AM Shirole and RC Holt. “Planning for a comprehensive bridge safety assurance program”. In: *Transportation Research Record* 1290.3950 (1991), pp. 39–50.

[14] Kumalasari Wardhana and Fabian C Hadipriono. “Analysis of recent bridge failures in the United States”. In: *Journal of performance of constructed facilities* 17.3 (2003), pp. 144–150.

[15] Wen Xiong et al. “Review of hydraulic bridge failures: historical statistic analysis, failure modes, and prediction methods”. In: *Journal of Bridge Engineering* 28.4 (2023), p. 03123001.

[16] Fabrizio Scozzese, Enrico Tubaldi, and Andrea Dall’Asta. “Damage metrics for masonry bridges under scour scenarios”. In: *Engineering Structures* 296 (2023), p. 116914.

[17] Gene W Parker, Lisa Bratton, and David S Armstrong. *Stream stability and scour assessments at bridges in Massachusetts*. US Geological Survey Washington, DC, 1997.

[18] Bruce W Melville and Stephen E Coleman. *Bridge scour*. Water Resources Publication, 2000.

[19] MC Forde et al. “Radar measurement of bridge scour”. In: *Ndt & E International* 32.8 (1999), pp. 481–492.

[20] Fernando De Falco and Raffaele Mele. “The monitoring of bridges for scour by sonar and sedimetri”. In: *NDT & E International* 35.2 (2002), pp. 117–123.

[21] Wen Xiong, CS Cai, and Xuan Kong. “Instrumentation design for bridge scour monitoring using fiber Bragg grating sensors”. In: *Applied Optics* 51.5 (2012), pp. 547–557.

[22] Chung-Yue Wang, Hao-Lin Wang, and Chun-Che Ho. “A piezoelectric film type scour monitoring system for bridge pier”. In: *Advances in structural engineering* 15.6 (2012), pp. 897–905.

[23] Abdollah Malekjafarian et al. “Experimental demonstration of a mode shape-based scour-monitoring method for multispan bridges with shallow foundations”. In: *Journal of Bridge Engineering* 25.8 (2020), p. 04020050.

[24] Luke J Prendergast, Kenneth Gavin, and David Hester. “Isolating the location of scour-induced stiffness loss in bridges using local modal behaviour”. In: *Journal of Civil Structural Health Monitoring* 7 (2017), pp. 483–503.

[25] O Bouzas et al. “Reliability-based structural assessment of historical masonry arch bridges: The case study of Cernadela bridge”. In: *Case Studies in Construction Materials* 18 (2023), e02003.

[26] D Brackenbury, I Brilakis, and M DeJong. “Automated defect detection for masonry arch bridges”. In: *International Conference on Smart Infrastructure and Construction 2019 (ICSIC) Driving data-informed decision-making*. ICE Publishing. 2019, pp. 3–9.

[27] B Conde et al. “Parameter identification for damaged condition investigation on masonry arch bridges using a Bayesian approach”. In: *Engineering Structures* 172 (2018), pp. 275–284.

[28] Paolo Zampieri, Mariano Angelo Zanini, and Flora Faleschini. “Influence of damage on the seismic failure analysis of masonry arches”. In: *Construction and Building Materials* 119 (2016), pp. 343–355.

[29] N Cavalagli et al. “Hierarchical environmental risk mapping of material degradation in historic masonry buildings: An integrated approach considering climate change and structural damage”. In: *Construction and Building Materials* 215 (2019), pp. 998–1014.

[30] Antonio Maria D’altri et al. “Modeling strategies for the computational analysis of unreinforced masonry structures: review and classification”. In: *Archives of computational methods in engineering* 27 (2020), pp. 1153–1185.

[31] Jigme Dorji et al. “Strength assessment of old masonry arch bridges through moderate destructive testing methods”. In: *Construction and Building Materials* 278 (2021), p. 122391.

[32] Charles R Farrar and Keith Worden. “An introduction to structural health monitoring”. In: *Philosophical Transactions of the Royal Society A: Mathematical, Physical and Engineering Sciences* 365.1851 (2007), pp. 303–315.

[33] Jean-Louis Briaud, Mabel Chedid, et al. *Allowable Limit Contraction and Abutment Scour at Bridges: Technical Report*. Tech. rep. Texas A&M Transportation Institute, 2019.

[34] Jacques Heyman. *The mansonry arch*. 1982.

[35] Michael W Grieves. “Product lifecycle management: the new paradigm for enterprises”. In: *International Journal of Product Development* 2.1-2 (2005), pp. 71–84.

[36] Eric VanDerHorn and Sankaran Mahadevan. “Digital Twin: Generalization, characterization and implementation”. In: *Decision support systems* 145 (2021), p. 113524.

[37] Krishnamoorthi Sivalingam et al. “A review and methodology development for remaining useful life prediction of offshore fixed and floating wind turbine power converter with digital twin technology perspective”. In: *2018 2nd international conference on green energy and applications (ICGEA)*. IEEE. 2018, pp. 197–204.

[38] Javier Sánchez-Haro et al. “Digital twin for predictive maintenance on the Espartxo Bridge. Application to early detection of under-foundation scour”. In: *Structures*. Vol. 71. Elsevier. 2025, p. 107916.

[39] Michael G Kapteyn et al. “Data-driven physics-based digital twins via a library of component-based reduced-order models”. In: *International Journal for Numerical Methods in Engineering* 123.13 (2022), pp. 2986–3003.

[40] Stein Ove Erikstad. “Merging physics, big data analytics and simulation for the next-generation digital twins”. In: *High-performance marine vehicles* (2017), pp. 141–151.

[41] Yu Zheng, Sen Yang, and Huanchong Cheng. “An application framework of digital twin and its case study”. In: *Journal of ambient intelligence and humanized computing* 10 (2019), pp. 1141–1153.

[42] Maria Pregnolato et al. “Towards Civil Engineering 4.0: Concept, workflow and application of Digital Twins for existing infrastructure”. In: *Automation in Construction* 141 (2022), p. 104421.

[43] Rolando Chacón et al. “Requirements and challenges for infusion of SHM systems within Digital Twin platforms”. In: *Structure and Infrastructure Engineering* 21.4 (2025), pp. 599–615.

[44] He Liu et al. “Digital Twin-Driven Machine Condition Monitoring: A Literature Review”. In: *Journal of Sensors* 2022.1 (2022), p. 6129995.

[45] Maggie Mashaly. “Connecting the twins: A review on digital twin technology & its networking requirements”. In: *Procedia Computer Science* 184 (2021), pp. 299–305.

[46] Kuo Tian et al. “Novel optimal sensor placement method towards the high-precision digital twin for complex curved structures”. In: *International Journal of Solids and Structures* 302 (2024), p. 113003.

[47] Shuo Wang et al. “Optimal sensor placement for digital twin based on mutual information and correlation with multi-fidelity data”. In: *Engineering with Computers* 40.2 (2024), pp. 1289–1308.

[48] Paul J Vardanega et al. “A review of recent research on visual inspection processes for bridges and the potential uses of AI”. In: *Bridge Maintenance, Safety, Management, Digitalization and Sustainability* (2024), pp. 3573–3580.

[49] Łukasz Topczewski et al. “Monitoring of scour around bridge piers and abutments”. In: *Transportation Research Procedia* 14 (2016), pp. 3963–3971.

[50] Neil L Anderson, Ahmed M Ismael, and Thanop Thitimakorn. “Ground-penetrating radar: a tool for monitoring bridge scour”. In: *Environmental & Engineering Geoscience* 13.1 (2007), pp. 1–10.

[51] Doyle J Webb et al. “Bridge scour: Application of ground penetrating radar”. In: *Proceedings of the First International Conference on the Application of Geophysical Methodologies and NDT to Transportation Facilities and Infrastructure*. Citeseer. 2000.

[52] Sivasakthy Selvakumaran et al. “Remote monitoring to predict bridge scour failure using Interferometric Synthetic Aperture Radar (InSAR) stacking techniques”. In: *International journal of applied earth observation and geoinformation* 73 (2018), pp. 463–470.

[53] NE Yankielun and L Zabilansky. “Laboratory investigation of time-domain reflectometry system for monitoring bridge scour”. In: *Journal of Hydraulic engineering* 125.12 (1999), pp. 1279–1284.

[54] Xinbao Yu and Xiong Yu. “Time domain reflectometry automatic bridge scour measurement system: principles and potentials”. In: *Structural Health Monitoring* 8.6 (2009), pp. 463–476.

[55] Paul J Vardanega, Gianna Gavriel, and Maria Pregnolato. “Assessing the suitability of bridge-scour-monitoring devices”. In: *Proceedings of the Institution of Civil Engineers-Forensic Engineering* 174.4 (2021), pp. 105–117.

[56] Yung-Bin Lin et al. “Real-time monitoring of local scour by using fiber Bragg grating sensors”. In: *Smart materials and structures* 14.4 (2005), p. 664.

[57] Zhi Zhou et al. “An optical fiber Bragg grating sensing system for scour monitoring”. In: *Advances in Structural Engineering* 14.1 (2011), pp. 67–78.

[58] Yung Bin Lin et al. “Flood scour monitoring system using fiber Bragg grating sensors”. In: *Smart materials and Structures* 15.6 (2006), p. 1950.

[59] Xuan Kong et al. “Scour monitoring system using fiber Bragg grating sensors and water-swellable polymers”. In: *Journal of Bridge Engineering* 22.7 (2017), p. 04017029.

[60] Yong Ding et al. “A new method for scour monitoring based on fiber Bragg grating”. In: *Measurement* 127 (2018), pp. 431–435.

[61] Gianluca Crotti and Stefano Manzoni. “In-field assessment of bridge pier scour by means of Fiber Bragg Gratings: System and algorithms”. In: *Measurement* 242 (2025), p. 116030.

[62] Kristopher Campbell et al. “Development of a prototype bridge scour sensor exploiting vortex-induced vibrations”. In: *Proceedings of the Institution of Civil Engineers-Bridge Engineering*. Emerald Publishing Limited. 2024, pp. 1–25.

[63] Salih O Duffuaa et al. “A generic conceptual simulation model for maintenance systems”. In: *Journal of Quality in Maintenance Engineering* 7.3 (2001), pp. 207–219.

[64] Rosmaini Ahmad and Shahrul Kamaruddin. “An overview of time-based and condition-based maintenance in industrial application”. In: *Computers & industrial engineering* 63.1 (2012), pp. 135–149.

[65] Guojing Zhang et al. “Causes and statistical characteristics of bridge failures: A review”. In: *Journal of traffic and transportation engineering (English edition)* 9.3 (2022), pp. 388–406.

[66] Wai-Fah Chen and Lian Duan. *Bridge engineering handbook: construction and maintenance*. Vol. 5. CRC press, 2014.

[67] Joseph L. Hartmann. *Memorandum: National Bridge Inspection Standards (NBIS) Inspection Interval Guidance*. `https://www.fhwa.dot.gov/bridge/pubs/memo_inspection_interval_guidance.pdf`. Federal Highway Administration (FHWA), Office of Bridges and Structures. June 2022.

[68] Praeparatus. *Build Resilience: Bridge Inspections, Scour Risk Rating and Building in Resilience*. `https://praeparatus.com/build-resilience/`. Accessed: April 22, 2025. 2025.

[69] YQ Ni and KY Wong. “Integrating bridge structural health monitoring and condition-based maintenance management”. In: *4th International workshop on civil structural health monitoring*. 2012, pp. 6–8.

[70] Ting Dong, Raphael T Haftka, and Nam H Kim. “Advantages of condition-based maintenance over scheduled maintenance using structural health monitoring system”. In: *Reliability and Maintenance-An Overview of Cases*. IntechOpen, 2019.

[71] Charles R Farrar and Keith Worden. *Structural health monitoring: a machine learning perspective*. John Wiley & Sons, 2012.

[72] Deepam Goyal and BS Pabla. “The vibration monitoring methods and signal processing techniques for structural health monitoring: a review”. In: *Archives of Computational Methods in Engineering* 23 (2016), pp. 585–594.

[73] Jerome Peter Lynch. “An overview of wireless structural health monitoring for civil structures”. In: *Philosophical Transactions of the Royal Society A: Mathematical, Physical and Engineering Sciences* 365.1851 (2007), pp. 345–372.

[74] Song Honghong et al. “Digital twin enhanced BIM to shape full life cycle digital transformation for bridge engineering”. In: *Automation in Construction* 147 (2023), p. 104736.

[75] Farid Ghahari et al. “Bridge digital twinning using an output-only Bayesian model updating method and recorded seismic measurements”. In: *Sensors* 22.3 (2022), p. 1278.

[76] Guoliang Shi et al. “Digital twin-based model updating method for mechanical behaviors analysis of cable truss structure”. In: *Journal of Constructional Steel Research* 221 (2024), p. 108917.

[77] Eva Brucherseifer et al. “Digital Twin conceptual framework for improving critical infrastructure resilience”. In: *at-Automatisierungstechnik* 69.12 (2021), pp. 1062–1080.

[78] Jianlin Wu et al. “A dynamic holographic modelling method of digital twin scenes for bridge construction”. In: *International Journal of Digital Earth* 16.1 (2023), pp. 2404–2425.

[79] Abdurahman Yasin Yiğit and Murat Uysal. “Virtual reality visualisation of automatic crack detection for bridge inspection from 3D digital twin generated by UAV photogrammetry”. In: *Measurement* 242 (2025), p. 115931.

[80] Sakdirat Kaewunruen et al. “Digital twins for managing railway bridge maintenance, resilience, and climate change adaptation”. In: *Sensors* 23.1 (2022), p. 252.

[81] Fei Jiang et al. “Digital Twin-driven framework for fatigue life prediction of steel bridges using a probabilistic multiscale model: Application to segmental orthotropic steel deck specimen”. In: *Engineering Structures* 241 (2021), p. 112461.

[82] Guo-Qing Zhang et al. “Simulation and prediction of vortex-induced vibration of a long suspension bridge using SHM-based digital twin technology”. In: *Journal of Wind Engineering and Industrial Aerodynamics* 247 (2024), p. 105705.

[83] Kaiqi Lin et al. “Digital twin-based collapse fragility assessment of a long-span cable-stayed bridge under strong earthquakes”. In: *Automation in Construction* 123 (2021), p. 103547.

[84] Fei Hu et al. “Digital twin-based fatigue life assessment of orthotropic steel bridge decks using inspection robot and deep learning”. In: *Automation in Construction* 172 (2025), p. 106022.

[85] Dong Zhong et al. “Overview of predictive maintenance based on digital twin technology”. In: *Heliyon* 9.4 (2023).

[86] IB Muhit et al. “A framework for digital twinning of masonry arch bridges”. In: *Life-Cycle of Structures and Infrastructure Systems*. CRC Press, 2023, pp. 817–824.

[87] Borja Conde et al. “Probabilistic-based structural assessment of a historic stone arch bridge”. In: *Structure and Infrastructure Engineering* 17.3 (2021), pp. 379–391.

[88] Els Verstrynge, Luc Schueremans, and Dionys Van Gemert. “Time-dependent mechanical behavior of lime-mortar masonry”. In: *Materials and structures* 44 (2011), pp. 29–42.

[89] Bruce W Melville and Arved J Raudkivi. “Effects of foundation geometry on bridge pier scour”. In: *Journal of Hydraulic Engineering* 122.4 (1996), pp. 203–209.

[90] Bora Pulatsu, Ece Erdogmus, and Paulo B Lourenço. “Comparison of in-plane and out-of-plane failure modes of masonry arch bridges using discontinuum analysis”. In: *Engineering Structures* 178 (2019), pp. 24–36.

[91] Daniel V Oliveira, Paulo B Lourenço, and Cláudia Lemos. “Geometric issues and ultimate load capacity of masonry arch bridges from the northwest Iberian Peninsula”. In: *Engineering Structures* 32.12 (2010), pp. 3955–3965.

[92] Yanyang Zhang, Lorenzo Macorini, and Bassam A Izzuddin. “Numerical investigation of arches in brick-masonry bridges”. In: *Structure and Infrastructure Engineering* 14.1 (2018), pp. 14–32.

[93] Vicente N Moreira, José C Matos, and Daniel V Oliveira. “Probabilistic-based assessment of a masonry arch bridge considering inferential procedures”. In: *Engineering Structures* 134 (2017), pp. 61–73.

[94] Neda M Sokolović et al. “Inspection and assessment of masonry arch bridges: Ivanjica case study”. In: *Sustainability* 13.23 (2021), p. 13363.

[95] Styliani Verykokou and Charalabos Ioannidis. “An overview on image-based and scanner-based 3D modeling technologies”. In: *Sensors* 23.2 (2023), p. 596.

[96] B Riveiro et al. “Photogrammetric 3D modelling and mechanical analysis of masonry arches: An approach based on a discontinuous model of voussoirs”. In: *Automation in Construction* 20.4 (2011), pp. 380–388.

[97] Maria E Stavroulaki et al. “Modelling and strength evaluation of masonry bridges using terrestrial photogrammetry and finite elements”. In: *Advances in Engineering Software* 101 (2016), pp. 136–148.

[98] Massimiliano Pepe and Domenica Costantino. “UAV photogrammetry and 3D modelling of complex architecture for maintenance purposes: The case study of the masonry bridge on the Sele river, Italy”. In: *Periodica Polytechnica Civil Engineering* 65.1 (2021), pp. 191–203.

[99] C Biscarini et al. “UAV photogrammetry, infrared thermography and GPR for enhancing structural and material degradation evaluation of the Roman masonry bridge of Ponte Lucano in Italy”. In: *NDT & E International* 115 (2020), p. 102287.

[100] P Arias et al. “Digital photogrammetry, GPR and computational analysis of structural damages in a mediaeval bridge”. In: *Engineering Failure Analysis* 14.8 (2007), pp. 1444–1457.

[101] Hyo Seon Park et al. “A new approach for health monitoring of structures: terrestrial laser scanning”. In: *Computer-Aided Civil and Infrastructure Engineering* 22.1 (2007), pp. 19–30.

[102] Belén Riveiro et al. “Validation of terrestrial laser scanning and photogrammetry techniques for the measurement of vertical underclearance and beam geometry in structural inspection of bridges”. In: *Measurement* 46.1 (2013), pp. 784–794.

[103] B Riveiro et al. “Terrestrial laser scanning and limit analysis of masonry arch bridges”. In: *Construction and building materials* 25.4 (2011), pp. 1726–1735.

[104] J Armesto et al. “Modelling masonry arches shape using terrestrial laser scanning data and nonparametric methods”. In: *Engineering Structures* 32.2 (2010), pp. 607–615.

[105] Saeed Talebi et al. “The development of a digitally enhanced visual inspection framework for masonry bridges in the UK”. In: *Construction Innovation* 22.3 (2022), pp. 624–646.

[106] Danielle S Willkens, Junshan Liu, and Shadi Alathamneh. “A case study of integrating terrestrial laser scanning (TLS) and building information modeling (BIM) in heritage bridge documentation: The Edmund Pettus Bridge”. In: *Buildings* 14.7 (2024), p. 1940.

[107] Izabela Lubowiecka et al. “Historic bridge modelling using laser scanning, ground penetrating radar and finite element methods in the context of structural dynamics”. In: *Engineering Structures* 31.11 (2009), pp. 2667–2676.

[108] Mercedes Solla et al. “Ground-penetrating radar for the structural evaluation of masonry bridges: Results and interpretational tools”. In: *Construction and Building Materials* 29 (2012), pp. 458–465.

[109] M Solla et al. “A novel methodology for the structural assessment of stone arches based on geometric data by integration of photogrammetry and ground-penetrating radar”. In: *Engineering structures* 35 (2012), pp. 296–306.

[110] Juan Pedro Cortés Pérez et al. “Assessment of the structural integrity of the Roman Bridge of Alcántara (Spain) using TLS and GPR”. In: *Remote Sensing* 10.3 (2018), p. 387.

[111] Antonio Brencich and Donato Sabia. “Experimental identification of a multi-span masonry bridge: The Tanaro Bridge”. In: *Construction and Building Materials* 22.10 (2008), pp. 2087–2099.

[112] Fanis Moschas and Stathis Stiros. “Measurement of the dynamic displacements and of the modal frequencies of a short-span pedestrian bridge using GPS and an accelerometer”. In: *Engineering structures* 33.1 (2011), pp. 10–17.

[113] Alban Kita et al. “A new method for earthquake-induced damage identification in historic masonry towers combining OMA and IDA”. In: *Bulletin of Earthquake Engineering* 19.12 (2021), pp. 5307–5337.

[114] Fabrizio Scozzese et al. “Modal properties variation and collapse assessment of masonry arch bridges under scour action”. In: *Engineering Structures* 199 (2019), p. 109665.

[115] Hoa Tran-Ngoc et al. “Model updating for Nam O bridge using particle swarm optimization algorithm and genetic algorithm”. In: *Sensors* 18.12 (2018), p. 4131.

[116] Tao Liu et al. “Finite element model updating of canonica bridge using experimental modal data and genetic algorithm”. In: *Structural Engineering International* 26.1 (2016), pp. 27–36.

[117] Cristina Costa et al. “Updating numerical models of masonry arch bridges by operational modal analysis”. In: *International Journal of Architectural Heritage* 9.7 (2015), pp. 760–774.

[118] Giacomo Zini et al. “Structural health monitoring of a masonry arch bridge: modal identification and model updating”. In: *International Journal of Masonry Research and Innovation* 9.1-2 (2024), pp. 42–53.

[119] Chiara Pepi et al. “An integrated approach for the numerical modeling of severely damaged historic structures: Application to a masonry bridge”. In: *Advances in Engineering Software* 151 (2021), p. 102935.

[120] Enrico Tubaldi, Lorenzo Macorini, and Bassam A Izzuddin. “Three-dimensional mesoscale modelling of multi-span masonry arch bridges subjected to scour”. In: *Engineering Structures* 165 (2018), pp. 486–500.

[121] Yidan Han, Qing Chun, and Xiaoyue Gao. “Flood-induced forces and collapse mechanism of historical multi-span masonry arch bridges: The Putang bridge case”. In: *Engineering Failure Analysis* 153 (2023), p. 107564.

[122] Amaryllis Audenaert, Herbert Peremans, and Genserik Reniers. “An analytical model to determine the ultimate load on masonry arch bridges.” In: *Journal of Engineering Mathematics* 59 (2007), pp. 323–336.

[123] Jofin George and Arun Menon. “A mechanism-based assessment framework for masonry arch bridges under scour-induced support rotation”. In: *Advances in Structural Engineering* 24.12 (2021), pp. 2637–2651.

[124] Daniele Gaetano et al. “An interface-based detailed micro-model for the failure simulation of masonry structures”. In: *Engineering Failure Analysis* 142 (2022), p. 106753.

[125] Vildan G Mentese et al. “Experimental collapse investigation and nonlinear modeling of a single-span stone masonry arch bridge”. In: *Engineering Failure Analysis* 152 (2023), p. 107520.

[126] Semih Gönen and Serdar Soyöz. “Seismic analysis of a masonry arch bridge using multiple methodologies”. In: *Engineering Structures* 226 (2021), p. 111354.

[127] Jofin George and Arun Menon. “Analytical fragility curves for displacement-based scour assessment of masonry arch bridges”. In: *Structures*. Vol. 46. Elsevier. 2022, pp. 172–185.

[128] Texas Department of Transportation. *Scour Evaluation Guide*. Revised July 2023. TxDOT. July 2023. URL: https://ftp.txdot.gov/pub/txdot-info/library/pubs/bus/bridge/scour-guide.pdf.

[129] X Kong et al. “Field application of an innovative bridge scour monitoring system with fiber Bragg grating sensors”. In: *Journal of aerospace engineering* 30.2 (2017), B4016008.

[130] Kai Tan et al. “Investigation of TLS intensity data and distance measurement errors from target specular reflections”. In: *Remote Sensing* 10.7 (2018), p. 1077.

[131] Encyclopaedia Britannica. *River Lagan*. https://www.britannica.com/place/River-Lagan.

[132] Department for Infrastructure, Northern Ireland. *Strategic Flood Map (NI) —Web Viewer*. https://dfi-ni.maps.arcgis.com/apps/webappviewer/index.html?id=fd6c0a01b07840269a50a2f596b3daf6. Accessed: 2025-05-05. 2024.

[133] Highways England. “CS 450 Inspection of highway structures”. In: *The National Archives: London, UK* (2020).

[134] National Highways. *CS 469: Management of Scour and Other Hydraulic Actions at Highway Structures*. https://www.standardsforhighways.co.uk/dmrb. Design Manual for Roads and Bridges (DMRB), Version 1.0.0, April 2024. 2024.

[135] Paul J Besl and Neil D McKay. “Method for registration of 3-D shapes”. In: *Sensor fusion IV: control paradigms and data structures*. Vol. 1611. Spie. 1992, pp. 586–606.

[136] C Costa et al. “Calibration of the numerical model of a stone masonry railway bridge based on experimentally identified modal parameters”. In: *Engineering Structures* 123 (2016), pp. 354–371.

[137] Stefano Pagliara and Iacopo Carnacina. “Temporal scour evolution at bridge piers: Effect of wood debris roughness and porosity”. In: *Journal of Hydraulic Research* 48.1 (2010), pp. 3–13.

[138] Bijan Dargahi. “Flow field and local scouring around a cylinder.” In: (1990).

[139] Zamri Chik and Luis E Vallejo. “Characterization of the angle of repose of binary granular materials”. In: *Canadian Geotechnical Journal* 42.2 (2005), pp. 683–692.

[140] Serkan Tapkın et al. “Structural investigation of masonry arch bridges using various nonlinear finite-element models”. In: *Journal of Bridge Engineering* 27.7 (2022), p. 04022053.

[141] Paul J Fanning, Thomas E Boothby, and Benjamin J Roberts. “Longitudinal and transverse effects in masonry arch assessment”. In: *Construction and Building Materials* 15.1 (2001), pp. 51–60.

[142] Niamh Gibbons and Paul J Fanning. “Progressive cracking of masonry arch bridges”. In: *Proceedings of the Institution of Civil Engineers-Bridge Engineering*. Vol. 169. 2. Thomas Telford Ltd. 2016, pp. 93–112.

[143] Daniel Girardeau-Montaut et al. “CloudCompare”. In: *France: EDF R&D Telecom ParisTech* 11.5 (2016), p. 2016.

[144] Brian Solan et al. “Scour-induced failure of masonry arch bridges: Causes and countermeasures”. In: *E-proceedings of the 38th IAHR World Congress*. 2019.

[145] Richard Mathews and Martin Hardman. “Lessons learnt from the December 2015 flood event in Cumbria, UK”. In: *Proceedings of the Institution of Civil Engineers-Forensic Engineering* 170.4 (2017), pp. 165–178.

[146] Amirhosein Shabani and Mahdi Kioumarsi. “Seismic assessment and strengthening of a historical masonry bridge considering soil-structure interaction”. In: *Engineering Structures* 293 (2023), p. 116589.

[147] Andreas J Kappos, Gregory G Penelis, and Christos G Drakopoulos. “Evaluation of simplified models for lateral load analysis of unreinforced masonry buildings”. In: *Journal of structural Engineering* 128.7 (2002), pp. 890–897.

[148] Nagavinothini Ravichandran, Daniele Losanno, and Fulvio Parisi. “Comparative assessment of finite element macro-modelling approaches for seismic analysis of non-engineered masonry constructions”. In: *Bulletin of Earthquake engineering* 19 (2021), pp. 5565–5607.

[149] Rúben Silva et al. “Numerical simulations of experimental material testing in stone masonry arch railway bridges”. In: *Structure and Infrastructure Engineering* 20.5 (2024), pp. 633–652.

[150] ANSYS Inc. *Drucker–Prager Concrete Model*. https://ansyshelp.ansys.com/public/account/secured?returnurl=/Views/Secured/corp/v242/en/ans_mat/mat_geomechanics.html#matgeomechDPconc. Accessed: July 6, 2025. 2024.

[151] George Gazetas. “Formulas and charts for impedances of surface and embedded foundations”. In: *Journal of geotechnical engineering* 117.9 (1991), pp. 1363–1381.

[152] Ruth Harley et al. “Geotechnical failure risk reviewed”. In: *Transportation Professional* (2015), pp. 24–25.

[153] Alberto Barontini et al. “An overview on nature-inspired optimization algorithms for Structural Health Monitoring of historical buildings”. In: *Procedia engineering* 199 (2017), pp. 3320–3325.

[154] Paolo Borlenghi et al. “Long-term monitoring of a masonry arch bridge to evaluate scour effects”. In: *Construction and Building Materials* 411 (2024), p. 134580.

[155] Luke J Prendergast et al. “An investigation of the changes in the natural frequency of a pile affected by scour”. In: *Journal of sound and vibration* 332.25 (2013), pp. 6685–6702.

[156] Zhen Wang et al. “Eliminating environmental and operational effects on structural modal frequency: A comprehensive review”. In: *Structural Control and Health Monitoring* 29.11 (2022), e3073.

[157] Junwei Xiong et al. “Study on mode localization and mode transition of high arch dam caused by explosion horizontal cracks”. In: *Engineering Structures* 329 (2025), p. 119690.

[158] Charles R Farrar and Scott W Doebling. “An overview of modal-based damage identification methods”. In: (1997).

[159] V Askegaard and P Mossing. “Long term observation of rc-bridge using changes in natural frequency. nordic concrete research. publication no 7”. In: *Publication of: NORDIC CONCRETE FEDERATION* (1988).

[160] Hoon Sohn. “Effects of environmental and operational variability on structural health monitoring”. In: *Philosophical Transactions of the Royal Society A: Mathematical, Physical and Engineering Sciences* 365.1851 (2007), pp. 539–560.

[161] A Venugopal, Amit Agrawal, and SV Prabhu. “Performance evaluation of piezoelectric and differential pressure sensor for vortex flowmeters”. In: *Measurement* 50 (2014), pp. 10–18.

[162] Tamotsu Igarashi. “Flow resistance and Strouhal number of a vortex shedder in a circular pipe”. In: *JSME International Journal Series B Fluids and Thermal Engineering* 42.4 (1999), pp. 586–595.

[163] Pijush K Kundu et al. *Fluid mechanics*. Elsevier, 2024.

[164] Honglei Bai and Md Mahbub Alam. “Dependence of square cylinder wake on Reynolds number”. In: *Physics of Fluids* 30.1 (2018).

[165] Florian R Menter, Martin Kuntz, Robin Langtry, et al. “Ten years of industrial experience with the SST turbulence model”. In: *Turbulence, heat and mass transfer* 4.1 (2003), pp. 625–632.

[166] Florian R Menter. “Elements of inductrial heat tranfer predictions”. In: *16th Brazilian Congress of Mechanical Engineering (COBEM), Uberlandia, Brazil, 2001*. 2001.

[167] Beomkeun Kim et al. “A comparison among Neo-Hookean model, Mooney-Rivlin model, and Ogden model for chloroprene rubber”. In: *International Journal of Precision Engineering and Manufacturing* 13 (2012), pp. 759–764.

[168] Melvin Mooney. “A theory of large elastic deformation”. In: *Journal of applied physics* 11.9 (1940), pp. 582–592.

[169] J Krmela et al. “Determination of material parameters of rubber and composites for computational modeling based on experiment data”. In: *Journal of Physics: Conference Series*. Vol. 1741. 1. IOP Publishing. 2021, p. 012047.

[170] Tao Li et al. “Digital twin for intelligent tunnel construction”. In: *Automation in Construction* 158 (2024), p. 105210.

[171] Antonios Kamariotis, Eleni Chatzi, and Daniel Straub. “Value of information from vibration-based structural health monitoring extracted via Bayesian model updating”. In: *Mechanical Systems and Signal Processing* 166 (2022), p. 108465.

[172] Cyrille Stephan. “Sensor placement for modal identification”. In: *Mechanical Systems and Signal Processing* 27 (2012), pp. 461–470.

[173] S Dorvash and SN Pakzad. “Effects of measurement noise on modal parameter identification”. In: *Smart materials and structures* 21.6 (2012), p. 065008.

[174] Yu Xin, Hong Hao, and Jun Li. “Operational modal identification of structures based on improved empirical wavelet transform”. In: *Structural Control and Health Monitoring* 26.3 (2019), e2323.

[175] Wenliang Zhou and David Chelidze. “Blind source separation based vibration mode identification”. In: *Mechanical systems and signal processing* 21.8 (2007), pp. 3072–3087.

[176] Enrico Tubaldi et al. “Invited perspectives: Challenges and future directions in improving bridge flood resilience”. In: *Natural Hazards and Earth System Sciences Discussions* 2021 (2021), pp. 1–21.

[177] Maria J Machado et al. “Flood frequency analysis of historical flood data under stationary and non-stationary modelling”. In: *Hydrology and Earth System Sciences* 19.6 (2015), pp. 2561–2576.

[178] Marco Luppichini et al. “Deep learning models to predict flood events in fast-flowing watersheds”. In: *Science of the total environment* 813 (2022), p. 151885.

[179] Jian He et al. “Deep learning enables super-resolution hydrodynamic flooding process modeling under spatiotemporally varying rainstorms”. In: *Water Research* 239 (2023), p. 120057.

[180] Qianqian Zhou et al. “A deep-learning-technique-based data-driven model for accurate and rapid flood predictions in temporal and spatial dimensions”. In: *Hydrology and Earth System Sciences* 27.9 (2023), pp. 1791–1808.

[181] Wei-Jian Yi et al. “Identification of localized frame parameters using higher natural modes”. In: *Engineering Structures* 30.11 (2008), pp. 3082–3094.

[182] L Yu et al. “Application of eigenvalue perturbation theory for detecting small structural damage using dynamic responses”. In: *Composite Structures* 78.3 (2007), pp. 402–409.

Appendix A. Sensor placement optimization code

```python
"""
sensor_placement_fim_redundancy.py
"""
import pandas as pd
import numpy as np
import os
from typing import List

## Parameters ##
step_files = [f "Step{i}.xlsx" for i in range(7)]
top_n = 200       # number of candidate nodes
k = 10            # number of sensors to place
alpha = 0.1
beta = 0.2
redund_cutoff = 0.5
out_csv = "recommended_nodes_fim.csv"

# Load deformation data from steps
def load_steps(step_files):
    all_data = None
    for i, file in enumerate(step_files):
        if not os.path.exists(file):
            print(f"Missing file: {file}")
            continue
        df = pd.read_excel(file)
        df = df.rename(columns={"Node Number": "Node", "Total Deformation (m)": f"def{i}"})
        df = df[["Node", f"def{i}"]]
        df[f"def{i}"] = pd.to_numeric(df[f"def{i}"], errors="coerce")
        if all_data is None:
            all_data = df
        else:
            all_data = all_data.merge(df, on="Node")
    return all_data

# Compute Fisher information determinant
def compute_fim(sel, phi):
    x = phi[sel, :]
    q = x @ x.T
    return abs(np.linalg.det(q))

# Redundancy between two nodes
def redundancy(i, j, phi):
    fi = phi[i]
    fj = phi[j]
    Ii = np.outer(fi, fi)
    Ij = np.outer(fj, fj)
    num = np.linalg.norm(Ii - Ij)
    denom = np.linalg.norm(Ii + Ij)
    if denom == 0:
```

```
            return 0
        return num / denom

# Greedy sensor selection
def select_nodes(phi, candidates, k, alpha=0.0, beta=0.0, threshold=0.5):
    selected = [candidates[0]]
    rest = candidates[1:]
    total_nodes = phi.shape[0]

    while len(selected) < k and rest:
        best_score = -1e10
        best_node = None
        for idx in rest:
            min_r = min([redundancy(idx, s, phi) for s in selected])
            if min_r < threshold:
                continue
            score = compute_fim(selected + [idx], phi)
            score += alpha * min([abs(idx - s) for s in selected]) / (total_nodes - 1)
            score += beta * min_r
            if score > best_score:
                best_score = score
                best_node = idx
        if best_node is None:
            threshold *= 0.7  # relax the threshold
            continue
        selected.append(best_node)
        rest.remove(best_node)
    return selected

# Main process
def main():
    print("Loading deformation data...")
    df = load_steps(step_files)
    phi = df.filter(regex="^def").to_numpy(dtype=float)

    # Normalize
    max_vals = np.max(np.abs(phi), axis=0)
    max_vals[max_vals == 0] = 1
    phi = phi / max_vals

    df["sum_def"] = np.abs(phi).sum(axis=1)
    df_top = df.nlargest(top_n, "sum_def").reset_index(drop=True)

    print("Running greedy optimization...")
    selected = select_nodes(phi[df_top.index], list(range(top_n)), k, alpha, beta, redund_cutoff)
    final_nodes = df_top.iloc[selected]["Node"].tolist()
    print("Selected nodes:", final_nodes)

    pd.DataFrame({"Recommended Node": final_nodes}).to_csv(out_csv, index=False)
    print("Result saved to", out_csv)

if __name__ == "__main__":
    main()
```

Appendix B. Greedy algorithm

To select K sensors from N_{cand} candidate nodes, the following greedy algorithm is applied:

1. Initialization: Set the candidate set $\mathcal{C} = \{1, 2, \ldots, N_{\text{cand}}\}$, and the selected set $\mathcal{S} = \emptyset$.
2. Select first node: Choose the node $i^\star$ with the largest R_i:

$$\mathcal{S} \leftarrow \{i^\star\}, \quad \mathcal{C} \leftarrow \mathcal{C} \setminus \{i^\star\}. \tag{1}$$

3. While $|\mathcal{S}| < K$, for each $i \in \mathcal{C}$:
   (a) Form the trial set $\mathcal{S}_i = \mathcal{S} \cup \{i\}$.
   (b) Construct

$$\mathbf{X}_i = \mathbf{\Phi}_{\text{aug}}(\mathcal{S}_i, :), \quad \mathbf{Q}_i = \mathbf{X}_i \, \mathbf{X}_i^{\mathsf{T}}. \tag{2}$$

   (c) Define the score:

$$\text{score}(i) = \det(\mathbf{Q}_i) + \alpha \cdot \frac{\min_{j \in \mathcal{S}} d(i,j)}{N_{\text{cand}} - 1} + \beta \min_{j \in \mathcal{S}} R_{ij}, \tag{3}$$

   where $d(i,j)$ is the distance between nodes i and j, and α is a weighting coefficient, and (α, β) are the weigh geometric dispersion and information independence, respectively.

4. Update: Choose the node $i^\star$ with the highest score:

$$\mathcal{S} \leftarrow \mathcal{S} \cup \{i^\star\}, \quad \mathcal{C} \leftarrow \mathcal{C} \setminus \{i^\star\}. \tag{4}$$

5. Repeat until $|\mathcal{S}| = K$.

Appendix C. Modal localization and transition

C.1. Mechanism of modal localization and transition

Scour around bridge piers can significantly alter the dynamic properties of masonry bridges by changing the local stiffness of the structure. Two critical modal phenomena may be observed as scour progresses: mode localization, where the vibration energy becomes spatially concentrated, and mode transition, where the order of natural frequencies and their corresponding mode shapes are altered.

C.1.1. Modal localization: Theory and conditions

Modal localization refers to the phenomenon where vibrational energy becomes spatially concentrated in a limited region of the structure, typically due to localized stiffness loss or changes in boundary conditions. This behavior is especially pronounced in higher-order modes, which are more sensitive to local irregularities, although not all high-order modes necessarily exhibit this effect.

Conditions for Modal Lomodal localization include:

- Significant local stiffness degradation, i.e., $\Delta K/K_0 \gg 0$;
- Dense distribution of modal shape;
- Structural discontinuities such as cracks, scour holes, or boundary constraint loss.

Nevertheless, not all higher-order modes necessarily undergo localization. Although higher-order modes are theoretically more susceptible to modal localization [181], not all higher-order modes exhibit localization in the presence of local damage. Only those modes with significant energy distribution near the damaged part will show sensitivity to local stiffness or mass changes.

C.1.2. Modal Transition: Perturbation and eigenvalue reordering

The starting point for modal analysis in structural dynamics is the equation of motion for a linear, undamped system:

$$[M]\ddot{\mathbf{q}}(t) + [K]\mathbf{q}(t) = \mathbf{0} \tag{5}$$

where $[M]$ and $[K]$ are the global mass and stiffness matrices of the structure, and $\mathbf{q}(t)$ is the vector of nodal displacements. Assuming harmonic motion of the form $\mathbf{q}(t) = \mathbf{u}\, e^{i\omega t}$, the equation reduces to the classical eigenvalue problem:

$$(-\omega^2[M] + [K])\mathbf{u} = \mathbf{0} \tag{6}$$

This can be rearranged into the standard generalized eigenvalue form:

$$[K]\mathbf{u} = \lambda[M]\mathbf{u} \tag{7}$$

where $\lambda = \omega^2$ is the eigenvalue corresponding to the squared natural frequency, and $\mathbf{u}$ is the associated mode shape.

For an undamaged structure, we denote the eigenvalue problem as:

$$[K_0]\{\mathbf{u}_i^0\} = \lambda_i^0[M_0]\{\mathbf{u}_i^0\} \tag{8}$$

Here, $[K_0]$ and $[M_0]$ are the global stiffness and mass matrices of the intact structure, λ_i^0 is the i-th eigenvalue, and $\{\mathbf{u}_i^0\}$ is the corresponding eigenvector (mode shape).

When scour-induced local stiffness degradation occurs, the perturbed eigenvalue problem becomes:

$$[K_d] = [K_0] + \Delta K, \quad [M_d] \approx [M_0] \tag{9}$$

Then the perturbed eigenvalue problem becomes:

$$[K_d]\{\mathbf{u}_i^d\} = \lambda_i^d[M_d]\{\mathbf{u}_i^d\} \tag{10}$$

Assuming small perturbation, the first-order approximation for the perturbed eigenvalue is [182]:

$$\lambda_i^d \approx \lambda_i^0 + \{\mathbf{u}_i^0\}^{\mathrm{T}}\Delta K\{\mathbf{u}_i^0\} \tag{11}$$

And the first-order correction to the mode shape is [182]:

$$\{\mathbf{u}_i^1\} = \sum_{\substack{s=1 \\ s\neq i}}^{n} \frac{\{\mathbf{u}_s^0\}^{\mathrm{T}}\Delta K\{\mathbf{u}_i^0\}}{\lambda_i^0 - \lambda_s^0}\{\mathbf{u}_s^0\} \tag{12}$$

Therefore, the updated mode shape is:

$$\{\mathbf{u}_i^d\} \approx \{\mathbf{u}_i^0\} + \{\mathbf{u}_i^1\} \tag{13}$$

When two eigenvalues λ_i^0 and λ_j^0 are initially close, their perturbed values may cross over:

$$\lambda_i^d > \lambda_j^d \quad \text{implies modal transition} \quad i \leftrightarrow j \tag{14}$$

This eigenvalue reordering leads to a switch in modal identity and is a key indicator of mode transition under evolving structural damage.

C.2. Higher order of natural frequency in the case study

Figure 1 illustrates the evolution of the natural frequencies of the first ten modes as scour depth increases. In the early stages of scour (from 0 to 1.0 m), the frequency curves exhibit relatively gradual reductions, indicating a uniform stiffness loss throughout the substructure. However, beyond a critical depth of approximately 1.5 m, several higher-order modes (notably Modes 5 through 7) experience abrupt frequency drops or curve intersections. These phenomena are characteristic of *modal localization*, where vibrational energy becomes concentrated near the locally weakened region, and *modal transition*, as evidenced by the reordering of modal frequencies. Meanwhile, some lower-order modes (e.g., Mode 1 and Mode 2) remain relatively stable, underscoring their dominance by global structural stiffness and reduced sensitivity to localized damage. Overall, this pattern confirms that higher-order modal parameters are more responsive indicators for detecting scour-induced damage in masonry bridge piers.

Modal localization is induced by local damage, such as changes in boundary conditions or stiffness degradation, and it is more likely to occur in higher-order modes. However, this does not imply that all higher-order modes are sensitive to such local damage. As shown in Figure 1, the 9th and 10th modes do not show significant abrupt changes in frequency.

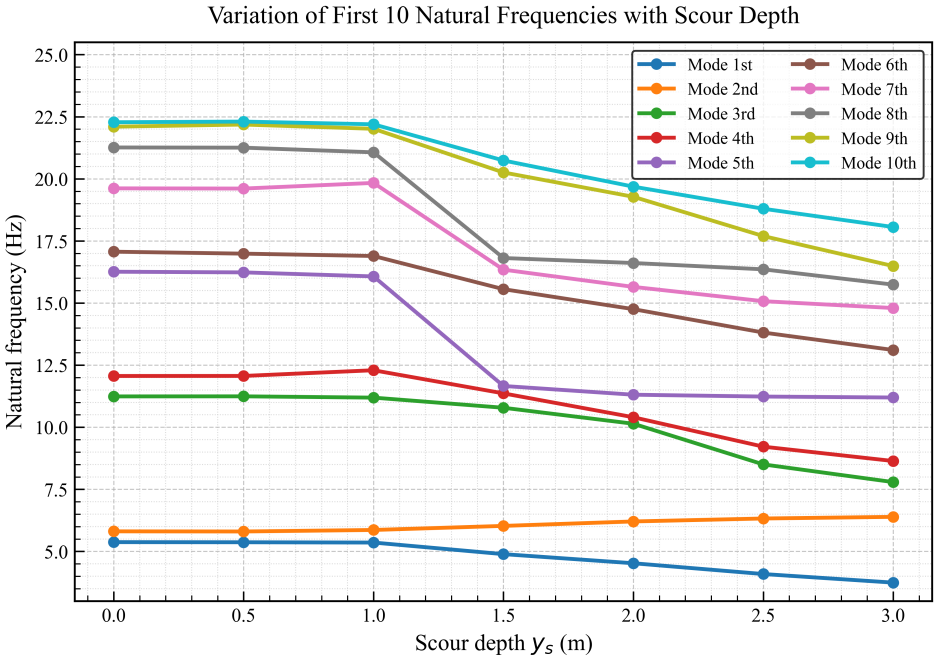

Figure 1: Natural frequency of the 10 modes during scouring

Appendix D. Summary of sensitivity analysis

Summary of the sensitivity analysis of material parameters on the first to sixth natural frequencies are shown in Figure 2, 3 and 4:

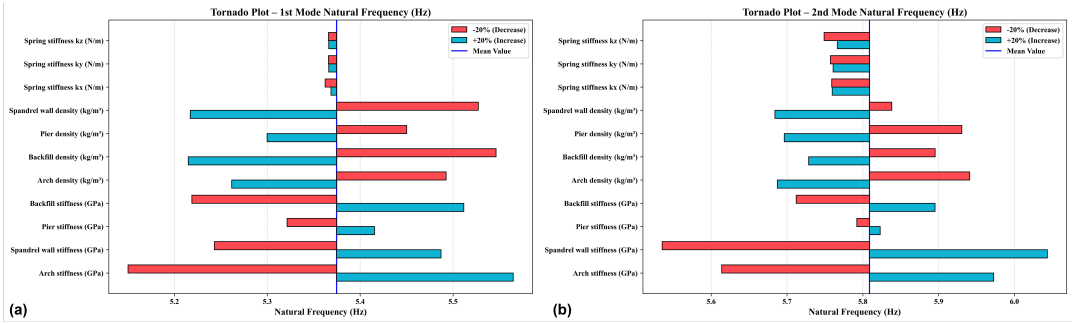

Figure 2: Sensitivity analysis: (a) to the first natural frequency and (b) to the second natural frequency

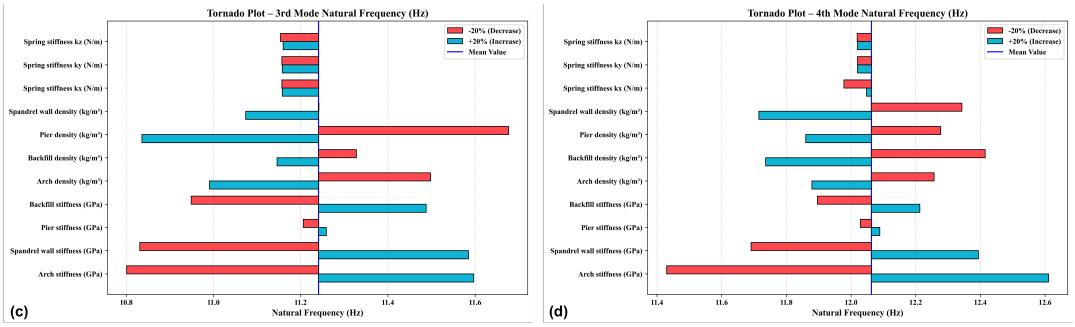

Figure 3: Sensitivity analysis: (c) to the third natural frequency and (d) to the fourth natural frequency

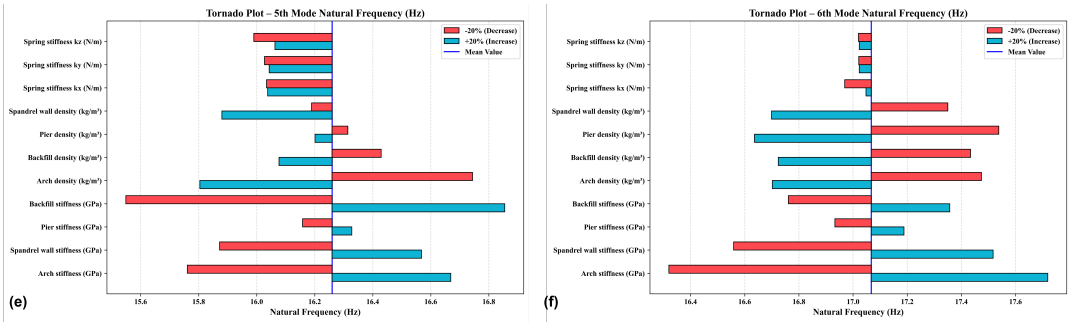

Figure 4: Sensitivity analysis: (e) to the fifth natural frequency and (f) to the sixth natural frequency